HEXACOORDINATE SILICON COMPLEXES FOR ELECTRONIC DEVICES

by

Margaret Kocherga

A dissertation submitted to the faculty of
The University of North Carolina at Charlotte
in partial fulfillment of the requirements
for the degree of Doctor of Philosophy in
Nanoscale Science

Charlotte

2020

Approved by:

_____
Dr. Thomas A. Schmedake

_____
Dr. Michael G. Walter

_____
Dr. Yong Zhang

_____
Dr. Daniel S. Jones

_____
Dr. Susan R. Trammell

ABSTRACT

MARGARET KOCHERGA. Hexacoordinate Silicon Complexes for Electronic Devices (Under the direction of DR. THOMAS A. SCHMEDAKE)

Organic electronics such as organic light emitting diodes, organic photovoltaics, organic field effect transistors begin to replace classically used technology. This is due to their tailorability, possibility of smaller and flexible devices, and new functionalities. These devices are light weight and consume less power. Although, these qualities are beneficial, there are major drawbacks to this technology. Commercially available devices exceed the cost of conventional due to instability and short lifetimes of organic materials, which results in costly manufacturing and assembling. Also, many devices employ heavy metals and rare-earth metals, which impose environmental challenges.

Hexacoordinate silicon based complexes with conjugated pincer ligands will have improved electronic, optical, and chemical properties for wide-scale application in organic electronic devices. The hexacoordinate silicon center enforces planarity of the pincer ligand, leading to extended, conjugation and improved optical properties compared to the free ligand alone. Also, the tridentate nature of the pincer ligand would lead to a more stable product less stable to hydrolysis than existing state-of-the-art materials such as Alq_3. In this work a new generation of electron and hole transport, and electroluminescent materials were synthesized, characterized and tested in prototype devices.

In this work, complexes with hexacoordinate silicon complexes with dianionic pincer ligands, $Si(pincer)_2$, motif were tested. All of the synthetic analogs were found to be air/moisture stable and fluorescent in solution and solid state. Thin films of the

complexes can be grown using vacuum deposition with high uniformity. The charge carrier mobilities of Si(pincer)$_2$ complexes have been measured and demonstrated that Si(pincer)$_2$ complexes are efficient electron and hole transport layers with electron mobilities comparable to commercially available alternatives. Si(pincer)$_2$ complexes have been successfully embedded into prototype OLEDs and OPVs, which confirms that hexacoordinate silicon complexes are attractive candidates for organic electronic applications.

ACKNOWLEDGEMENTS

I would like to thank for funding for this research provided by the NSF Division of Chemistry under award number CHE-1800331, support from the UNC Charlotte Targeted Research Internal Seed Program and a graduate student career preparedness supplement to the NSF-REU/DOD-ASSURE supported NanoSURE program (CHE-1460867).

This work would not be possible without support, encouragement, and contribution of many people. First, I would like to express my gratitude, and respect to my mentor and advisor Dr. Tom Schmedake for providing advice, guidance, assistance, and support. His ability to stay open minded, the will to explore, and attention to my growth and evolution brought to me the opportunities I would have never imagined. Also, huge thanks for his patience. I am very grateful for his ability to dive into all the experiences with me from measuring OLED emission in complete darkness, to going to middle school with me to provide hands on experience to children, to writing fellowship applications, to collaborating with different groups in different departments, to entrepreneurship. He is a great role model for me as a professional and as a human being. Dr. Schmedake had enormous impact on me to become the person I am today.

I am thankful that Dr. Michael Walter allowed me to be in his research lab as if I was a member of his lab, it provided amazing experience for me to learn, grow, and explore. I appreciate his will to always discuss any new ideas or try some new device designs. His positive outlook and the will to explore kept me motivated, when I had yet another device design not work. I am also very thankful to have been a part of other projects, which allowed me to learn new things, and share what I have learned. I would

like to say words of appreciation to Dr. Yong Zhang, for always willing to come up with a way to generate new ideas and experiments. I want to thank him for allowing me to not be afraid of quantum mechanics. For allowing to work with him and his group members on two projects, and for letting me mentor Lisa, she is a bright young woman, and I cannot wait to see where the future takes her.

Big thank you to the chair of the department Dr. Bernadette Donovan-Merkert, for support, for motivation, and for not letting me quit my first year. It was very important to have such support from you and be able to explore variety of non-traditional academic experiences. Words of appreciation to Dr. Dan Jones for allowing me to work with XRD, it was my dream since I was an undergraduate, and it was amazing opportunity to be able to perform experiments myself, and work on experiments for my projects, as well as other groups in the department and beyond. Big thank you to Dr. Jon Merkert for always being ready to address my complaints about cold labs, leaky roof, light bulb replacement in the fume hood, sink leaks, pump struggles, glovebox challenges and so many other things that I came to him with. Separate words of appreciation for his help with cyclic voltammetry and spending hours with me to capture OLED emission.

More words of gratitude for Dr. Tino Hoffman for the will to help a struggling graduate student to address a problem, which had turned into collaboration and resulted in publication. I appreciate our long discussions about material properties, and his enthusiasm and ability to be upfront about the topics in question. I would like to thank Dr. Christopher Bejger for letting me work with the samples from their group to learn more about XRD, and even though I would get frustrated at the twentieth attempt at a crystal from a batch, I knew how important it was and kept trying. Seeing the end result

that reveals a complex structure is truly amazing, and I appreciate that our collaboration resulted in publication. I would like to also thank Dr. Susan Trammell who was kind to become one of my committee members, she allowed me to believe that I can understand nuclear physics, even though I was “the chemist in the room”, she is absolutely amazing teacher.

Very thankful for the help that Jose Castaneda was providing with Raman measurements, performing variety of photoluminescence bleaching and thermal annealing experiments, as well as helping with AFM measurements. I am very thankful for contribution that Kevin Boyle was able to provide on the project. His patience, work ethic, and the will to learn have been amazing qualities, and I had a great pleasure mentoring him, and see him navigate through his career as a scientist. I am grateful for his help with assembling and testing of almost two thousand pixels of variety of devices. Thank you for being patient, always ready to listen and becoming a friend, and I am looking forward to seeing you grow. Another thank you for the help and contributions of Lynn Stevens, whom I had the pleasure of mentoring, and I am looking forward to seeing her dissertation defense. I would also like to thank Kate Norman, and Michael Lust for their commitment and help on verity of projects, and Adam Earnhardt for helping me hunt the data.

Next, I would like to thank those that help me find the strength and navigate how to continue in life through my father’s illness and after he passed away. I would like to thank UNCC’s department of chemistry, and how everyone came together to support me in many ways, it made a huge difference. Special thank you to Dr. Angelica Martin for taking the time and help me navigate through challenging situations, helping find

resources, or by simply being there for me to talk through everything. Monica Rabinovich has been a great teaching supervisor, she was always there to help in moment of struggle of how to handle teaching, as well as always provided me support, which is so important as an instructor. She had also shown great support for me during the toughest time in my life. I am also very grateful for the people that were in my cohort of nanoscale science students Maddy Greenier, Damian Beasock, Weina Ke, Amanda Reid, Abhispa Sahu, Nick Sayresmith, and Esha Thakur they have shown me you support in so many ways from personal, to helping with outreach, to collaborating on research projects.

I would like to say words of appreciation to those that helped me directly and indirectly to stay on track and stay sane. I would like to say big thank you to Marissa Styron, although she is no longer with us, she would have been very happy to see me do well in the program. Marissa had motivated and inspired me since the time I did undergraduate research under mentorship, and she had been supporting me ever since, she will remain in my memory and memory of many other students as a great mentor and person. Would like to express words of appreciation to Tyler Adams for uplifting the spirits in the lab when I was yelling at the glovebox, for helping with maintenance, and for all the support. Thanks to Jesse Ingham for maintaining twenty-five copies of my dissertation to make sure nothing gets lost.

Most importantly I would like to thank my parents Maryna and Gennadiy Kocherga for all the sacrifices, unconditional love and support. They have always supported my new beginnings, held me accountable, and did not let me give up. My father is no longer with us, but I will always appreciate his valuable life lessons.

TABLE OF CONTENTS

LIST OF TABLES

LIST OF FIGURES

CHAPTER 1: ORGANIC ELECTRONICS

1.1 Introduction

Organic electronic devices consist of active layers composed of organic molecules and/or polymers. Organic materials were first found to have acceptable electronic properties in 1950-1960s.[1] Electroluminescence in organic materials was observed shortly after.[2] Organic electronic devices have many unique advantages over conventional electronics. For example, they can be manufactured on flexible substrates, they have potential for printability, and they can be tuned allowing for a wide range of properties. These advantages allow for a variety of different applications such as organic light emitting diodes (OLEDs) in displays,[3] signage and lighting; organic photovoltaics (OPVs) for outdoor and indoor solar cells and photodetectors for biomedical application.[4] They also enable unique emerging applications such as organic field-effect transistors (OFETs) for pixel switches on electronic paper.[5]

Typically, semiconducting organic molecules contain conjugated substructure. Such structure results in an overlap of π-orbitals and allows for delocalization of the π-electrons facilitating the conduction. In OLED devices, charge carriers, electrons and holes, can be injected into the organic materials at the anode (holes) and cathode (electrons). The charge carriers travel through the organic material via a hopping mechanism from molecule to molecule.[6] Eventually the electron and hole can combine to form an electron-hole pair, which is called an exciton. The resulting exciton can be a singlet or triplet exciton depending on the spin pair orientation. In singlet excitons, spins align in opposite directions, and the exciton can relax radiatively, since radiative relaxation from the excited singlet state to the ground state (singlet) is spin-allowed.

Radiative recombination from the triplet exciton is spin-forbidden however, and typically non-emissive. Since the singlet exciton is singly degenerate while the triplet exciton is triply degenerate and typically lower energy, only 25% of excitons are emissive and 75% of the injected charge carriers are wasted. Several schemes have been developed to harvest the triplet excitons including: increasing the radiative recombination efficiency of the triplet exciton by addition of a heavy atom (PHOLEDs),[7] thermally activated delayed fluorescence (TADF),[8] and triplet fusion delayed fluorescence (TFDF).[9]

1.2 Organic electronic devices

1.2.1 Organic light emitting diodes

OLEDs are one of the greatest examples of commercially successful organic electronic devices and have been extensively studied in academia and industry for the last thirty years. OLED displays for example have significant advantages over the conventional liquid crystal display (LCD) technology.[10, 11] LCDs use a white-light source, polarizing filters, liquid crystals and color filters. OLEDs offer a significantly simpler design that is direct emission, which does not require color filters or light source. This fundamental difference in the engineering of the devices allows OLEDs to have lower power consumption, faster response time, better contrast, wider viewing angles, and new form factors. Even though this technology is commercially available, there are still many issues with OLEDs, such as poor lifetime, moisture sensitivity, burn-in issues, and high manufacturing cost.[12]

The existing challenges motivate the research community in both academia and industry to find new solutions. The first OLED was reported by Tang and VanSlyke in

1987 in its simplest design, where a single organic layer is sandwiched between anode and cathode as shown in **Figure 1.1**.[13] This was the first successful demonstration of the electrons and holes being transported through organic material under forward bias voltage resulting in light emission. The charges are injected into the organic material, travel towards the center of the device due to applied electric field, and recombine in the form of an electron-hole pair, exciton. The light is then emitted as these excitons decay and release their energy as a photon. This mechanism of OLED operations is shown in **Figure 1.2**.

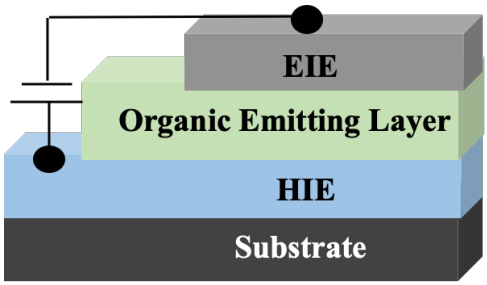

Figure 1.1. Schematic representation of the first OLED device. The organic light emitting layer is sandwiched between the electron injecting electrode (EIE) and hole injecting electrode (HIE).

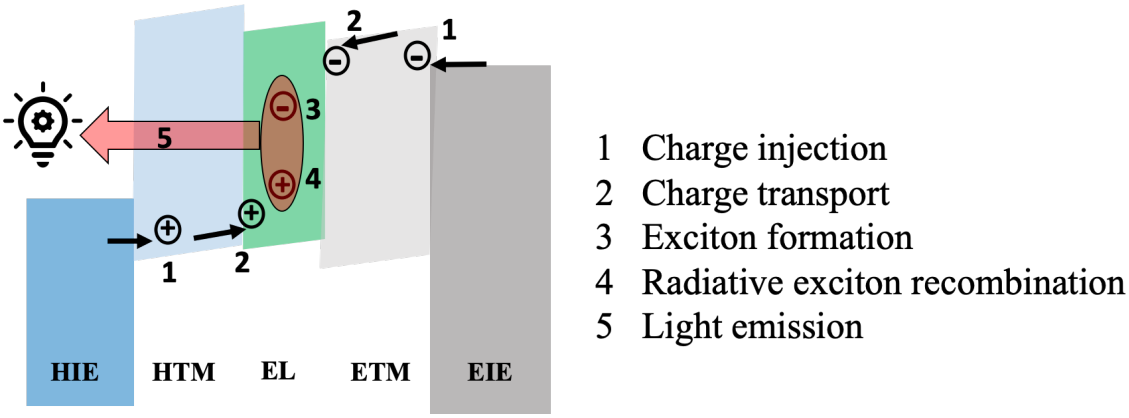

Figure1.2. Schematic representation of the photon generation in OLEDs: charge injection and transport through the HTM:ETM interface, exciton formation and radiative emission. HIE-hole injection electrode; HTM-hole transport material; EL-emissive layer; ETM-electron transport material; EIE- electron injection electrode.

There are five key step that are occurring in order for successful light emission to occur. The first step is injection of electrons and holes through electron injecting electrode (EIE) and hole injecting electrode (HIE), upon applied bias voltage.

The second step is charge transport. After the injection, the charges have to travel towards the center of device, organic emitting layer, and the charge transport efficiency depends on how ordered the materials are. Highly ordered materials have greater carrier mobilities, while materials with defects will have worse carrier mobilities and are prone to have traps sites for charges, causing loss of efficiency.

The third step is exciton formation. After traveling through the electron or hole transport materials (ETM and HTM), electrons and holes will combine to form singlet and triplet excitons in the emitting layer leading to the last two steps: radiative exciton recombination and light emission. Well-designed singlet exciton emitters can emit with a near unity quantum yield leading to an overall internal quantum efficiency approaching 25%. To exceed this limit a triplet harvesting scheme must be exploited.

1.2.1.1 State of the art

One of the ways of improving the device performance is by thermally activated delayed fluorescence (TADF). Unlike traditional singlet emitters, the triplet excitons that are usually non-emissive are converted into the singlet excitons via reverse intersystem crossing (RISC). This is possible when the singlet-triplet energy levels have a gap of less that 0.1 eV.[14] By converting the triplet excitons into singlet, it is possible to obtain 100% internal quantum efficiency (IQE), instead of 25% when using singlet emitters. This hypothetical 100% IQE is a result of the prompt and delayed fluorescence mechanisms.

The prompt fluorescence is $S_1 – S_0$ (first excited singlet state – ground state) decay and occurs on the nanosecond scale. Singlet excitons that are created via RISC result in delayed fluorescence, which happens on the order of 100 μs.[15] This time delay conveniently does not affect the spectral distribution, and both have the energy from the $S_1 – S_0$ decay. The key challenges are to design materials that not only have a small singlet-triplet gap, but also have a stable triplet state that would allow the excitons to efficiently undergo the RISC to singlet state. Current TADF emitters are either macromolecules, dendrimers, or polymers. Examples of such emitters from 2020 review of Jiang *et. al* are shown in **Figure 1.3.**[16]

There are still some challenges to this day to prepare TADF materials that would meet all the requirements. The first challenge is to achieve a small singlet-triplet gap and maintain high photoluminescence. Second, in the case of macromolecules and polymers, they suffer quenching of the excited states. Another challenge is ability to control the emission, addition of units that assist in control and prevention of quenching, often results in broadening of the light emission, or additional unwanted luminescence. All of these shortcomings inspire research for new materials to continue in academia and industry.[17]

Another approach to improving the OLED efficiency is to use phosphorescent emitters, which is somewhat reverse of TADF process. During phosphorescent emission the singlet excitons are converted to triplet through intersystem crossing (ISC).[18] ISC allows all of the singlet excitons to become triplet excitons, the heavy atom effect (spin-orbit coupling) enables the triplet excitons to radiatively emit and have 100% IQE. Such

OLEDs are called POLEDs, PhOLEDs or PHOLEDs. Although, phosphorescent emitters offer great performance improvement in comparison to the

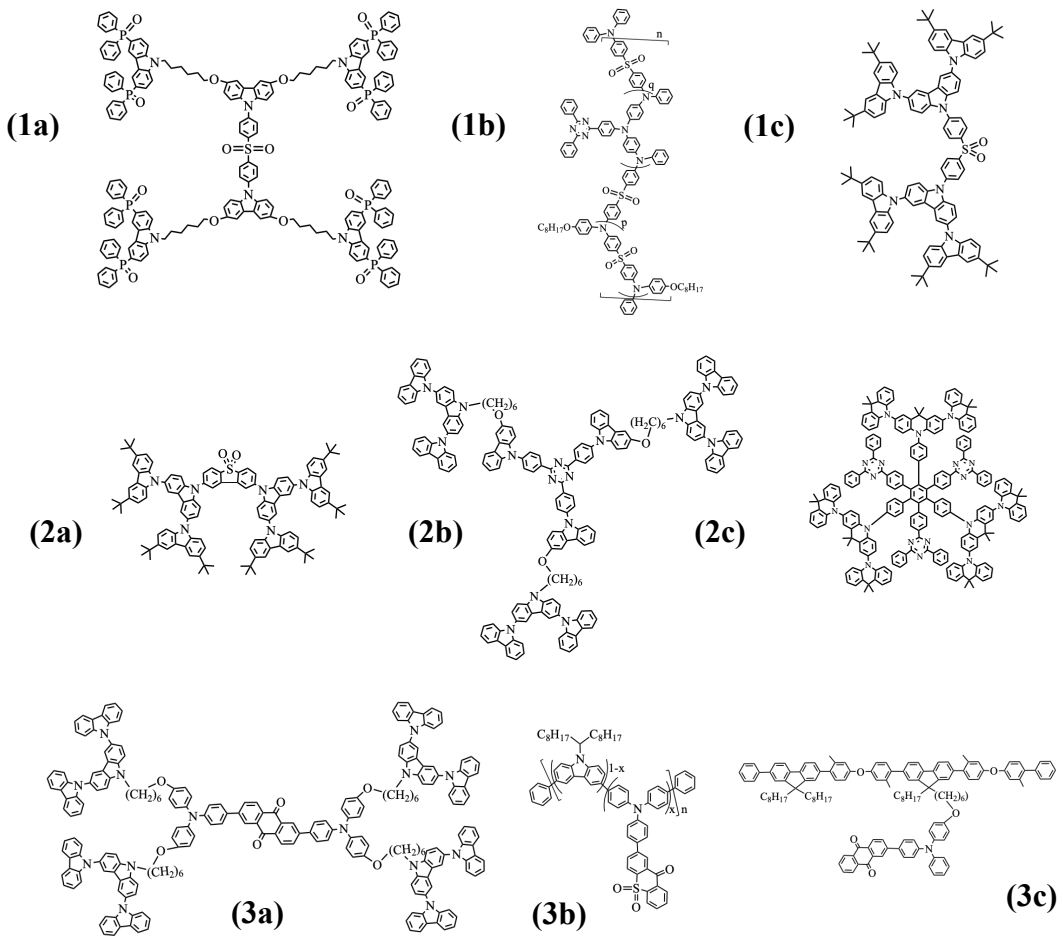

Figure 1.3. Examples of molecular structures of polymers and dendrimers for TADF emission. (**1a,b,c**) Blue TADF emitters. (**2a,b,c**) Green TADF emitters. (**3a,b,c**) Red TADF emitters.[16]

fluorescent emitters, there are limitations. At high bias voltages phosphorescent emitters suffer efficiency degradation called roll-off, they have very low lifetimes for blue emitters, and are usually made with scarce elements, which makes them expensive.[19] Some of the most commonly employed phosphorescent emitters are iridium based. In fact, most of the commercially available OLED displays employ iridium based green,

yellow, and red emitters produced by Universal Display Corporation. Few examples of recently reported by Mao *et. al* iridium emitters are shown in **Figure 1.4**.[20]

There is one more type of OLEDs that employs triplet states, and it is triplet fusion delayed fluorescence (TFDF) or triplet-triplet annihilation delayed fluorescence (TTADF).[21] This is a process in which two triplet states combine to produce either a triplet or singlet exciton that is higher in energy. When fluorescent emitters are used,

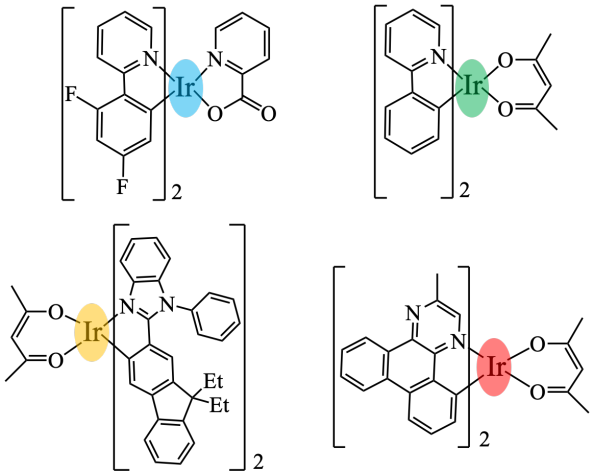

Figure 1.4. Examples of phosphorescent iridium complexes.[20]

TF results in formation of singlet excitons with much longer lifetimes, but leads to only 25% conversion efficiency due to spin statistics. In the systems where first excited singlet state energy level is at least twice larger than the first triplet state. TF can be executed under requirement that first triplet state must be at least two times smaller in energy than the higher-order triplet states to prevent production of non-radiative excitons. This approach allows to achieve 50% IQE. The first material to meet these criteria was rubrene with tetracene based molecule. Since then material variety has increased, but motif remained similar. Some of the TFDF-OLED materials are shown in **Figure 1.5**. Although this approach is very promising, there are great challenges in to maximizing the

contribution of TTS process due to lack of understanding of the mechanism. Similarly to POLEDs, these materials suffer roll-off issues, along with poor efficiency of the deep-blue.

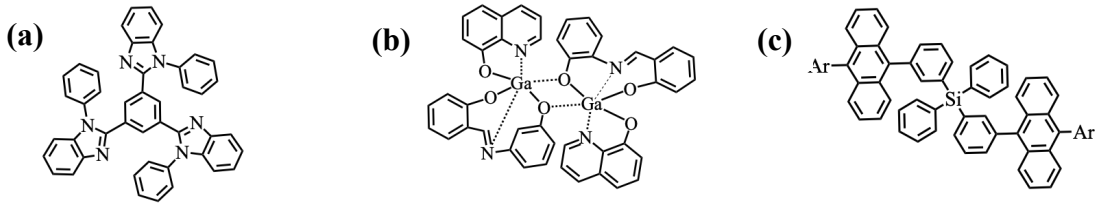

Figure 1.5. Examples of TFDF materials. (a) charge transfer featured (b) and (c) local excited featured.[9]

The key shortcomings in OLEDs are the low efficiency and poor lifetime. To improve the performance more complex device designs are used in the current market. In **Figure 1.6 a** the most essential layers for current device are listed, most commercial OLEDs would have multiple materials in the stack for each of the essential layers. To further improve the external quantum efficiency (EQE), tandem devices are often used, shown in **Figure 1.6 b**. Tandem OLEDs allow for over 100% IQE due to presence of multiple emissive layers, which results in multi-photon emission, with over 100% quantum efficiency and improvement in EQE. Tandem white OLED device design is shown in **Figure 1.7**, where can be seen that it was assembled with over 20 layers.[22]

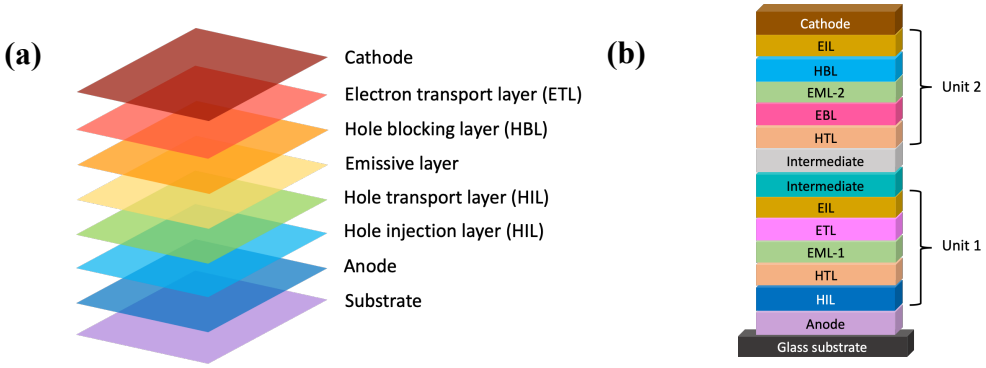

Figure 1.6. Modern OLED structures. (a) Single emitter OLED.[23] (b) Tandem OLED.[24]

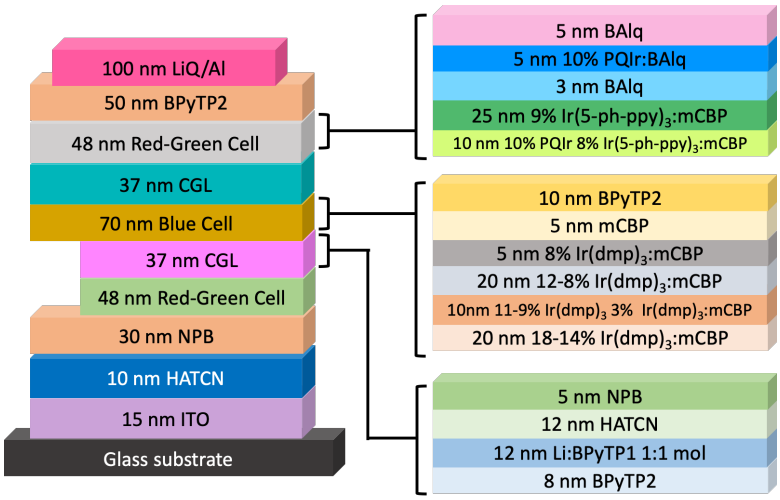

Figure 1.7. White emitting tandem OLED structure.[22]

1.2.2 Organic photovoltaics

Organic photovoltaic devices have distinct differences to inorganic OPVs, and even though they not as efficient, there have been significant improvements in the efficiency and lifetime in recent years.[25, 26] Inorganic semiconductors have electrons delocalized over a sigma bonded three-dimensional lattice, while organic semiconductors have electrons delocalized over the conjugation within the molecule and are held together by π- π stacking of the molecules, van der Waals, and dipole-dipole based intermolecular interactions. The key difference between the inorganic and organic photovoltaic devices is how excitons are generated upon illumination. Upon absorption of photons by the inorganic solar cells, the free electrons and holes are generated, while in the organic solar cells, both electrons and holes are still bound via Coulombic forces. This results in the need for different device architectures in order to successfully separate the electron and hole pairs.[27, 28] Although, architectural engineering can assist to resolve some issues in charge separation and extraction, the inorganic solar cells are still far superior to the

organic counterparts, as can be seen in **Figure 1.8**. This motivates the area of organic semiconductors to continue growing.

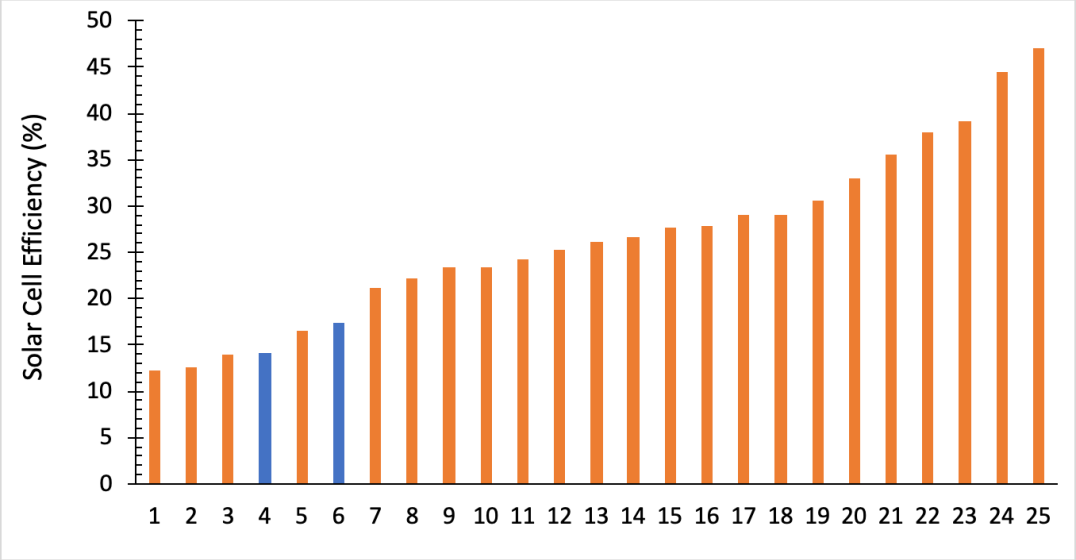

	Type of solar cell		Type of solar cell
1	Dye-sensitized	14	Silicon heterostructures
2	CZTSSe	15	Single-crystal (concentrate)
3	Amorphous Si:H (stabilized)	16	Single crystal Single-junction GaAs
4	Organic tandem	17	Thin-film crystal GaAs
5	Quantum dot	18	Perovskite/Si tandem
6	Organic	19	Single-junction GaAs concentrator
7	Thin-film crystal Si	20	Two-junction (non-concentrator)
8	CdTe	21	Two-junction (concentrator)
9	Multicrystaline	22	Three-junction (non-concentrator)
10	CIGS (concentrator)	23	Four-junction (non-concentrator)
11	Perovskite/CIGS tandem	24	Three-junction (concentrator)
12	Perovskite	25	Four-junction (concentrator)
13	Single-crystal (non-concentrate)		

Figure 1.8. Best research solar cell efficiencies from National Renewable Energy Laboratory July 2020 report.[29]

Currently, OPVs underperform inorganic based devices, but there are many benefits that can be achieved using OPV technology such as flexible, bendable, lighter, safer, and lower cost solar cells. Two of most common architectural designs of OPVs are shown in **Figure 1.9**, which generally have sandwich like structure, where organic layers

are inserted between cathode and anode. In order to separate the Coulombically-bound electron-hole pairs, the photoactive layer includes electron transport material (ETM) with a high electron affinity and hole transport material with a small ionization potential (HTM). The HTM and ETM can be assembled in either bilayer fashion as shown in **Figure 1.9 b** or in bulk-heterojunction (BHJ) configuration shown in **Figure 1.9 c**. Indium tin oxide (ITO) is commonly used as hole collecting electrode (HCE), and aluminum is chosen as electron collecting electrode (ECE). It is also common to include poly(3,4-ethylenedioxythiophene):poly(styrenesulfonate) (PEDOT:PSS) as a hole transport layer.

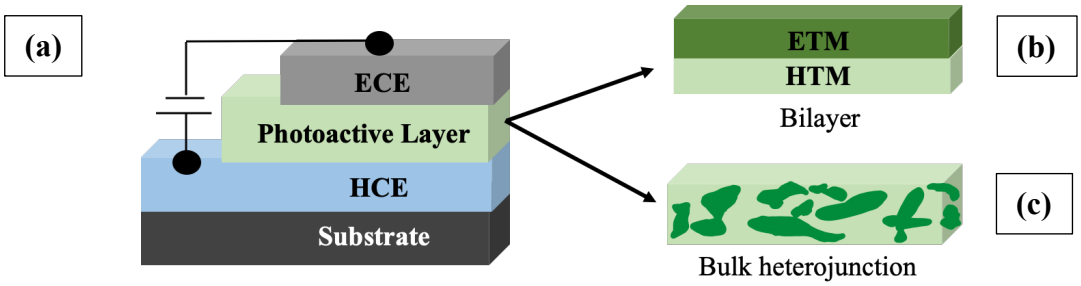

Figure 1.9. Simplified schematic representation of OPV device. The photoactive layer is sandwiched between the electron collecting electrode (ECE) and hole collecting electrode (HCE).

There are five key step that are occurring in order for successful conversion of light to occur as shown in **Figure 1.10**. The first step for operation of OPV is absorption of photons by the photoactive layer, which causes formation of Coulombically bound electron-hole pairs called excitons. The formed excited state is a theoretical limit for the maximum voltage that can be achieved from the device. The exciton binding energy in organic semiconductor is typically in the range of a few hundreds of meV, and on the order of a few meV for inorganic semiconductors.

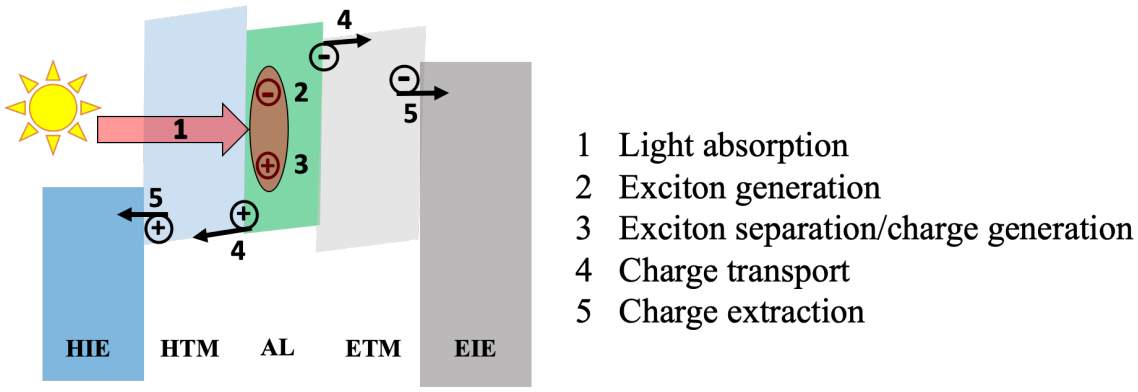

Figure 1.10. Schematic representation of the photo-induced charge-carrier formation in OPVs: exciton formation and dissociation at the HTM:ETM interface through charge separation and charge-transfer. HIE-hole injection electrode; HTM-hole transport material; AL-active layer; ETM-electron transport material; EIE- electron injection electrode.

The second step is exciton migration. After the exciton is formed, it then needs to reach the HTM:ETM interface for the charge transfer to occur. To reach the interface, the exciton will have to diffuse through the material and migrate towards the interface. Exciton diffusion is competing with exciton decay or charge recombination, which results in an exciton diffusion length typically around 5-20 nm for organic semiconductors [30, 31] High performance in OPVs can be achieved via minimization or radiative and non-radiative decay pathways that contribute to loss of excitonic states. Thus, the device needs to be engineered in a way that would maximize the number of excitons that reach the interface

The third step is exciton separation. In order to produce photocurrent, the exciton must dissociate into free charges, which in OPV needs an energetic driving force for charge separation to occur. Charge-transfer process through HTM and ETM serves as the driving force, where electrons and holes are transferred as intermediate step towards exciton separation.

The fourth step is charge transport. After the separation, the charges must travel towards the corresponding charge collecting electrodes, and the efficiency of the charge transport depends on how well-ordered the materials are. The more ordered the material the greater the carrier mobilities, while disordered materials will have worse carrier mobilities and are prone to have charge traps. The device efficiency is greatly impacted by the charge transport loses, which depends on parameters such as molecular packing, morphology and defects. All of these parameters are heavily investigated within the literature, to understand their impact. [32-34]

The fifth step is charge collection, which is the final step that requires charges to be collected at the appropriate charge collecting electrode. The success of charges being collected depends on metal-organic layer interface and electrode work functions that must be appropriately matched.

1.2.3 Device characterization

Photovoltaic device performance is judged based on the current-voltage response of the device in the dark and under illumination. The current density under illumination at zero applied voltage is the short-circuit current density Jsc. The voltage under illumination where current density is zero is the open-circuit voltage Voc. The points Vmax and Jmax can be identified as the values that give the maximum power output, Pmax, for the device. The fill factor FF of the device can be calculated as shown in Equation 1.1 and is demonstrated graphically in a sample plot shown in **Figure 1.11**. Another important parameter in device characterization is power conversion efficiency, $\boldsymbol{\eta}$, and can be calculated as shown in **Equation 1.2**.

$$FF = \frac{Jmax \cdot Vmax}{Voc \cdot Jsc} \qquad \text{Equation 1.1}$$

$$\eta = \frac{Voc \cdot Jsc \cdot FF}{Pin} \qquad \text{Equation 1.2}$$

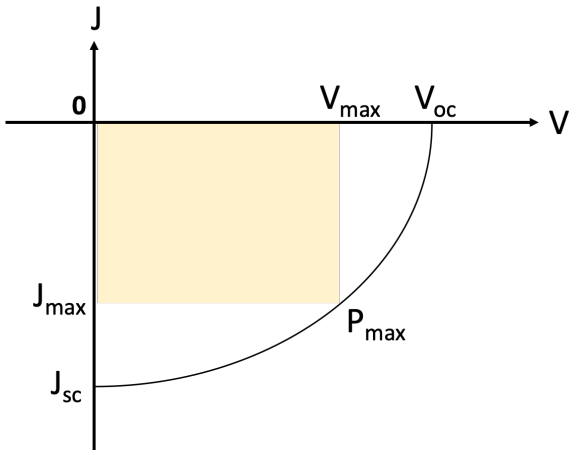

Figure 1.11. Current-voltage mock curve of a typical OPV device.

1.2.4 State of the art

Some of the current approaches to assembling OPVs are through bilayer or bulk heterojunction with small molecules, polymers or combinations of the two. These devices can have one or two active layers, modern devices would always have two active layers. There is a large variety of molecular donor and acceptor molecules that can be employed in OPVs. Some examples of the donor molecules are shown in **Figure 1.12** from review by Lin *et. al*.[35] There are many more molecules reported in the review, but examples of each family of molecules are shown here, such as dye-based (**Figure 1.12 a, b**), oligothiophene-based (**Figure 1.12 c**), acene-based (**Figure 1.12 f**), triphenylamine-based (**Figure 1.12 d, e**), and commonly used polymer based acceptor P3HT (**Figure 1.12 g**).[35] There is also a variety of acceptor molecules that can be used as an active layer component in OPVs. Some of the representative molecules are shown in **Figure 1.13.**

Fullerene-based acceptors, such as very commonly used $PC_{70}BM$ is shown in **Figure 1.13 a**, rylene diimide-based (**Figure 1.13 b**), and other nonfullerene-based acceptors (**Figure 1.13 c, d, e, f**).[35]

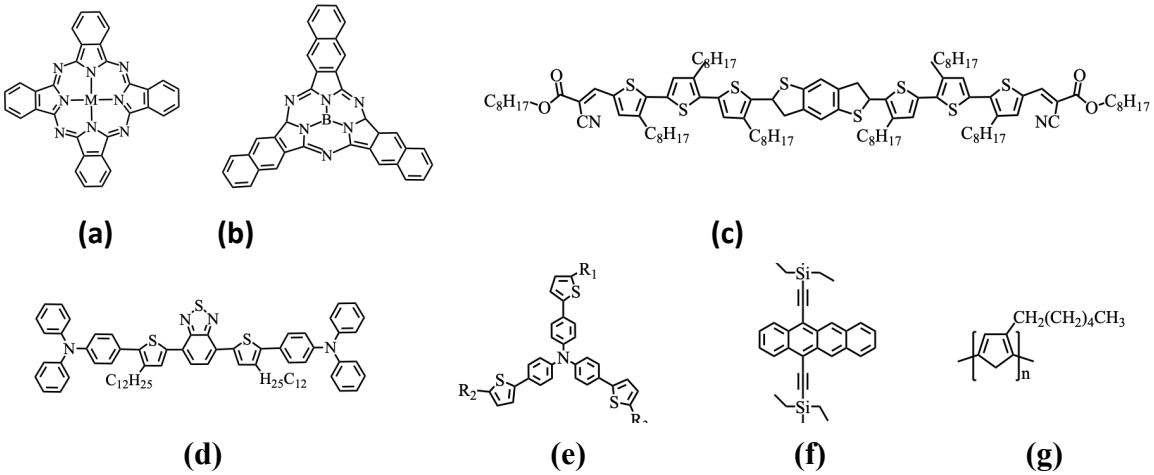

Figure 1.12. Chemical structures of donor molecules for OPVs.[35]

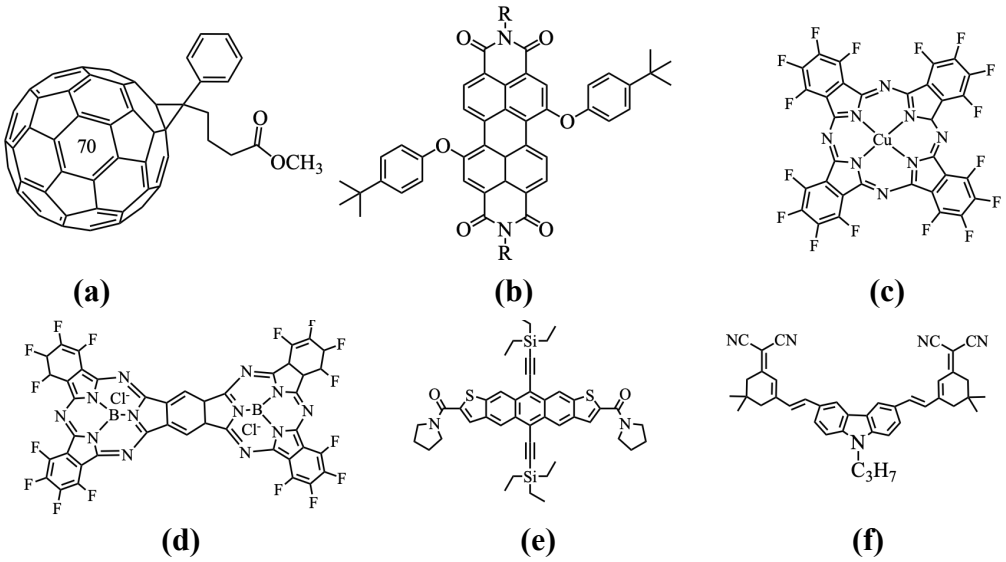

Figure 1.13. Chemical structures of acceptor molecules for OPVs.[35]

1.3. Charge transport in organic electronics

Charge transport materials are a very important part of electronic devices. It is crucial for optimal device performance to select appropriate charge transport materials

that have optimal transport rates, packing, and appropriate energy levels. ETM and HTM have to be not only good materials, but their rate of recombination, space-charge distribution, electron and hole injection must match each other.

The key requirements for electron transport materials are: a) high electron mobility, b) good electron-injection, and c) good hole-blocking.[36] The current range of electron transport rates is between 10^{-3} – 10^{-8} cm^2/Vs. Examples of currently used electron transport molecules are shown in **Figure 1.14**.[37] The key challenges are ability to maintain high electron mobility, high triplet energy, and the anility be deposited into smooth thin films.

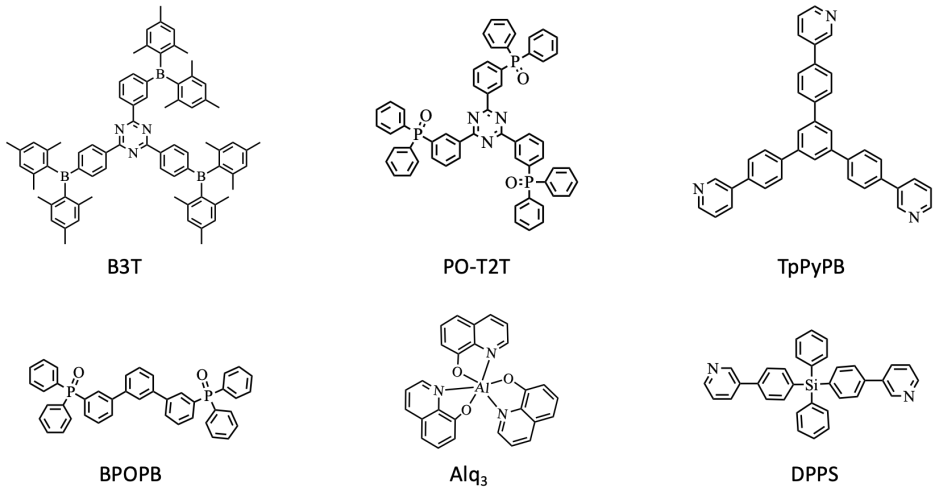

Figure 1.14. Examples of electron transport materials.[37]

Good hole transport materials should have: a) high hole mobility, b) good hole-injection, and c) good electron-blocking. The current range of hole transport rates is between 10^{-3} – 10^{-9} cm^2/Vs. The key shortcomings in the current materials is ability to obtain high carrier mobility, and thermal stability. Also, the synthesis is often very

complex, resulting in high cost of these materials. Examples of currently used molecular hole transport materials are shown in **Figure 1.15**.[38]

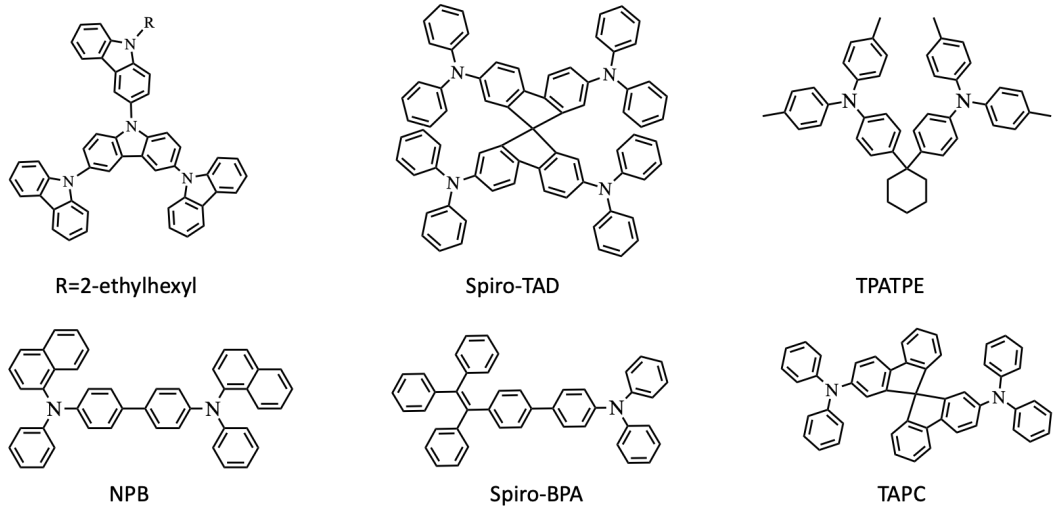

Figure 1.15. Examples of hole transport materials.[38]

When an interface is formed between a metal and an intrinsic semiconductor, given that the value of the work function of the metal, or the metal Fermi energy, E_F^{metal} , is approximately equal to either the energy of conduction or valence band, either electrons or holes are injected into the semiconductor from the metal forming either a negative or positive space-charge layer at the interface. At high voltages, the charge density becomes spatially constant, and the current shows Ohmic behavior and depends on this spatially constant charge-carrier density, given essentially by the density of states and the injection barrier heights.

When relatively low voltage is applied across the device, the current across the device will mainly be governed by drift. The current in this case is usually described by the Mott–Gurney law. In this regime the relationship is no longer $J \propto V$, but rather $J \propto V^2$. The Mott-Gurney equation is shown in Equation 1.3, where μ is the charge carrier

mobility ($m^2\ V^{-1}\ s^{-1}$), J is the current density ($A\ m^{-2}$), L is the thickness of the film (m), V_a is the applied voltage (V), $\varepsilon_0 = 8.85 \times 10^{-12}$ A s V^{-1} m^{-1} is the permittivity of free space, $\varepsilon = 3$ is the relative dielectric constant.[39]

$$J = \frac{9}{8}\,\varepsilon\varepsilon_o\mu\frac{V_a^2}{L^3} \qquad \text{Equation 1.3}$$

When all of these conditions are met, then Mott–Gurney equation can be used to compute the charge carrier mobility. Mott–Gurney law is a good model for interpreting Space-Charge-Limited Current of devices that satisfy the following conditions:[40]

(i) the semiconductor layer is a thin film

(ii) the semiconductor layer being probed is undoped and trap free

(iii) the semiconductor layer is sandwiched between two Ohmic contacts

(iv) diffusion contributions to the current must be negligible, which may be the case only for certain voltage ranges.

CHAPTER 2: HEXACOORDINATE SILICON COMPLEXES FOR APPLICATION IN ORGANIC ELECTRONICS

2.1. Introduction

Metal chelates have been frequently used in organic electronics since the beginning of the field. They are used as electroluminescent layers (ELs), electron transport layers (ETLs), hole transport layers (HTL), emissive layers (EM) and others. The very first reported organic light emitting diode device that was reported by Tang and VanSlyke employed tris(8-hydroxyquinolinato)aluminium, Alq_3.[41] The complex Alq_3 and its derivatives are routinely used in OLEDs, OPVs,[3] perovskite solar cells,[4] memory and spintronic devices[5]. There is a continuous development of new materials for organic electronic devices that are chemically and electrochemically robust, and efficient. Challenging multi-step syntheses raise the cost of these materials, and organic electronic materials often employ scarce elements as described in Chapter 1. There are also challenges in manufacturing using these materials due to their poor chemical stability. All of these factors lead to exploring new types of molecular materials for organic electronics.

Chelating ligands have been widely employed in d-block coordination chemistry, but they are not commonly used with main block elements. There has been a rapid increase in the synthesis and utilization of stable hexacoordinate silicon complexes in recent years. The first examples of hexacoordinate complexes were those that employed pyridine ligands in 1963.[42] The most notable is tremendous success of hexacoordinate silicon phthalocyanine complexes such as Pc4 shown in **Figure 2.1** as photodynamic therapy agents for cancer treatment.[43] Silicon phthalocyanines have also been utilized as

near-IR sensitizers in dye-sensitized solar cells.[44] The air/moisture stability and photo-stability

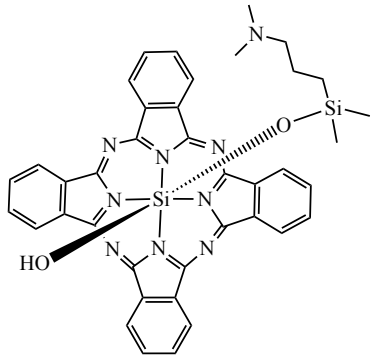

Figure 2.1. Structure of Pc4.

of these complexes results in part from the rigid tetradentate N_4-ligand that favors octahedral geometry at the silicon center.

Likewise, bidentate and tridentate ligands containing pyridine moieties have proven to be excellent stabilizing ligands for hexacoordinate silicon centers.[45] A wide variety of air/moisture stable bipyridine and phenanthroline complexes have been synthesized, and applications with these compounds are emerging. Fluorescent dyes (**Figure 2.2 a**) ,[46] DNA intercalators (**Figure 2.2 b**),[47-49] high-energy materials (**Figure 2.2 c**),[50] and electrochromic materials (**Figure 2.2 d**)[51] have been developed based on the rigid octahedral-like geometry imposed by the polydentate, pyridine-containing ligands.[45]

Hexacoordinate silicon complexes have been largely neglected as promising structural templates for electronic applications. Very little has been reported about the luminescent properties of hexacoordinate silicon complexes. Schmedake has reported the photoluminescence of charged hexacoordinate silicon complexes, $[Si(bpy)_3](PF_6)_4$ (**Figure 2.2 d**),[52] $[Si(terpy)_2](PF_6)_4$, and $[Si(bpy)_2(O,O\text{-dipyridocatecholate})](PF_6)_2$.[53] A

recent study by Shibahara *et. al*,[46] demonstrated that compound **Figure 2.2 a**, possesses a high fluorescence quantum yield (λ_{em} = 499 nm and quantum yield, Φ_F = 0.98), and fluorescent applications of hexacoordinate trifluorides analogous to **Figure 2.2 a** have been patented. The limited reports in the literature so far, indicate polydentate pyridine-containing ligands are a promising ligand motif to target for further synthetic development of hexacoordinate silicon complexes for applications in electronics.

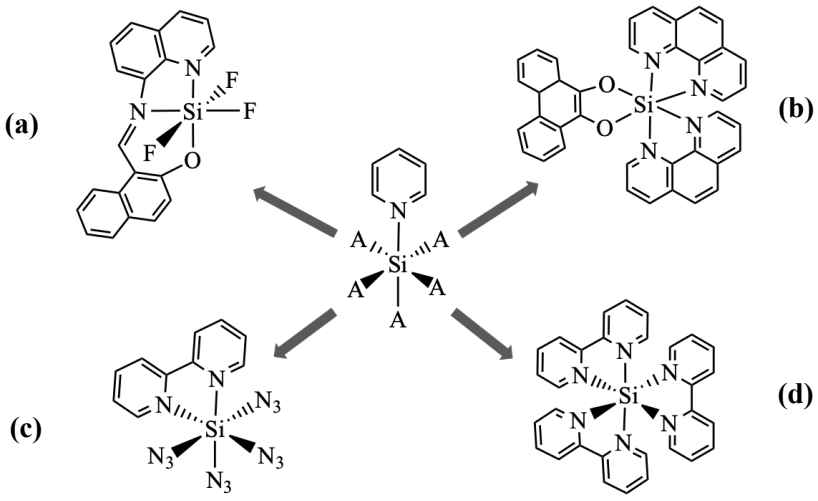

Figure 2.2. Hexacoordinate silicon with pyridine-containing ligands.[45]

Silicon is the smallest tetravalent atom capable of forming stable hexacoordinate complexes. Tetravalency is advantageous because it allows for two symmetric dianionic pincer ligands to coordinate to the center atom, leading to low dipole moments and lack of stereoisomers. The small size of silicon is advantageous because it minimizes spin-orbit coupling effects, thereby providing longer triplet state lifetimes. Also, the tetravalent silicon center is fairly redox innocent with reductions being primarily ligand localized in hexacoordinate Si(IV) complexes;[54] this should lead to greater intermolecular

electronic coupling with low reorganization energies and therefore fast electron transfer rates and high electron mobility.

These benefits of employing hexacoordinate silicon-based complexes lead to hypothesis that they will have ideal electronic, optical, and chemical properties for wide-scale application in organic electronics. The hexacoordinate center will enforce planarity of the pincer ligands, resulting in extended conjugation, which would lead to better charge transport. The tridentate nature of selected pincer ligands will lead to a more stable product, addressing the hydrolysis issues in current materials. Upon successful synthesis of Si(pincer)$_2$ complexes, a new generation of hexacoordinate silicon complexes that can be used as materials for organic electronic devices can be obtained.

2.2. Synthesis of hexacoordinate complexes

Several Si(bzimpy)$_2$ derivatives were synthesized using modified 2,6-bis(benzamidazol-2'-yl)pyridine, bzimpy, ligand. To obtain Si(bzimpyOMe)$_2$ complex 2,2'-[4-(methoxy)-2,6-pyridinediyl]bis[1*H*-benzimidazole], bzimpyOMe, ligand was used. To obtain Si(bzimpyMe)$_2$ complex 2,2'-(2,6-Pyridinediyl)bis[5,6-dimethyl-1*H*-benzimidazole], bzimpyMe, ligand was used. To obtain Si(bzimpyMeOMe)$_2$ complex 2,2'-[4-(methoxy)-2,6-pyridinediyl]bis[5,6-dimethyl-1H-benzimidazole], bzimpyMeOMe, ligand was used. For Si(IPI)$_2$ complex ligand 2,6-bis(imidazol-2'-yl)pyridine, IPI, was used. The described ligands were used as shown in **Schemes 2.1 and 2.2** to yield the hexacoordinate silicon complexes. The appropriate ligand was dried under vacuum then reacted with silicon tetrachloride and triethylamine in chloroform under continuous nitrogen flow. This reaction did not work with the 2,6-bis(indol-2'-

yl)pyridine, BIP, ligand, presumably due to the lower acidity of the BIP ligand. Instead, $Si(BIP)_2$ was synthesized by first lithiating the BIP ligand in THF, followed by reaction with $SiCl_4$ (Scheme 2.3). The reactions were left to proceed overnight at room temperature. The crude reaction mixtures were collected using liquid-liquid extraction in solutions of dichloromethane followed by evaporation to provide the crude product, which was subsequently purified by chromatography and recrystallization as needed. The pure complexes were then characterized using a variety of solution- and solid-state characterization techniques described in this work.

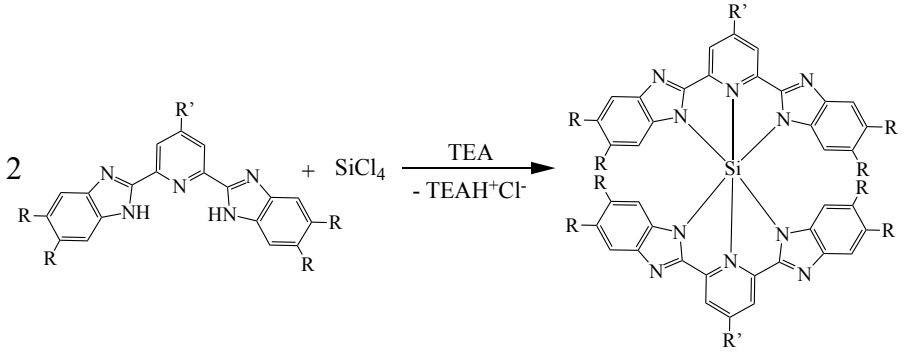

Scheme 2.1. Reaction synthesis scheme of $Si(bzimpy)_2$ derivatives.

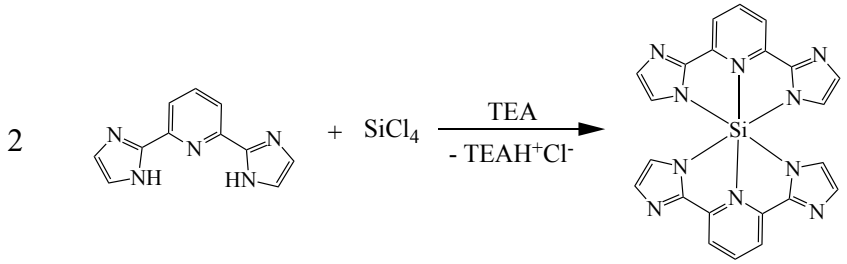

Scheme 2.2. Reaction synthesis scheme of $Si(IPI)_2$.

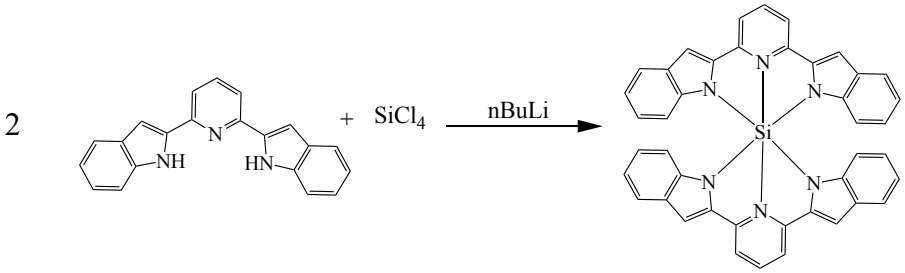

Scheme 2.3. Reaction synthesis scheme of $Si(BIP)_2$.

For all of the complexes, a characteristic upfield shift is observed in the ^{1}H NMR as a result of the aromatic ring current of the perpendicular ligand. The upfield shifted hydrogen position for each complex is indicated by the red circle in **Figure 2.3**. The hydrogen signal shifts from 7.8-7.0 ppm to 6.0-5.4 ppm region, and in the case of Si(bzipmy)$_2$ 5.9 ppm. ^{1}H NMR (**Figure 2.4**) also shows evidence for the 2:1 hexacoordinate complex in solution and the symmetry due to two ligands perpendicularly attached to the silicon center. The representative NMRs of each complex are shown in the **Appendix G-K**. ^{13}C NMR spectra can be seen in **Appendix L-P**, which confirm the presence of hexacoordinate silicon complexes. ^{13}C NMR spectrum of Si(bzipmy)$_2$ is shown in **Figure 2.5**.

The ^{29}Si NMR peaks appear in the region that is expected for hexacoordinate silicon complexes containing pyridine ligands, that has been reported to be between -140 ppm and -190 ppm for all of the complexes.[45] For the complexes observed in this work the ^{29}Si NMR peaks have been observed between -179 ppm and -189 ppm, and spectra can be seen in the **Appendix Q-U**, which confirms the presence of hexacoordinate silicon complex in solution. ^{29}Si NMR spectrum of Si(bzipmy)$_2$ is shown in **Figure 2.6**.

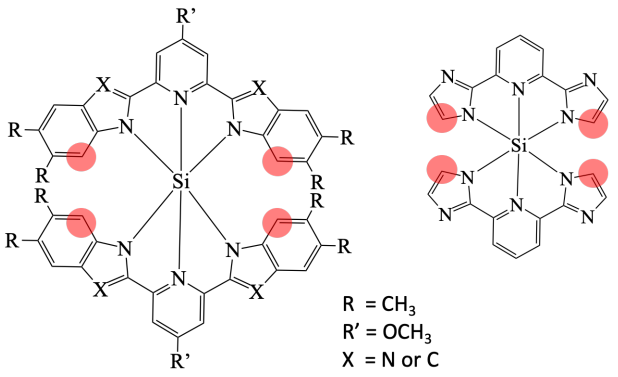

Figure 2.3. Location of hydrogen that is most shielded due to aromatic ring-current. On the left is the scheme of Si(bzimpy)$_2$ and Si(BIP)$_2$ motif complexes, and on the right is the scheme of Si(IPI)$_2$

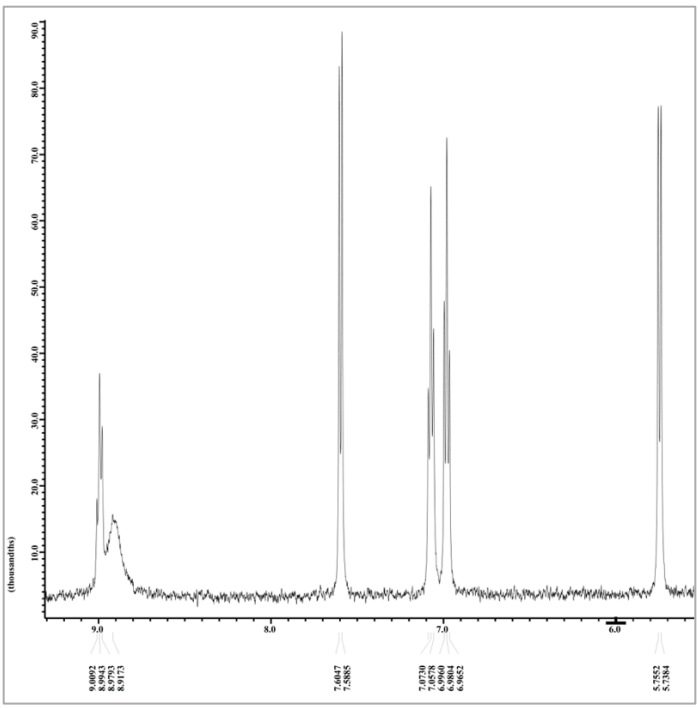

Figure 2.4. ^{1}H NMR spectrum of **Si(bzimpy)$_2$**. (500 Mhz, CD_2Cl_2)

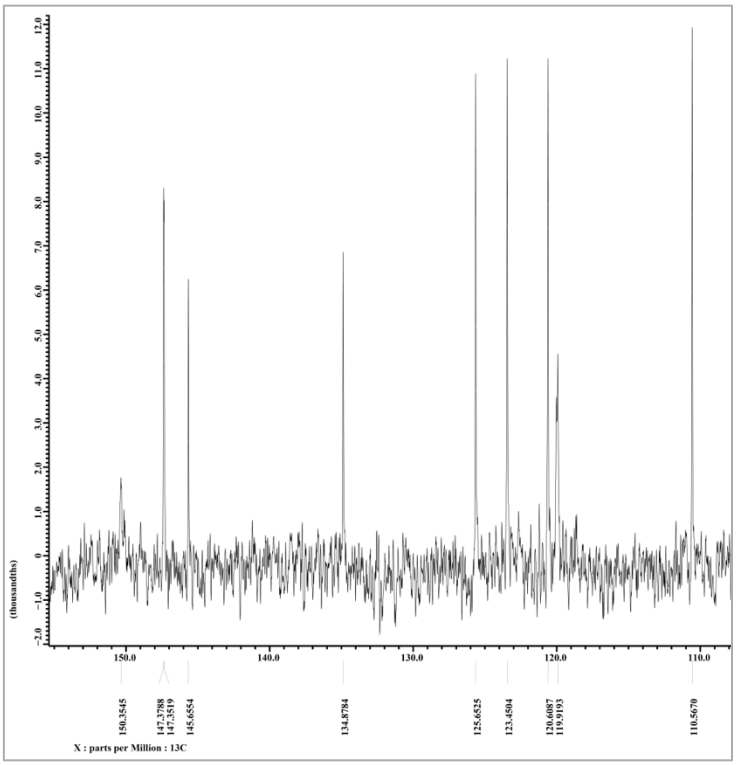

Figure 2.5. ^{13}C NMR spectrum of **Si(bzimpy)$_2$**. (125 Mhz, $CDCl_3/CD_3OD$)

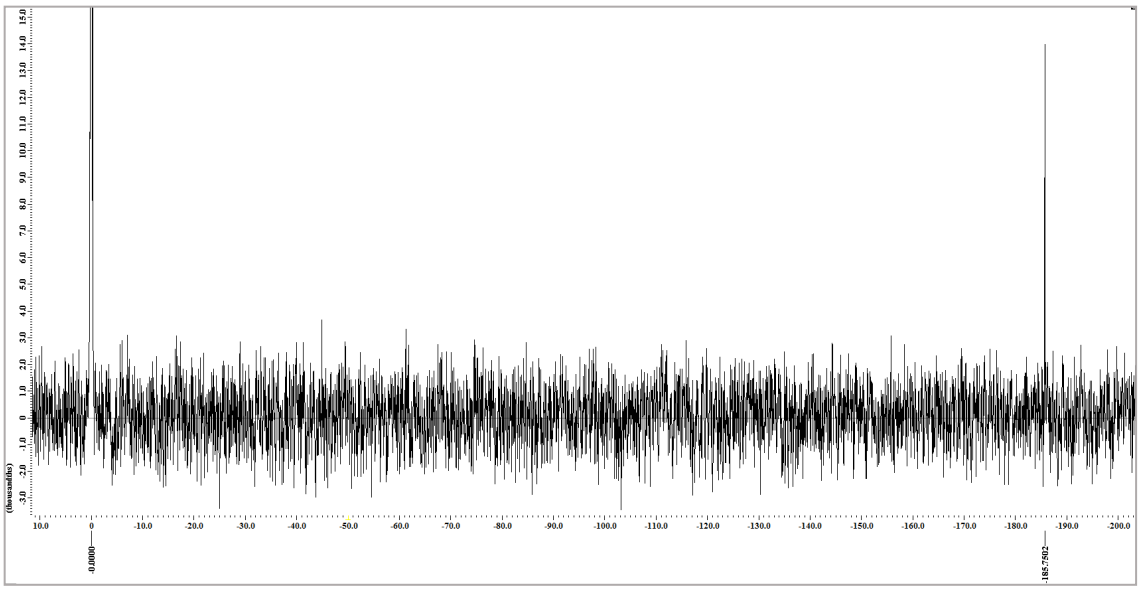

Figure 2.6. ^{29}Si NMR spectrum of **Si(bzimpy)$_2$**. (99 Mhz, $CDCl_3/CD_3OD$)

The crystal structures were also obtained for complexes Si(bzimpy)$_2$, Si(bzimpyMe)$_2$, Si(bzimpyOMe)$_2$, Si(bzimpyMeOMe)$_2$, and Si(IPI)$_2$, which are shown in **Figure 2.7**. All of the complexes were formed with two ligands perpendicular to each other, which confirms the results obtained via NMR and the peaks that were observed. For Si(bzimpy)$_2$ derivatives that have substituents, significant distortion from planarity is observed, especially in the case of Si(bzimpyMeOMe)$_2$. This distortion is not observed via NMR possibly due to free movement in solution, and an average of the signals of different movements is captured.

To further confirm the presence of hexacoordinate species in the solid state, MALDI-TOF (mass assisted laser desorption ionization – time of flight) mass spectrometry was used to see if corresponding m/z (mass to charge ratio) to hexacoordinate silicon complex species will be present. As a result of these experiments, it was observed that each of the synthesized complexes is indeed present as a

hexacoordinate species in the solid state. Spectrum of $Si(bzimpy)_2$ is shown in **Figure 8**, and others can be found in **Appendix V-Y**.

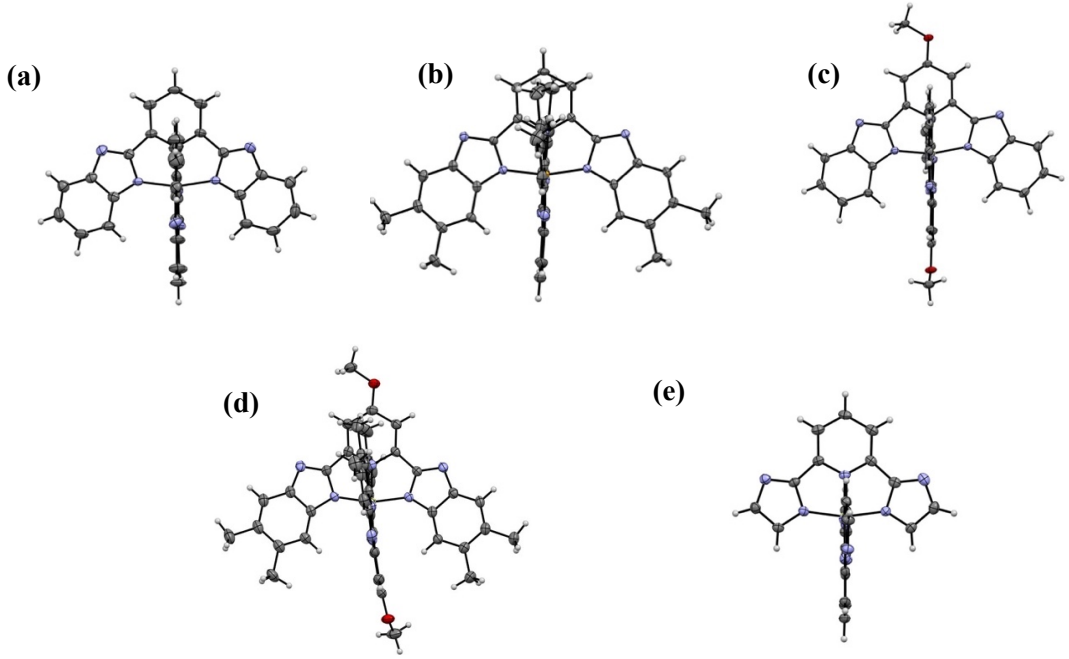

Figure 2.7. Crystal structures of: (a) $Si(bzimpy)_2$, (b) $Si(bzimpyMe)_2$, (c) $Si(bzimpyOMe)_2$, (d) $Si(bzimpyMeOMe)_2$, and (e) $Si(IPI)_2$.

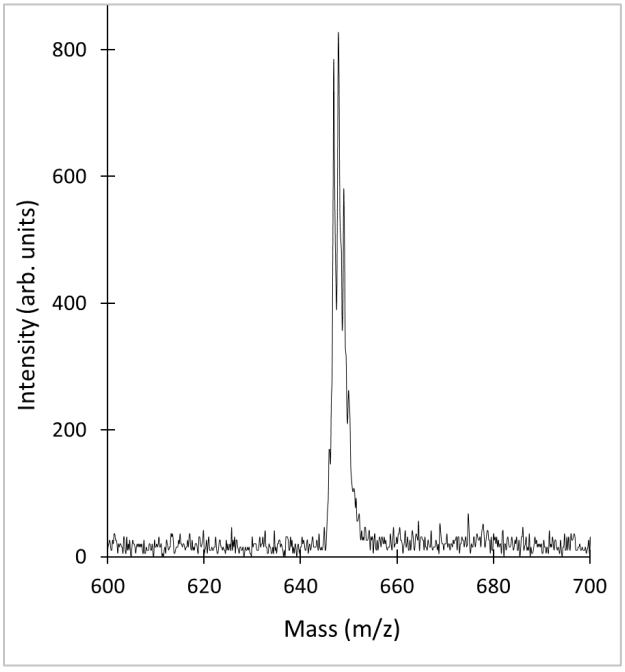

Figure 2.28. MALDI-TOF-MS spectrum of **$Si(bzimpy)_2$** (Matrix = 1,8,9-trihydroxyanthracene)

2.3. Characterization of complexes in solution

Optical properties of molecules are a significant part of characterization of molecules and understanding their potential for organic electronics applications. A simulated UV-Vis spectra for all six of the obtained complexes can be seen in **Figure 2.9**. It is important to note two distinct and broad peaks for all of the complexes, a stronger high energy peak and a weaker low energy peak that varies considerably with the composition of the ligand. Simulated spectra shown in **Figure 2.9** were calculated for complexes in gas phase using DFT with the B3LYP functional and the 6-31G* basis set.

Experimentally obtained UV-Vis data have been obtained in solution of dichloromethane or dimethylformamid (DMF), by making saturated solution then filtering using 45 μm PTFE microfilter, then diluted to have absorption bellow 1.0. The normalized absorbance spectra of complexes are shown in **Figure 2.10**. For clarity all spectra were normalized to have similar intensity of the highest energy peak. Comparison of the simulated and experimental UV-Vis spectra indicates validity of the selected calculation approach. The relative peak intensities, as well as approximate peak location

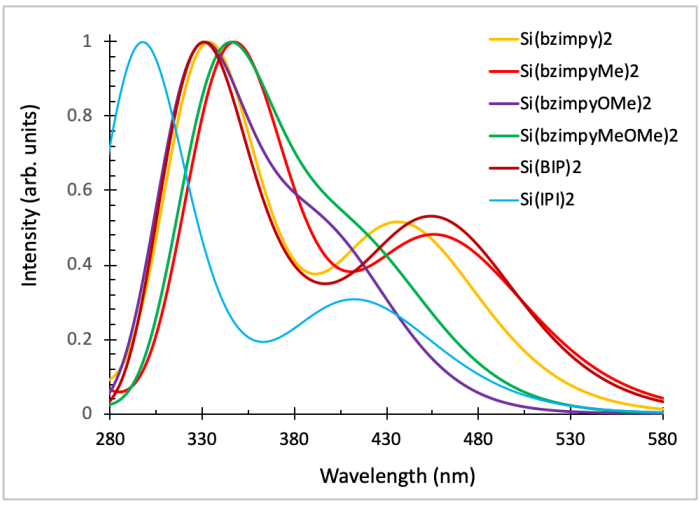

Figure 2.9. Simulated UV-Vis spectra of all complexes in gas phase (Calculations performed using Spartan'16).

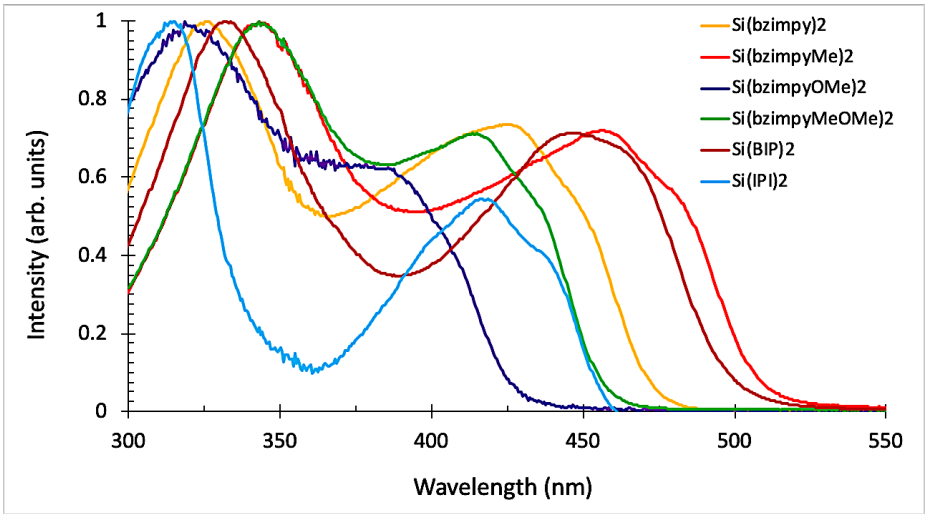

Figure 2.10. UV-Vis spectra of all complexes in solution (Intensity is normalized. Complexes Si(bzimpy)$_2$, Si(bzipmyMe)$_2$, Si(bzimpyOMe)$_2$, Si(bzimpyMeOMe)$_2$, and Si(IPI)$_2$ were dissolved in DCM, and Si(BIP)$_2$ in DMF)

have been correctly assigned in the simulated approach. In **Table 2.1** the two most intense peaks are reported for simulated and experimentally obtained spectra, indicating strong correlation. This provides confidence that molecular modeling using DFT (B3LYP/6-31G*) can help design and identify target molecules with desired properties, which is a powerful tool in the quickly evolving environment of the organic electronics industry.

Table 2.1. Values of intensity for the two greatest intensity peaks from simulated and experimentally obtained UV-Vis spectra of all complexes.

Complex	Simulated (nm)	Experimental (nm)		Simulated (nm)	Experimental (nm)
Si(bzimpyOMe)$_2$	400	390		332	322
Si(IPI)$_2$	415	418		301	310
Si(bzimpyMeOMe)$_2$	422	415		348	343
Si(bzimpy)$_2$	440	428		335	325
Si(BIP)$_2$	455	458		332	333
Si(bzimpyMe)$_2$	460	454		350	343

The molar absorptivity corrected UV-Vis spectra for the four $Si(bzimpy)_2$ derivatives are shown in **Figure 2.12**. The UV-Vis experiment is a good visual demonstration of the ability to tailor the HOMO and LUMO of the molecules through synthetic modification, specifically in this case via the addition of electron donating substituents. The addition of electron donating groups onto the LUMO/HOMO portion of the molecule results in destabilization or raising of the LUMO/HOMO respectively. The LUMO of the parent complex $Si(bzimpy)_2$ is delocalized predominantly over the pyridine ring as shown in **Figure 2.11**, while the HOMO of the molecule is predominantly delocalized on the benzimidazole portion of the ligand. Addition of methyl groups to the benzamidazolyl group in $Si(bzimpyMe)_2$, primarily raises the HOMO resulting in a lowering of the HOMO/LUMO gap and accounts for the red-shift seen in the UV-vis spectrum (**Figure 2.12**). Likewise, addition of an electron donating methoxy group to the pyridine leads to a raising of the LUMO and accounts for the blue shift seen for $Si(bzimpyOMe)_2$ realative to $Si(bzimpy)_2$. In the case of addition of electron donating groups to both the pyridine and benzamidazolyl portions of the ligand, as in the case of

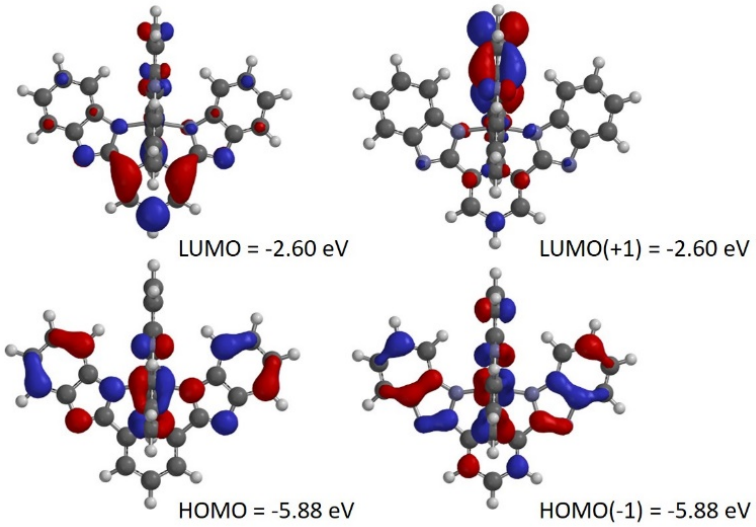

Figure 2.11. Calculated HOMO and HOMO-1 (left) and LUMO and LUMO+1 (right) of $Si(bzimpy)_2$ calculated in the gas phase, using B3LYP/6-31G* (Spartan 2016).

$Si(bzimpyMeOMe)_2$, both the LUMO and HOMO of the molecule are destabilized and the energy is both the LUMO and the HOMO are increased. The net effect is little change on the HOMO/LUMO gap and an overall absorption wavelength range very similar to the parent molecule, $Si(bzimpy)_2$, although the molar absorptivity is greater, as shown in **Figure 2.12**.

From the spectra demonstrated in **Figure 2.12** can be observed that the methylated derivatives overall have greater absorption of the incoming light. The complexes without methoxy groups on the pyridine, absorb broader than those with the methoxy groups. The fluorescence emission spectra of all six complexes in solution are shown in **Figure 2.13**. All complexes were dissolved in dichloromethane with the exception of $Si(BIP)_2$, which was dissolved in DMF due to solubility challenges. The excitation wavelength of 365 nm was used to excite all samples except $Si(BIP)_2$,which was excited with 450 nm wavelength due to differences in the excitation wavelengths for these complexes demonstrated in **Figure 2.11**. The highest energy fluorescence emission is observed for $Si(IPI)_2$, and the lowest for $Si(BIP)_2$. For $Si(bzimpy)_2$ derivatives, a

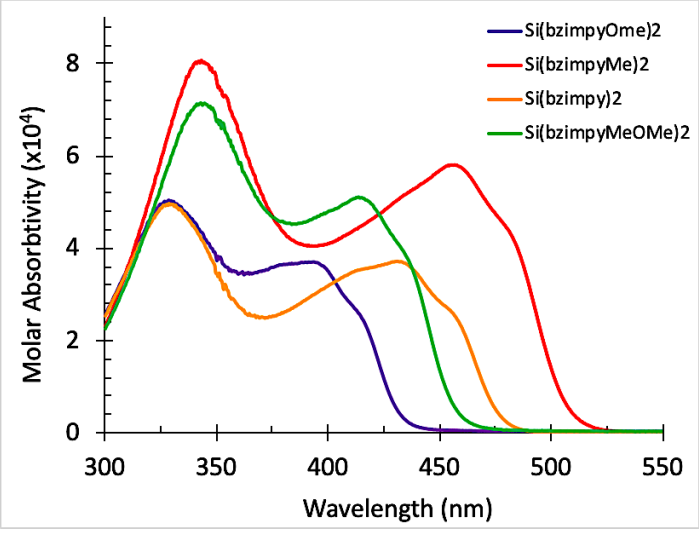

Figure 2.12. Molar absorptivity corrected UV-Vis spectra of complexes in solution of dichloromethane.

similar trend is observed as for UV-Vis. Raising of the HOMO due to added electron donating groups resulted in the shift of emission into the lower energy wavelengths for $Si(bzimpyMe)_2$, in comparison to the parent complex $Si(bzimpy)_2$. Raising of the LUMO due to added electron donating groups resulted in the shift of emission into the higher energy wavelengths for $Si(bzimpyOMe)_2$, in comparison to the parent complex $Si(bzimpy)_2$. Fluorescence emission peak of $Si(bzimpyMeOMe)_2$ is observed between $Si(bzimpyOMe)_2$ and $Si(bzimpy)_2$. **Figure 2.15** includes photos of fluorescence emission of all complexes in solution and solid state for better visual correlation.

The quantum efficiency (Φ) and lifetimes (τ, measured using time-correlated single photon counting) of all complexes in solution are listed in **Table 2.2**. The highest quantum efficiency was observed for $Si(bzimpyMe)_2$ (67%), and the lowest quantum efficiency was observed for $Si(BIP)_2$ (10%). The lifetimes range between 1-6 ns, which is typical for fluorescent emitters.One of the most common issues in the organic electronics world is presence of moisture, which results in material degradation and device failure. To see the effect of water on the hydrolysis and optical

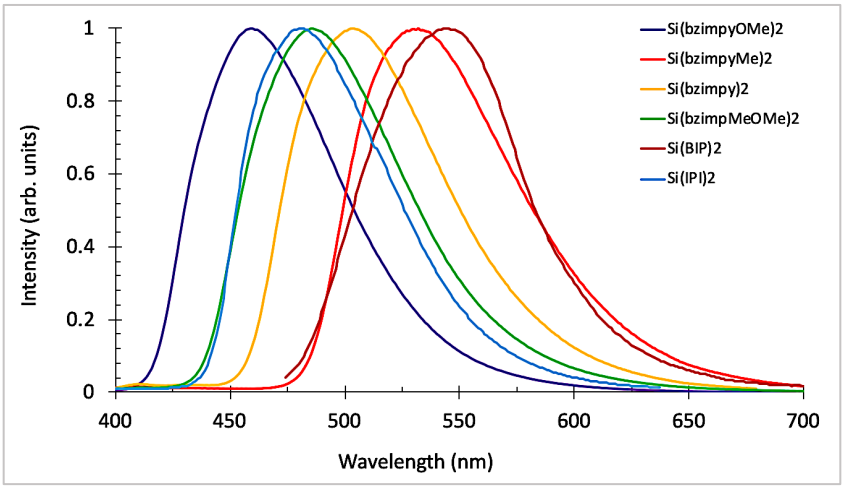

Figure 2.13. Fluorescence emission spectra of all complexes in solution (Intensity is normalized. Complexes $Si(bzimpy)_2$, $Si(bzipmyMe)_2$, $Si(bzimpyOMe)_2$, $Si(bzimpyMeOMe)_2$, and $Si(IPI)_2$ were dissolved in DCM, and $Si(BIP)_2$ in DMF)

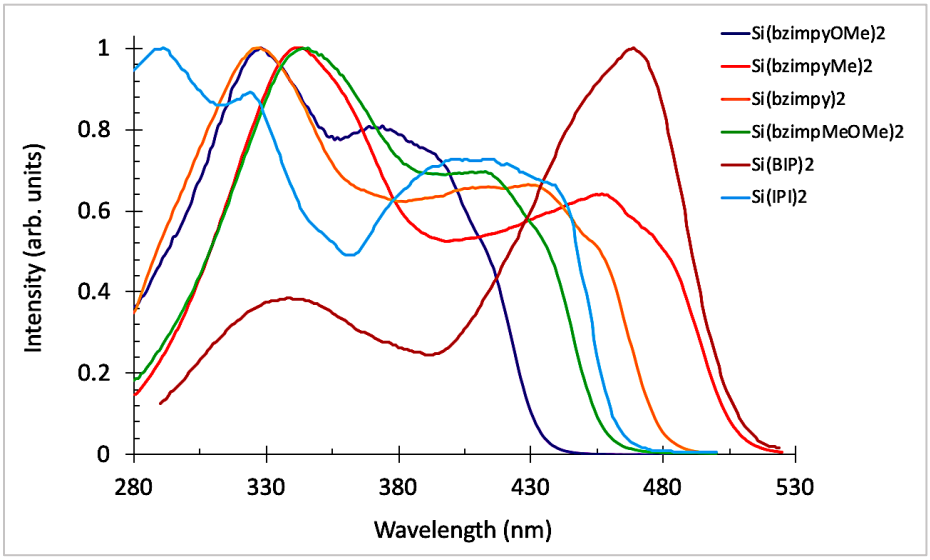

Figure 2.14. Excitation spectra of all complexes in solution (Intensity is normalized. Complexes Si(bzimpy)$_2$, Si(bzipmyMe)$_2$, Si(bzimpyOMe)$_2$, Si(bzimpyMeOMe)$_2$, and Si(IPI)$_2$ were dissolved in DCM, and Si(BIP)$_2$ in DMF)

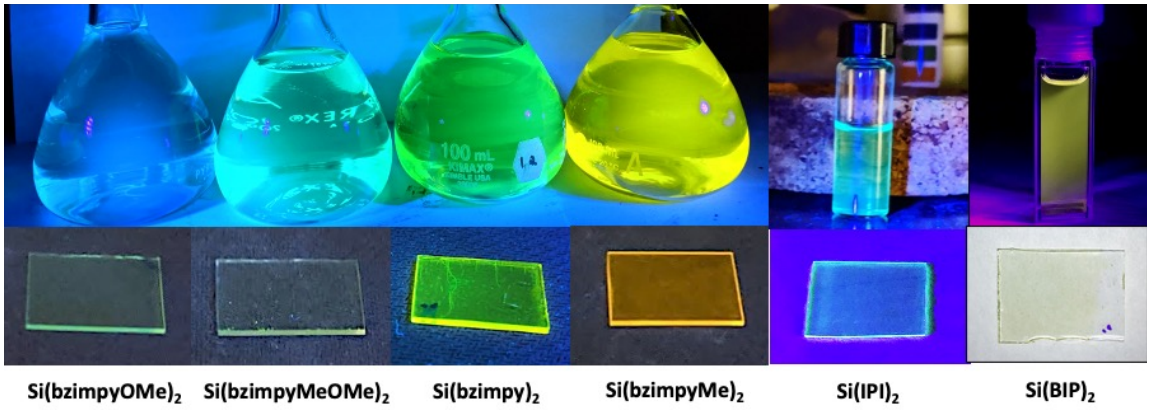

Figure 2.15. Fluorescence emission in solution and solid state. (Solid state emission of Si(BIP)$_2$ was not captured via camera due to low intensity)

Table 2.2. Solution phase quantum yields and lifetimes. Dichloromethane was used as a solvent except for BIP, which was dissolved in dimethylformamid.

Complex	Φ	τ(ns)
Si(bzimpyMe)$_2$	0.67	3.8
Si(bzimpyMeOMe)$_2$	0.66	4.1
Si(bzimpyOMe)$_2$	0.63	3.3
Si(bzimpy)$_2$	0.50	4.2
Si(IPI)$_2$	0.45	6.1
Si(BIP)$_2$	0.10	1.0

properties, $Si(bzimpy)_2$ was used to study the effects of moisture on this family of complexes via UV-Vis, fluorescence emission, and NMR. The experimental monitoring of $Si(bzimpy)_2$ dissolved in THF via UV-Vis is shown in **Figure 2.16**, and via fluorescence emission in **Figure 2.17**. The radiative and non-radiative rates, quantum yield, and lifetime are shown in **Table 2.3.** The radiative and non-radiative rates were calculated using the relationship shown in **Equation 2.1**, where Φ = quantum yield, τ = lifetime, k_{rad} = radiative rate, and k_{nr} = non-radiative rate. In **Figure 2.17** the black curve represents 100% THF:0% H_2O, and serves as initial measurement. Upon changing the solvent composition to 80% THF:20% H_2O a decrease in intensity is observed in both UV-vis and fluorescence emission. Upon addition of water both radiative and non-radiative rates change, and quantum efficiency drops from 57% to 27% as shown in **Table 2.3**. For 40% and 60% H_2O content, the further changes were minor in UV-Vis, fluorescence emission and in radiative and non-radiative rates. After increasing water content to 80%, significant drop in intensity in both UV-Vis and fluorescence emission, and quantum efficiency drops to 17%.

Table 2.3. Quantum yield and lifetime data in THF/H_2O mixture

THF/H_2O	**Φ**	**τ(ns)**	**k_{rad} (s^{-1})**	**k_{nr} (s^{-1})**
100/0	0.57	4.3	1.3×10^8	1.0×10^8
80/20	0.27	2.9	9.6×10^7	2.6×10^8
60/40	0.22	2.5	9.0×10^7	3.1×10^8
40/60	0.21	2.4	8.8×10^7	3.3×10^8
20/80	0.17	2.3	7.5×10^7	3.5×10^8

$$\Phi = \frac{k_{rad}}{k_{rad}+k_{nr}} \quad \text{and} \quad \tau = \frac{1}{k_{rad}+k_{nr}} \qquad \textbf{Equation 2.1}$$

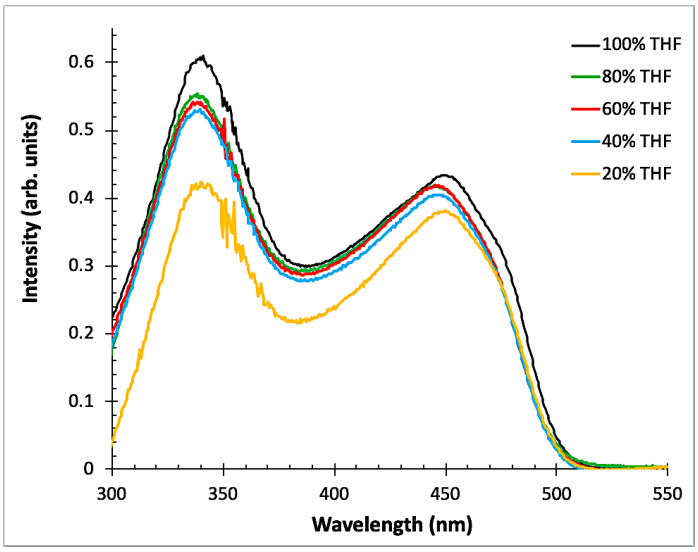

Figure 2.16. UV-Vis spectra of Si(bzimpy)$_2$ in solution of THF and water mixture.

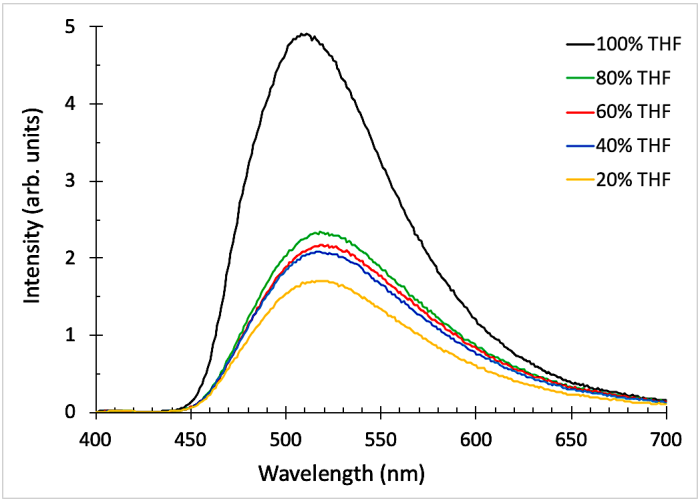

Figure 2.17. Fluorescence emission spectra of Si(bzimpy)$_2$ in solution of THF and water mixture.

The effect of water on optical properties of the molecule lead to the investigation of possible hydrolysis or other structural changes using ^{1}H NMR. The sample was prepared using THF-d8 and D_2O mixture in approximately 50:50 ratio. In **Figure 2.18** the initial spectrum and the sample after 56 hours do not show any structural difference, there are no new signals nor peak shifts observed. No changes were observed after 122 hours as well, as shown in **Figure 2.19**.

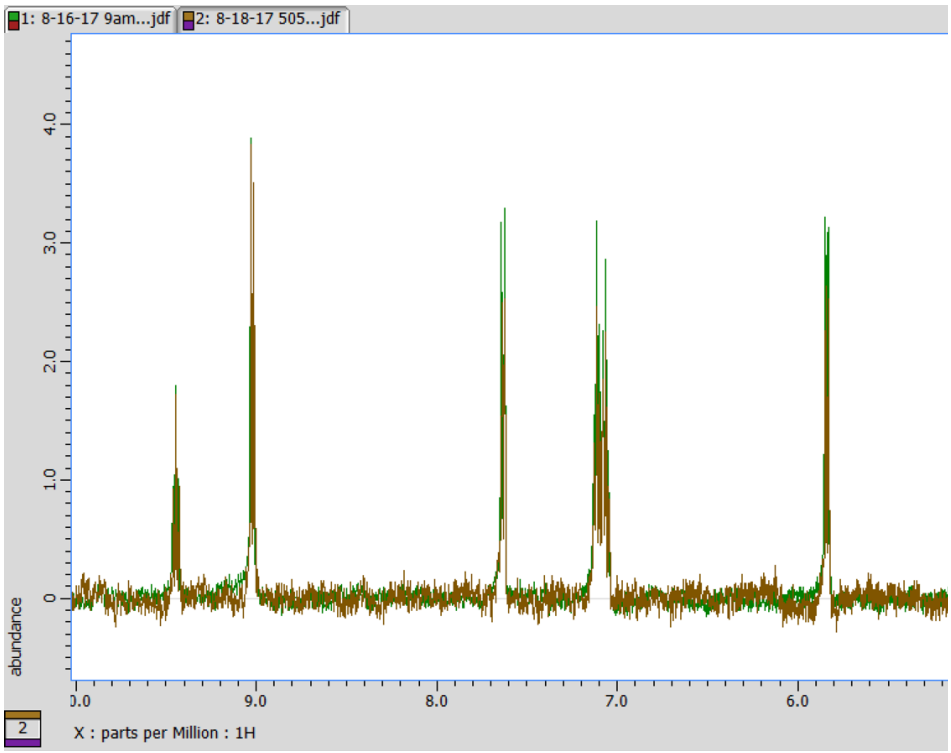

Figure 2.18. NMR spectrum of $Si(bzimpy)_2$ in solution of THF-d8 and D_2O mixture. (Green line – initial, brown line – after 56 hours in solution)

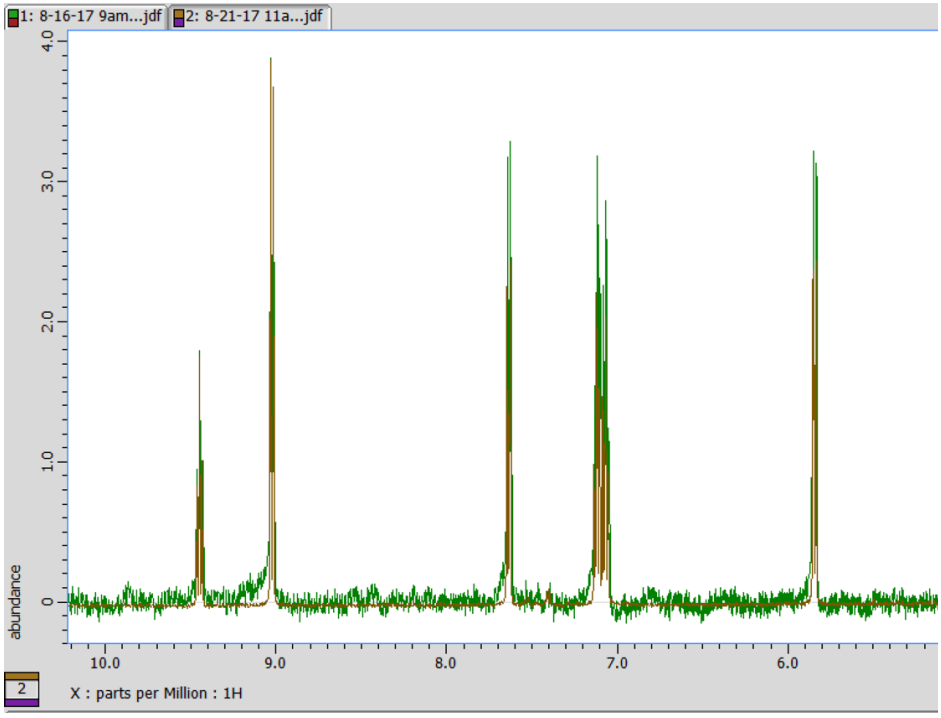

Figure 2.19. NMR spectrum of $Si(bzimpy)_2$ in solution of THF-d8 and D_2O mixture. (Green line – initial, brown line – after 122 hours in solution)

A quenching effect has been observed upon addition of HCl into solution of $Si(bzimpy)_2$ in THF. This process is reversable as can be seen in **Figure 2.20 c**. Three different pH ranges were selected to see the effect of HCl quenching on $Si(bzimpy)_2$ in solution. Black curve represents the initial excitation (**Figure 2.20 a**) and emission (**Figure 2.20 b**) at pH = 7 in THF/H_2O mixture. Upon addition of HCl, $Si(bzimpy)_2$ is significantly quenched, as seen in the excitation (**Figure 2.20 a**) and emission (**Figure 2.20 b**), as well as in the photo in **Figure 2.20 c** can be seen that there is no fluorescence emission from the vial with added HCl. The fluorescence emission can be recovered by adding base, such as $NaHCO_3$, and recovered emission can be seen in the **Figure 2.20 c**.

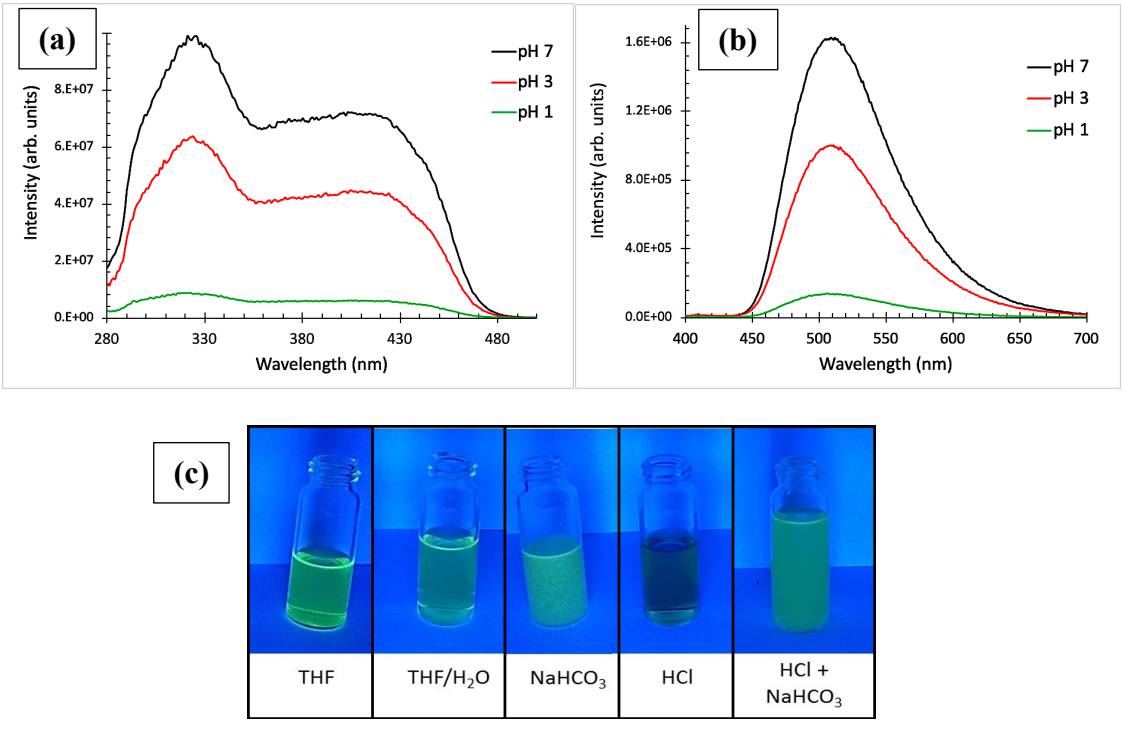

Figure 2.20. (a) Excitation spectra of $Si(bzimpy)_2$ in solution of THF and HCl to adjust to appropriate pH. (b) Fluorescence emission spectra of $Si(bzimpy)_2$ in solution of THF and HCl to adjust to appropriate pH. (c) Photos of $Si(bzimpy)_2$ in solution under UV-light (390-400 nm) of THF, and THF/H_2O mixture, $THF/H_2O/NaHCO_3$ mixture, $THF/H_2O/HCl$ mixture and $THF/H_2O/HCl/NaHCO_3$ mixture.

Some of the complexes in this study exhibit sensitivity to the polarity of the solvent. Fluorescence emission changes when different polarity solvent is used. The polar interactions lower the excited state energy, which results in the redshift of the emission, which is observed in the case of $Si(bzimpyMe)_2$ in solution shown in **Figure 2.21**, a similar effect was observed for $Si(bzimpyMe)_2$ in solution shown in **Figure 2.22.** In the case of $Si(bzimpyMe)_2$ the emission in the least polar solvent is observed at 531 nm and

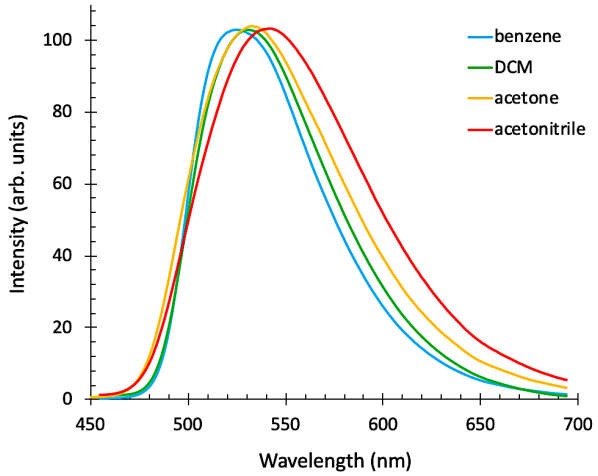

Figure 2.21. Effect of solvent polarity on fluorescence emission of $Si(bzipmyMe)_2$ in solution (Intensity is normalized).

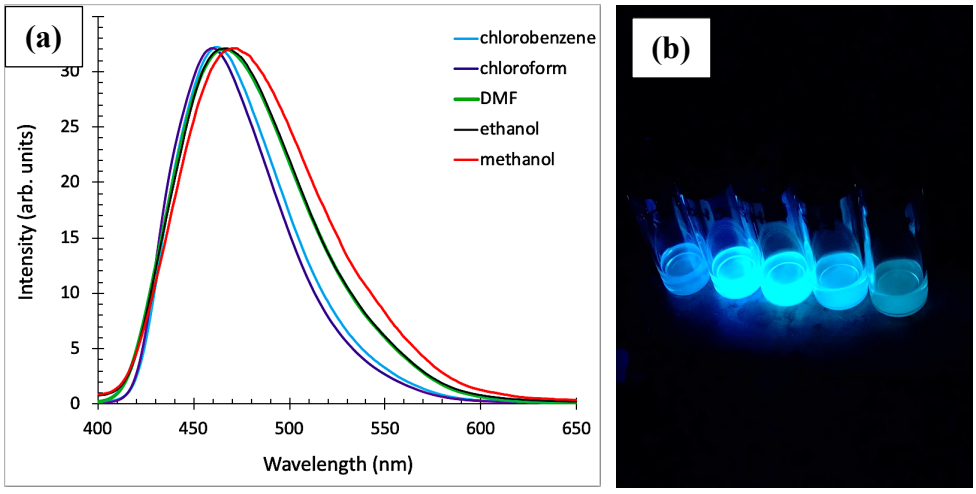

Figure 2.22. Effect of solvent polarity on fluorescence emission of $Si(bzipmyOMe)_2$ in solution (Intensity is normalized). (a) Fluorescence emission spectra (b) Photo of fluorescence emission of $Si(bzipmyOMe)_2$ in solution under UV light (390-400 nm LED). Solvents from left to right respectively: chlorobenzene, chloroform, DMF, ethanol, methanol.

in the most polar solvent is 547 nm. For $Si(bzimpyOMe)_2$ the emission in the least polar solvent is observed at 462 nm and in the most polar solvent is 471 nm.

The phosphorescence spectra of the four $Si(bzimpy)_2$ derivatives are shown in **Figure 2.43**. The samples were prepared by dissolving in dichloromethane and cooling with liquid nitrogen to 77 K. Blue 390-400 nm LED was used to excite the samples. The phosphorescence emission is significantly red shifted as shown in **Table 2.4**. The

Table 2.4. Tabulated peaks of fluorescence and phosphorescence emission of silicon complexes. The tabulated values for phosphorescence emission are listed based on the highest energy shoulder peaks.

Complex	Fluorescence emission at 77K (nm)	Phosphorescence emission at 77K (nm)	ΔE_{ST} (meV)
$Si(bzimpy)_2$	463	500	198
$Si(bzimpyMe)_2$	503	536	152
$Si(bzimpyOMe)_2$	515	545	133
$Si(bzimpyMeOMe)_2$	546	577	122

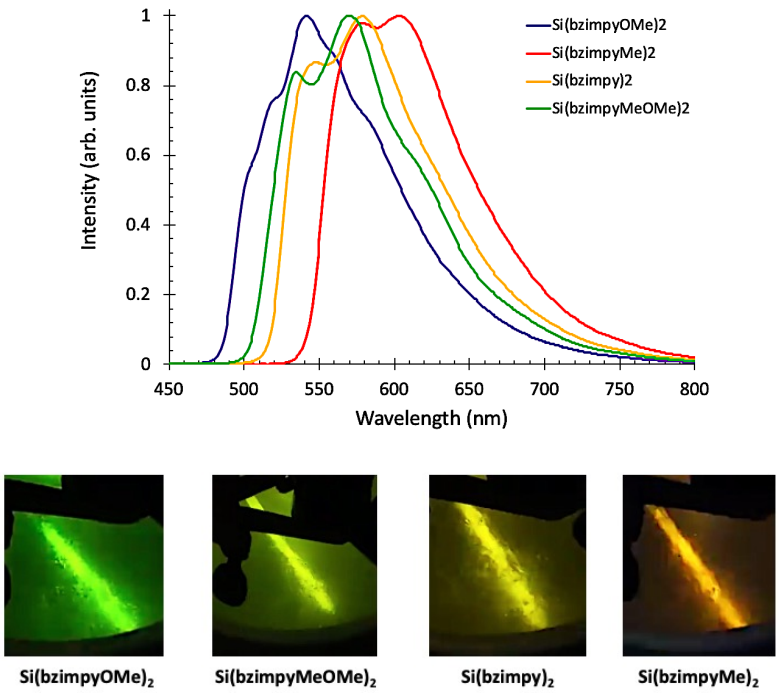

Figure 2.23. Phosphorescence emission spectra of complexes in dichloromethane at 77 K (Intensity is normalized). Phosphorescence emission photo images of complexes in solution at 77 K. The saturated solutions in dichloromethane were placed into glass NMR tubes and then into dewar with liquid nitrogen.

difference between the singlet and triplet states ΔE_{ST} based on the peak emission obtained experimentally is between 122-198 meV. The <100 meV requirement for TADF applications cannot be met with the demonstrated materials in this study, but there is a promising potential to modify these molecules to have desired ΔE_{ST} and these can potentially serve as the next generation materials for TADF applications. This was not of interest for this work, and is something to investigate further in the future.

2.4. Solid state characterization of complexes

The obtained hexacoordinate silicon complexes have demonstrated very high thermal stability for all six complexes. In this experiment thermal gravimetric analysis (TGA) was used to study the thermal stability. $Si(bzimpy)_2$ is stable up to 500 °C as shown by the TGA curve in **Figure 2.24**. $Si(bzimpyMe)_2$ is stable up to 570 °C as shown by the TGA curve in **Figure 2.25**. $Si(bzimpyOMe)_2$ is stable up to 400 °C as shown by

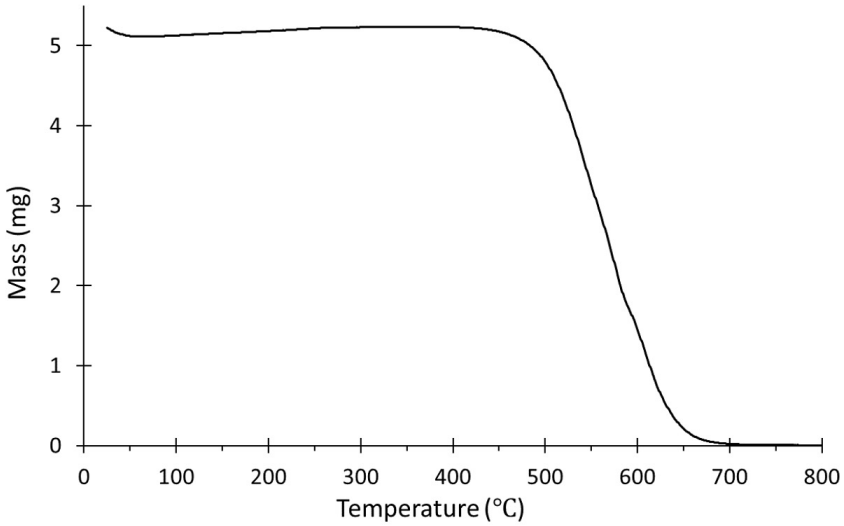

Figure 2.24. TGA spectrum of $Si(bzimpy)_2$ under nitrogen flow, blank corrected

the TGA curve in **Figure 2.26**. Si(bzimpyMeOMe)$_2$ is stable up to 410 °C as shown by the TGA curve in **Figure 2.42**. Si(BIP)$_2$ is stable up to 480°C as shown by the TGA curve in **Figure 2.28**. Si(IPI)$_2$ is stable up to 400 °C as shown by the TGA curve in **Figure 2.29**.

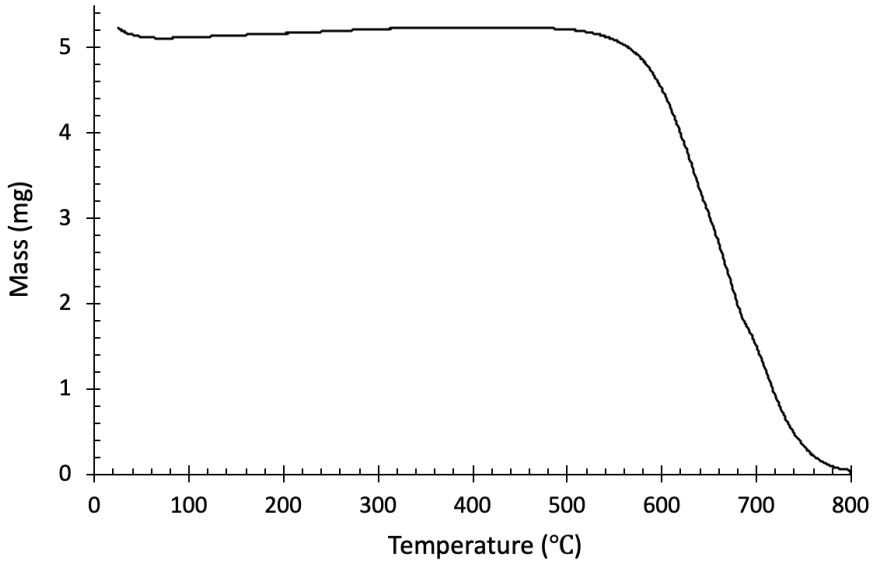

Figure 2.25. TGA spectrum of Si(bzimpyMe)$_2$ under nitrogen flow, blank corrected

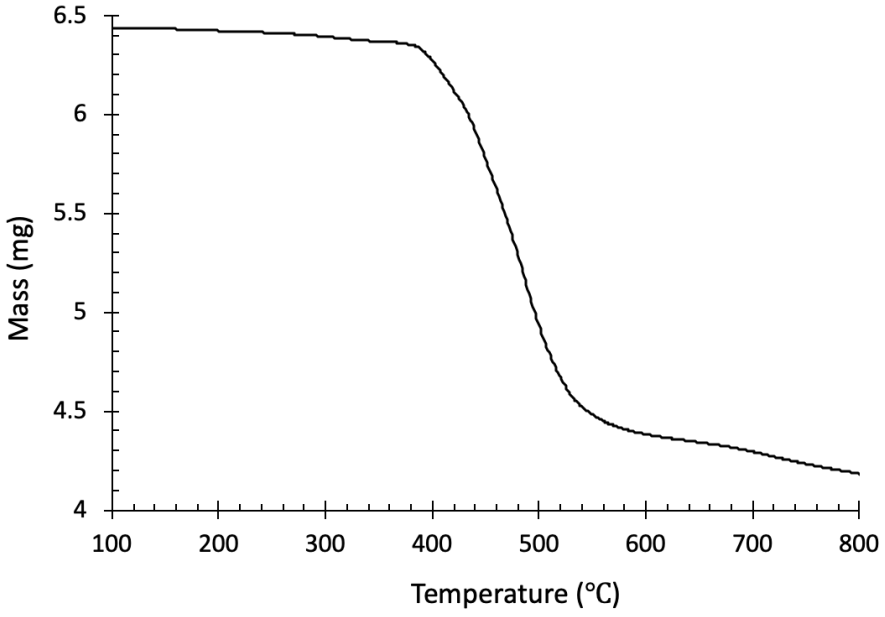

Figure 2.26. TGA spectrum of Si(bzimpyOMe)$_2$ under nitrogen flow.

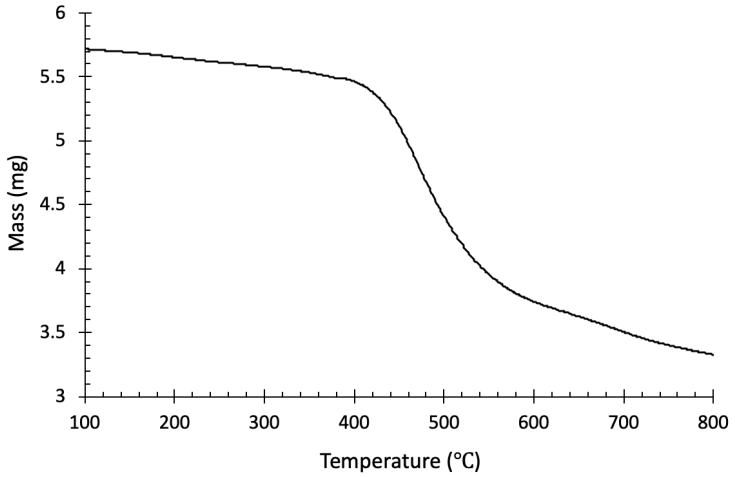

Figure 2.27. TGA spectrum of $Si(bzimpyMeOMe)_2$ under nitrogen flow

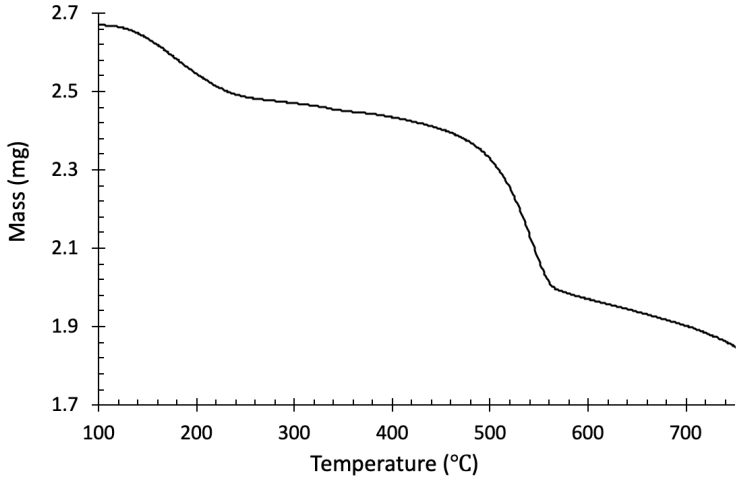

Figure 2.28. TGA spectrum of $Si(BIP)_2$ under nitrogen flow

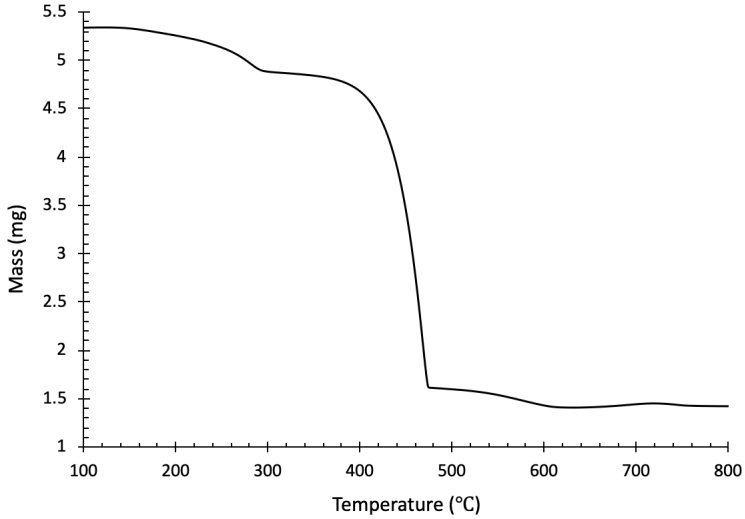

Figure 2.29. TGA spectrum of $Si(IPI)_2$ under nitrogen flow

Gradual stepwise temperature dependent fluorescence emission has been performed and is shown in **Figure 2.30**. A 45 nm film on glass substrate was heated on a hot plate in the presence of air for 10 min at each temperature indicated in **Figure 2.31** from 150 °C to 300 °C. A change in the fluorescence emission is observed after annealing at 200 °C, which corresponds to the start of glass phase transition. After annealing at 220 °C the emission blue shifts from initial 545 nm (the center of the peak) to 523 nm (the center of the peak). The blue shift along with the appearance of shoulders can be a sign of the film becoming more ordered upon annealing, or due to structural changes due to presence of oxygen in the atmosphere during annealing.

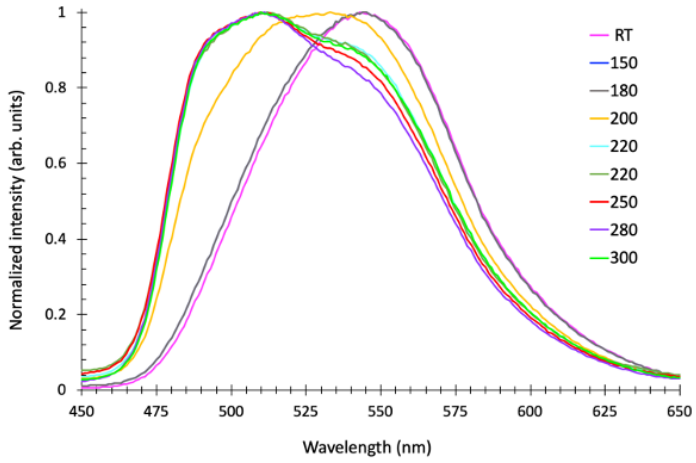

Figure 2.30. Effect of thermal annealing in air on fluorescence emission of $Si(bzipmy)_2$ 45 nm film. (Intensity is normalized). The films were annealed for 10 min on hot plate at each temperature, then cooled to room temperature for measurements.

The next set of annealing experiments were performed in nitrogen atmosphere, to exclude any chemical changes induced by the presence of moisture and/or oxygen. Thin film of $Si(bzimpy)_2$ 110 nm thickness was annealed at 300 °C for 10 min in the glovebox, then cooled to room temperature, after which the absorbance and fluorescence emission changes were measured and shown in **Figure 2.31**. Film absorption before annealing is

observed between 300 – 500 nm with two major peaks, one at 340 nm and second at 440 nm, and no noticeable shoulders observed. In the case of annealed film, one peak observed at 345 nm and second at 447 nm, and the appearance of three distinct shoulders can be observed. Fluorescence emission shown in **Figure 2.31 b**, the. Initial fluorescence emission peak, before annealing is centered at 549 nm and after annealing under nitrogen atmosphere the peak overall blue shifted to 544 nm, and the emission intensity significantly decreased and multiple shoulders appeared. These results are different from those obtained in presence oxygen and moisture in air, which leads to hypothesis that the packing of the film is changing.

The observations made via monitoring fluorescence emission suggest aggregate formation. Possible aggerates are shown in **Figure 2.32**, and the most appropriate description of the obtained data is the formation of the H-aggregate, where luminescence intensity is typically reduced, and blue shift in fluorescence emission is common.

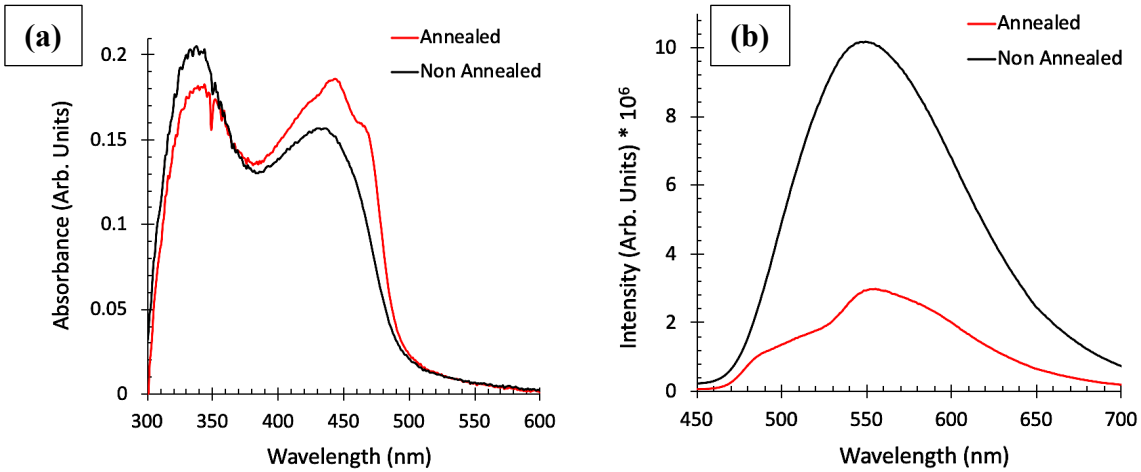

Figure 2.31. Effect of thermal annealing at 300 ºC in N_2 atmosphere of $Si(bzipmy)_2$ 110 nm film. The film was annealed for 10 min on hot plate, then cooled to room temperature for measurements. (a) UV-vis of the film before and after annealing. (b) fluorescence emission of the film before and after annealing.

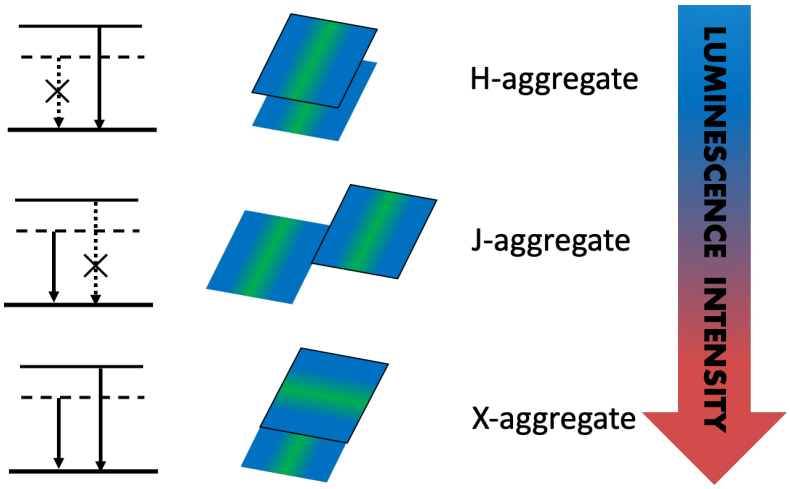

Figure 2.32. Possible aggregates that can be formed within the film.[55]

Thin film of Si(bzimpy)$_2$ of 110 nm was then further investigated to observe if the packing of the film was changing upon annealing. Raman spectra before and after annealing at 300 ºC for 10 min is shown in **Figure 2.33**. Although there are no significant shifts as shown in **Figure 2.33 b**, or differences in the peak location, the narrowing of the peaks' widths is be observed. This change can be attributed to change of the film packing, but it is inconclusive whether or not changes occurred. This led to further investigation of the film structure via atomic force microscopy (AFM).

The AFM images before and after annealing at 300 ºC for 10 min are shown in **Figure 2.34**. Top view of the film before annealing is shown in **Figure 2.34 a**, along with three-dimensional view of the surface. The surface roughness of the film as deposited is 3.6 nm, and the surface looks density packed, with fiber like structure. Upon annealing the surface appearance has changed, in the top view of the surface in **Figure 2.34 c** the surface looks island-like with variety of smaller and larger islands, along with appeared valleys. This can be further seen in three-dimensional view in **Figure 2.34 d**. The surface roughness after annealing was found to be 20.8 nm.

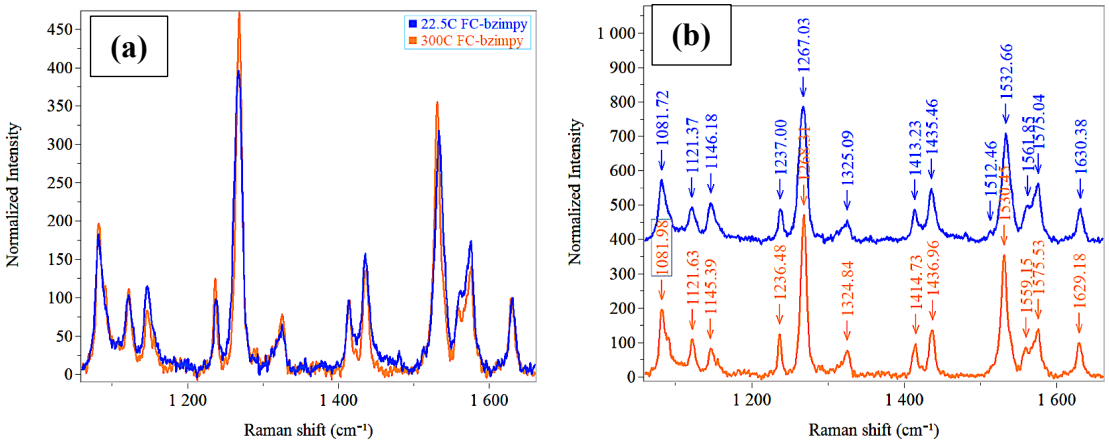

Figure 2.33. Effect of thermal annealing at 300 ºC in N_2 atmosphere of Si(bzipmy)$_2$ 110 nm film on Raman spectra (normalized 1630 cm^{-1} peak). The film was annealed for 10 min on hot plate, then cooled to room temperature for measurements. (a) Raman spectra of the film before (blue) and after annealing (orange) overlaid. (b) Raman spectra of the film before (blue) and after annealing (orange) with labeled peaks. Data acquired by Jose Castaneda.

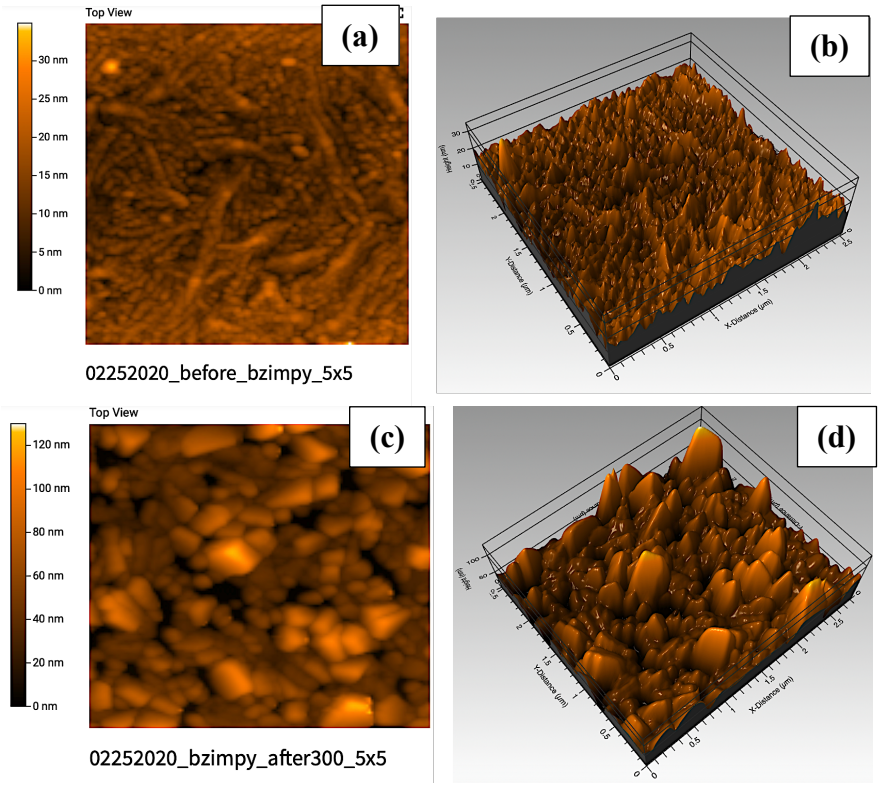

Figure 2.34. Effect of thermal annealing at 300 ºC in N_2 atmosphere of Si(bzipmy)$_2$ 110 nm film using AFM The film was annealed for 10 min on hot plate, then cooled to room temperature for measurements. (a) before annealing (b) after annealing

As a part of film characterization omega-2theta x-ray diffraction (XRD) scan was performed on $Si(bzimpy)_2$ 100 nm film as deposited on silicon substrate as shown in **Figure 2.35 b**, and the spectrum of which is shown in **Figure 2.35 a**. From obtained XRD pattern, there are no defined peaks, which is indicative of an amorphous film. In the obtain spectrum there is a broad peak which could be caused by the tape that film was taped with, as well as by disorder in the film, in the case of randomly oriented film domains.

From fluorescence emission, Raman, AFM, and XRD experiments can be concluded that films are predominantly amorphous as deposited, and most likely undergo some H-aggregate formation upon annealing. The structural change upon annealing results in decrease of fluorescence emission, and the increase in surface roughness, which can lead do worsening in device performance in the future due to increase chance of short-circuiting. Thus, for the purposes of applications in OLEDs and OPVs, the films will be used as deposited, without annealing.

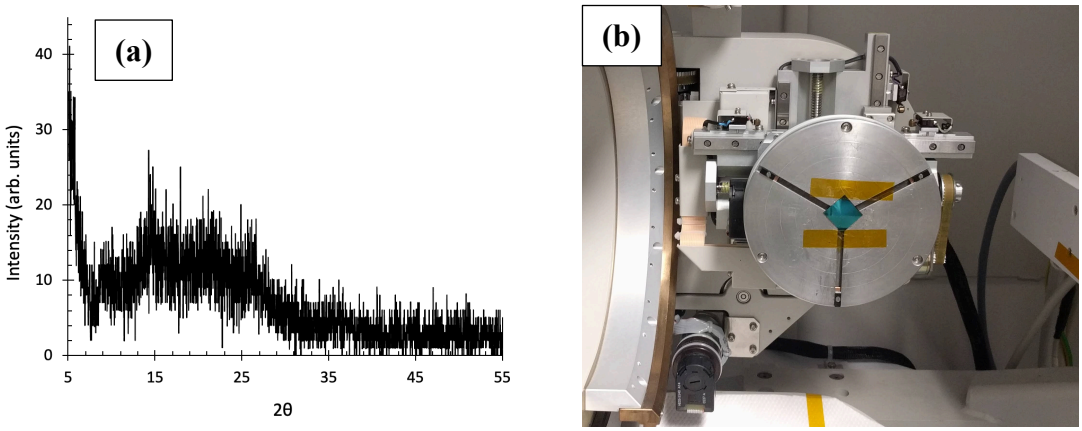

Figure 2.35. XRD omega-2theta of $Si(bzimpy)_2$ 100 nm film.

The problem of photobleaching is common among the organic materials. Comparison of response to photobleaching of widely used in organic electronics Alq_3 and

$Si(bzimpy)_2$ is shown in **Figure 2.56**. Both samples were prepared by making saturated solution in methanol, then filtering using 45 µm PTFE microfilter. Then samples were placed in a dark area and illuminated with UV lamp of 390-400 nm simultaneously. The fluorescence emission was measured after each exposure interval and is shown in **Figure 2.53 a** for Alq_3 and **Figure 2.36 b** for $Si(bzimpy)_2$. For Alq_3 noticeable reduction in fluorescence emission is observed after 2008 min of UV light exposure, while no reduction in the intensity of the emission is observed for $Si(bzimpy)_2$ over the same time of exposure period

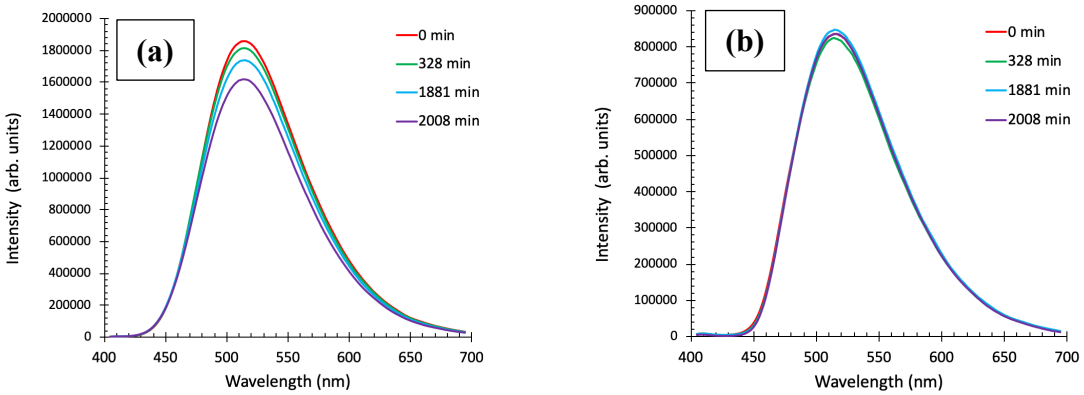

Figure 2.36. Effect of UV light exposure of complexes in solution of methanol at room temperature. (a) Fluorescence emission of Alq_3. (b) Fluorescence emission of $Si(bzipmy)_2$.

Photobleaching experiment was also performed in the solid state by exposing 90 nm films of Alq_3 and $Si(bzipmy)_2$ to 60 W/cm^2 and 440 W/cm^2 light source at 442 nm. The decay of the intensity of fluorescence emission is shown in **Figure 2.37**. In the case of 60 W/cm^2 light source the photodegradation is very similar for both materials, but $Si(bzipmy)_2$ shows less of emission intensity loss than Alq_3. The greater stability of $Si(bzipmy)_2$ in comparison to Alq_3 is especially noticeable in the case of exposure to higher intensity light of 440 W/cm^2. The intensity remains much greater over time for

Si(bzipmy)$_2$, which suggest that it will be a more stable material for applications in electronic devices.

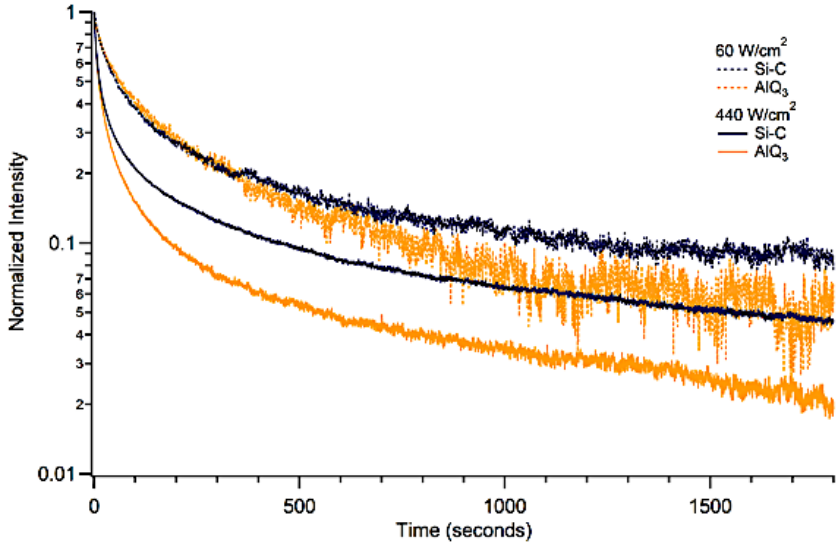

Figure 2.37. Effect of UV light exposure of complexes in solution of methanol at room temperature. Yellow line corresponds to the fluorescence emission of Alq3. Black line corresponds to the fluorescence emission of Si(bzipmy)$_2$. Data acquired by Jose Castaneda.

As a part of film characterization, AFM images are shown in **Figures 2.38-2.42** for all of the complexes. Surface images of 90 nm Si(bzimpy)$_2$ film are shown in **Figure 2.38 a**, top view of the surface, and **Figure 2.38 b**, three-dimensional view of the surface, where the surface roughness (root mean squared, RMS) across the film was found to be 0.3 nm. Surface images of 118 nm Si(bzimpyMe)$_2$ film are shown in **Figure 2.39 a**, top view of the surface, and **Figure 2.39 b**, three-dimensional view of the surface, where the surface roughness (RMS) across the film was found to be 0.6 nm. Surface images of 18 nm Si(bzimpyOMe)$_2$ film are shown in **Figure 2.40 a**, top view of the surface, and **Figure 2.40 b**, three-dimensional view of the surface, where the surface roughness (RMS) across the film was found to be 0.5 nm. Surface images of 27 nm Si(bzimpyMeOMe)$_2$ film are shown in **Figure 2.41 a**, top view of the surface, and

Figure 2.41 b, three-dimensional view of the surface, where the surface roughness (RMS) across the film was found to be 0.5 nm. Surface images of 90 nm $Si(IPI)_2$ film are shown in **Figure 2.42 a**, top view of the surface, and **Figure 2.42 b**, three-dimensional view of the surface, where the surface roughness (RMS) across the film was found to be 7.0 nm.

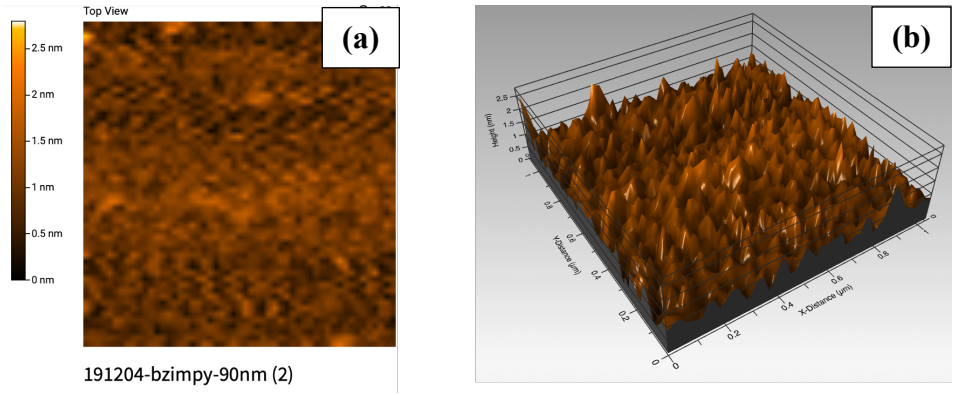

Figure 2.38. $Si(bzimpy)_2$ 90 nm film with 0.3 nm surface roughness.

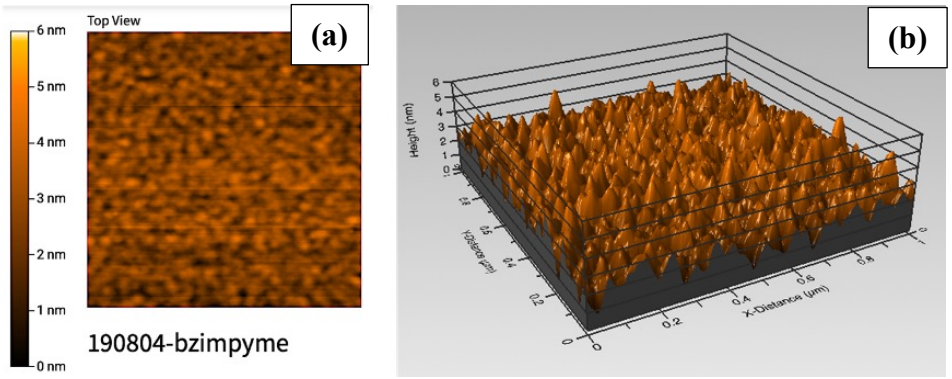

Figure 2.39. Si(bzimpyMe)2 118 nm film with 0.6 nm surface roughness

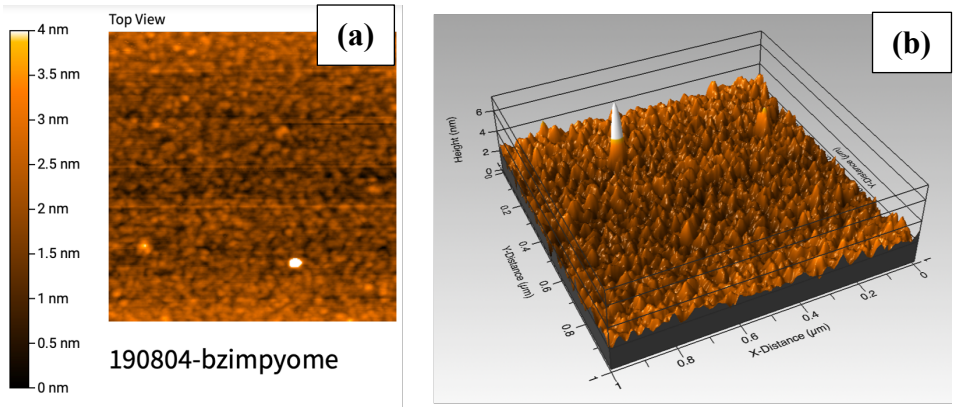

Figure 2.40. Si(bzimpyOMe)2 18 nm film with 0.5 nm surface roughness

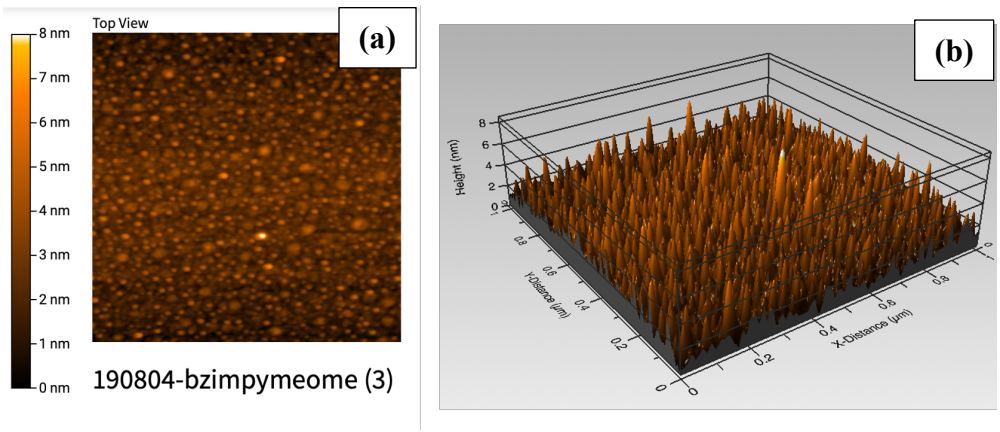

Figure 2.41. Si(bzimpyMeOMe)2 27 nm film with 0.5 nm surface roughness

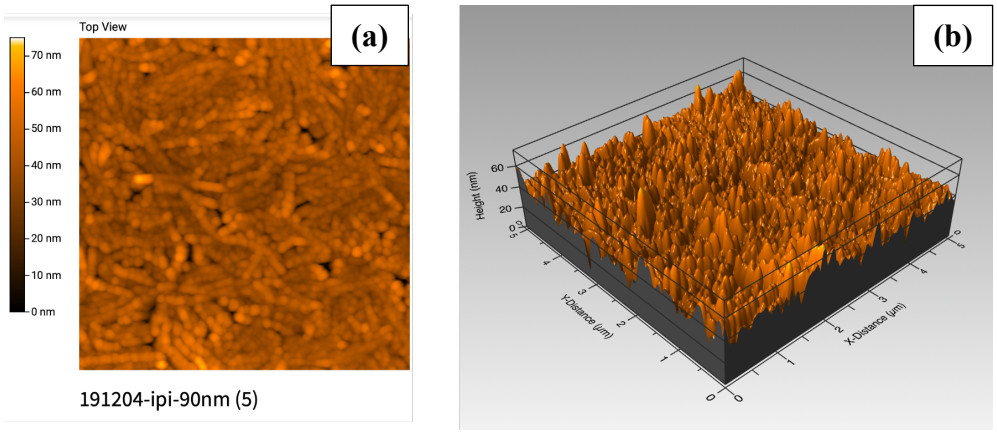

Figure 2.42. Si(IPI)2 90 nm film with 7.0 nm surface roughness

CHAPTER 3: PROTOTYPE ORGANIC ELECTRONIC DEVICES WITH HEXACOORDINATE SILICON COMPLEXES

3.1. Electron mobility

Electron mobility devices were assembled using $Si(bzimpy)_2$, $Si(bzimpyMe)_2$, $Si(bzimpyOMe)_2$, $Si(bzimpyMeOMe)_2$, and $Si(IPI)_2$. Due to challenges with obtaining $Si(BIP)_2$ films, it was not possible to assemble prototype devices using this complex. All of the devices were assembled using design shown in **Figure 3.1**, to allow injection, transport and collection of electrons, and measure carrier mobility for each of the materials. For each of the materials three top performing devices are reported. It is also important to know that thicknesses of $Si(pincer)_2$ complexes were very different, in some cases three times thinner than others, which can be partially attributed to why the charge transport was lower for these films.

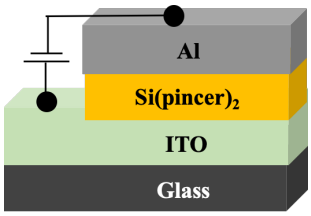

Figure 3.1. Device structure of electron only devices to measure electron mobility using SCLC method.

Patterned OLED substrates with 100 nm indium tin-oxide (ITO) coated glass (from Ossila) of area of pixel equal to $2.97 \cdot 10^{-6}$ m^2 with sheet resistance of 20 Ω/square were first cleaned by ultrasonication for 15 min in each of the following solvents: deionized water, acetone, and isopropanol. Then dried with nitrogen flow, and treated in a UV/ozone ProCleaner for 15 min. The substrates were then quickly transferred to the glovebox with nitrogen atmosphere for thermal evaporation of materials. The thermal evaporation was performed under ultra-high vacuum of 10^{-6} mbar using a MB-EVAP

system inside a MBRAUN glovebox and controlled with a SQC-310C Deposition Controller. The rate of evaporation along with thickness of $Si(pincer)_2$ complexes are listed in **Table 3.1.** After deposition of the active layer, cathode layer is applied. Aluminum was used as cathode and was deposited onto the substrate by thermal evaporation at a rate of 0.20 Å/s for the first 20 nm and 2.0 Å/s for 20-150 nm. The total thickness of the aluminum layer was 150 nm for all of the devices.

Table 3.1. Rate of deposition, and total thickness for active layers of electron transport devices.

Material	Rate (Å/s)	Thickness (nm)
$Si(bzimpy)_2$	0.20	92
$Si(bzimpyMe)_2$	0.30-0.40	89
$Si(bzimpyOMe)_2$	0.01-0.10	14
$Si(bzimpyMeOMe)_2$	0.01-0.10	35
$Si(IPI)_2$	0.02-0.05	29

The highest electron mobility was found to be in $Si(bzimpy)_2$ with average mobility of $1.17 \times 10^{-4} \pm 2.51 \times 10^{-5}$ cm^2/Vs, and representative curves of the three top performing devices are shown in **Figure 3.2**. Such high carrier mobility can be attributed to potentially better packing of the molecules within the film, which would support the charge hopping mechanism, and lower the risk of pinholes, which would interrupt the charge transport. It is also important to note that depending on the orientation of the molecules, either hole or electron transport can be favored, since molecules can align with the intermolecular stacking where: 1) LUMOs of two or more molecules overlap; 2) HOMOs of two or more molecules overlap; or 3) HOMO of one molecule would overlap with LUMO of neighboring molecule. According to previous observations of no

particular orientation, and films looking rather amorphous, it is possible that the films have molecules aligned in a manner of all three possibilities, and everything in-between.

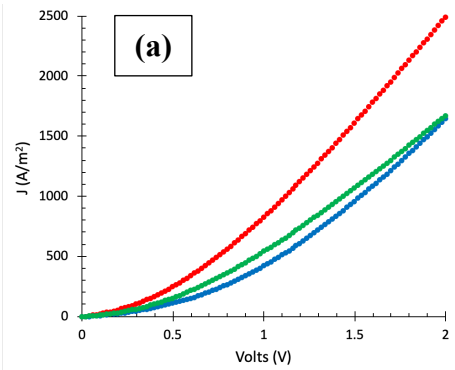

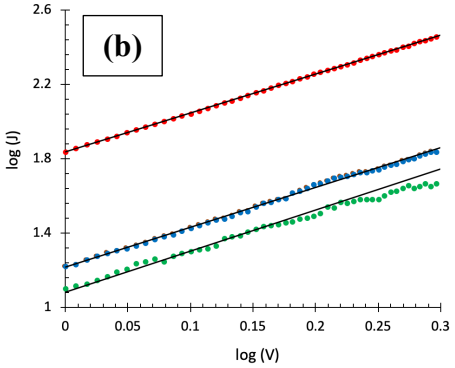

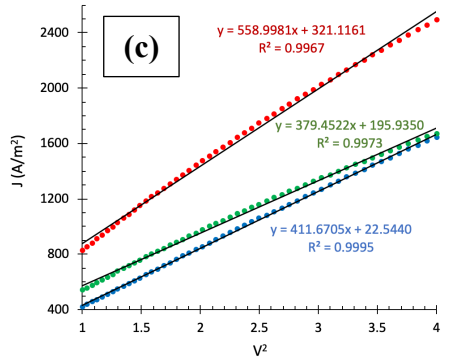

Color	Slope (A/V^2m^2)	R^2	mobility (cm^2/Vs)
Red	559.00	0.9967	1.46×10^{-4}
Green	379.45	0.9973	9.89×10^{-5}
Blue	411.67	0.9995	1.07×10^{-4}

Figure 3.2. (a) J-V curve of ITO/Si(bzimpy)$_2$/Al devices. (b) log(J)-log(V) curve of ITO/Si(bzimpy)$_2$/Al devices. (c) J-V^2 curve of ITO/Si(bzimpy)$_2$/Al devices. Electron mobilities were calculated from slopes of lines in graph 3.2 c.

The lowest electron mobility was found to be in Si(bzimpyOMe)$_2$ with average mobility of $3.05 \times 10^{-8} \pm 2.87 \times 10^{-8}$ cm^2/Vs, and representative curves are shown in **Figure 3.3**. Lower carrier mobility can be assigned to potentially the molecules being not as tightly packed in the film due to the film being significantly thinner, only 14 nm, while Si(bzimpy)$_2$ was 92 nm thick.

Complex Si(bzimpyMe)$_2$ also demonstrated high average mobility of $4.94 \times 10^{-5} \pm 2.04 \times 10^{-5}$ cm^2/Vs, and representative curves are shown in **Figure 3.4**. Film thickness for these films was 89 nm, which is more comparable to Si(bzimpy)$_2$, and the lower mobility is probably a result of greater spacing between the molecules due to increased

bulkiness on the backbone of benzimidazoles due to presence of methyl groups. These spacers prevent molecules to pack very tightly, even in the case when they are well aligned.

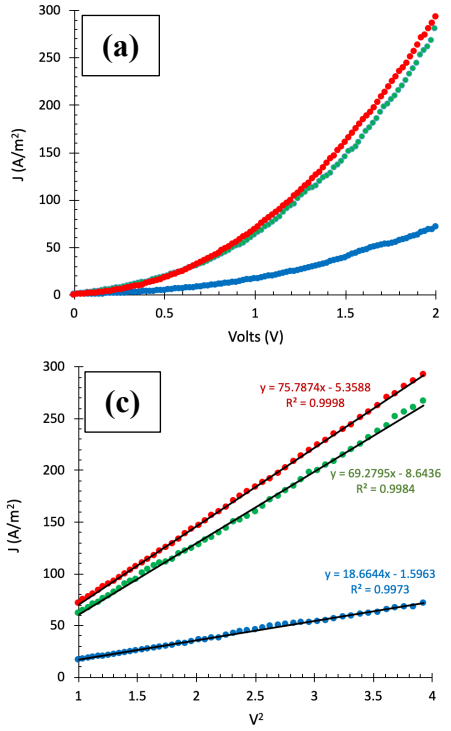

Color	Slope (A/V^2m^2)	R^2	mobility (cm^2/Vs)
Red	75.79	0.9998	6.96×10^{-8}
Green	69.28	0.9984	6.36×10^{-8}
Blue	18.66	0.9973	1.71×10^{-8}

Figure 3.3. (a) J-V curve of ITO/Si(bzimpyOMe)$_2$/Al devices. (b) log(J)-log(V) curve of ITO/Si(bzimpy)$_2$/Al devices. (c) J-V^2 curve of ITO/Si(bzimpy)$_2$/Al devices. Electron mobilities were calculated from slopes of lines in graph 3.3c.

Electron mobilities of Si(bzimpyMeOMe)$_2$, shown in **Figure 3.5**, and Si(IPI)$_2$ shown in **Figure 3.6** were found to be in between the lowest and the highest performing materials, and were determined to be $1.46 \times 10^{-6} \pm 6.30 \times 10^{-7}$ cm^2/Vs, and $5.21 \times 10^{-6} \pm 8.53 \times 10^{-7}$ cm^2/Vs for Si(bzimpyMeOMe)$_2$ and Si(IPI)$_2$, respectively. These were both relatively thin films of 35 and 29 nm for Si(bzimpyMeOMe)$_2$ and Si(IPI)$_2$, accordingly. As in previous cases, the molecules in the films are most likely randomly oriented, which can influence the carrier mobility.

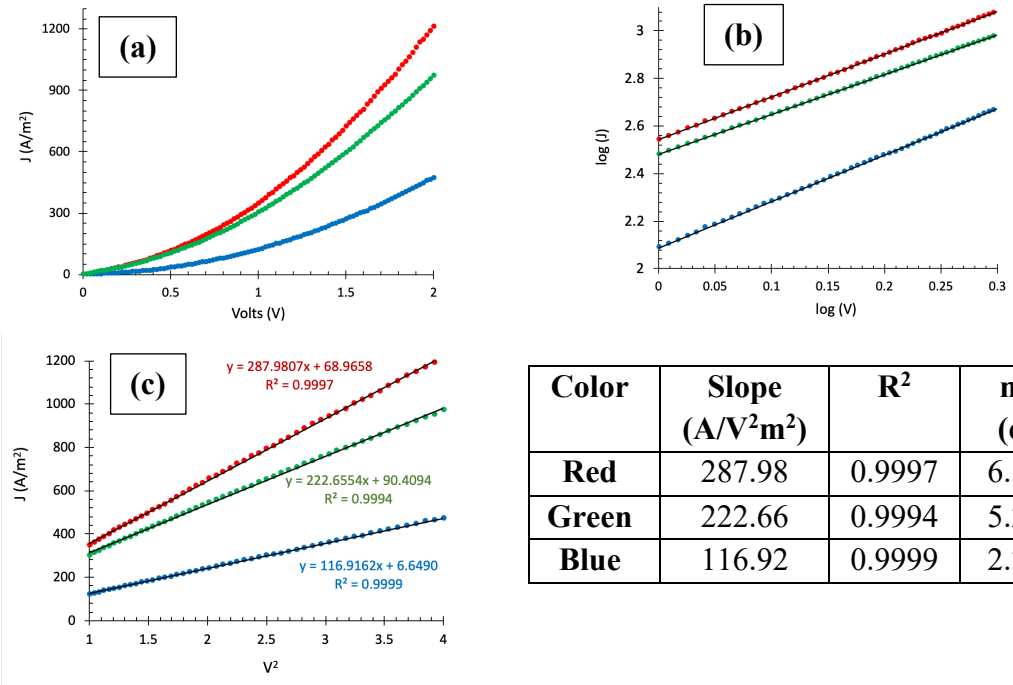

Color	Slope (A/V^2m^2)	R^2	mobility (cm^2/Vs)
Red	287.98	0.9997	6.80×10^{-5}
Green	222.66	0.9994	5.26×10^{-5}
Blue	116.92	0.9999	2.76×10^{-5}

Figure 3.4. (a) J-V curve of ITO/Si(bzimpyMe)$_2$/Al devices. (b) log(J)-log(V) curve of ITO/Si(bzimpy)$_2$/Al devices. (c) J-V^2 curve of ITO/Si(bzimpy)$_2$/Al devices. Electron mobilities were calculated from slopes of lines in graph 3.4c.

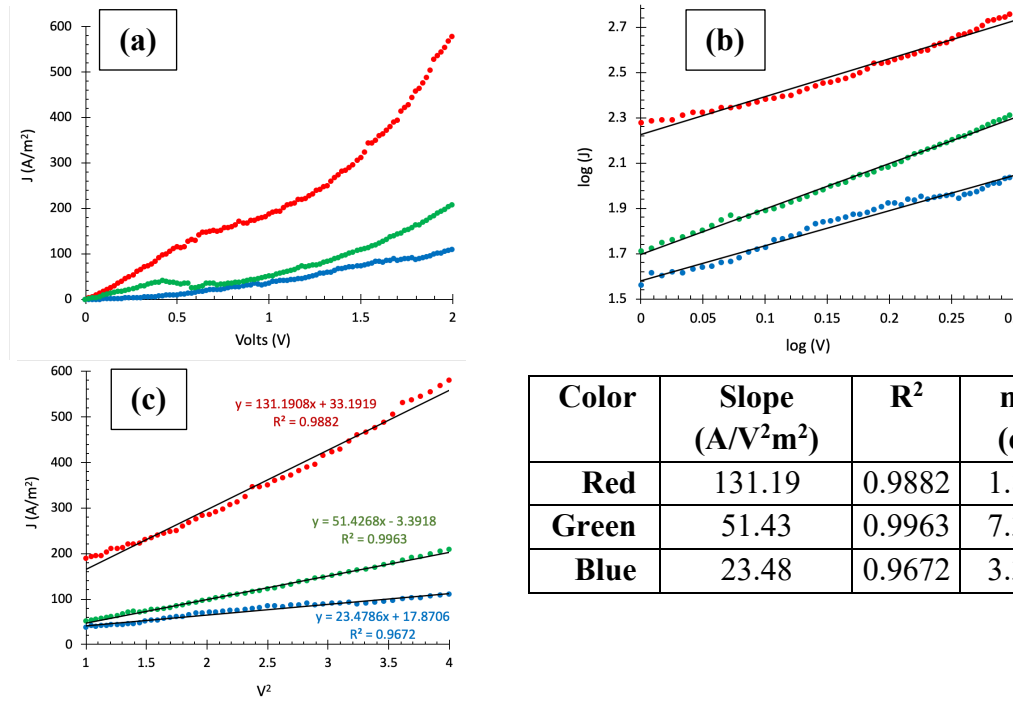

Color	Slope (A/V^2m^2)	R^2	mobility (cm^2/Vs)
Red	131.19	0.9882	1.88×10^{-6}
Green	51.43	0.9963	7.38×10^{-7}
Blue	23.48	0.9672	3.37×10^{-7}

Figure 3.5. (a) J-V curve of ITO/Si(bzimpyMeOMe)$_2$/Al devices. (b) log(J)-log(V) curve of ITO/Si(bzimpy)$_2$/Al devices. (c) J-V^2 curve of ITO/Si(bzimpy)$_2$/Al devices. Electron mobilities were calculated from slopes of lines in graph 3.5c.

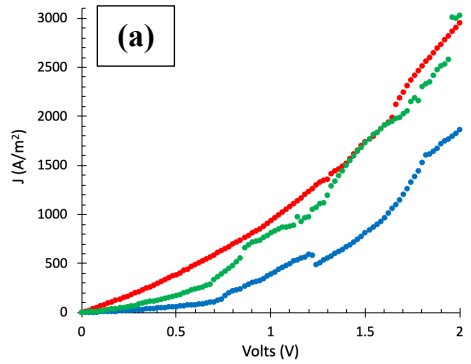

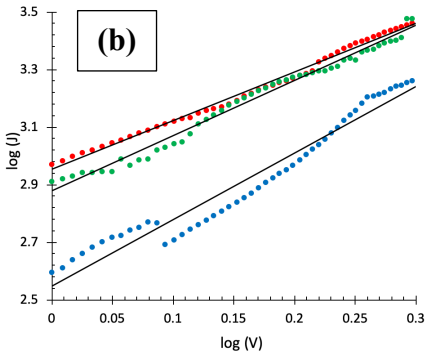

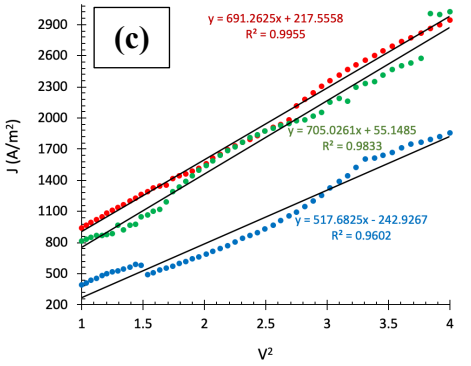

Color	Slope (A/V^2m^2)	R^2	mobility (cm^2/Vs)
Red	691.26	0.9955	1.64×10^{-6}
Green	705.03	0.9833	4.23×10^{-6}
Blue	517.68	0.9602	5.76×10^{-6}

Figure 3.6. (a) J-V curve of ITO/Si(IPI)$_2$/Al devices. (b) log(J)-log(V) curve of ITO/Si(bzimpy)$_2$/Al devices. (c) J-V^2 curve of ITO/Si(bzimpy)$_2$/Al devices. Electron mobilities were calculated from slopes of lines in graph 3.6c.

3.2 Hole mobility

The next set of devices were assembled to measure hole transport of Si(bzimpy)$_2$, Si(bzimpyMe)$_2$, Si(bzimpyOMe)$_2$, Si(bzimpyMeOMe)$_2$, and Si(IPI)$_2$. All of the devices were prepared using design shown in **Figure 3.7**, to allow injection, transport and collection of holes, and measure carrier mobility for each of the materials. For each of the materials three top performing devices are reported. The thicknesses of films with Si(pincer)$_2$ complexes vary significantly, in some cases three times thinner than others, which may contribute to lowering of charge transport for these devices.

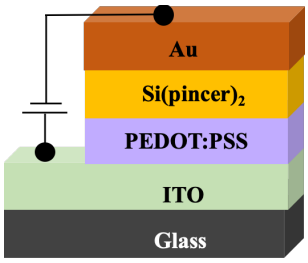

Figure 3.7. Device structure of hole only devices.

Patterned OLED substrates were used to make the devices and prepared as discussed in section 3.1. The substrates were then quickly transferred to the glovebox with nitrogen atmosphere for thermal evaporation of materials, or were used to spin coat PEDOT:PSS in ambient conditions. PEDOT:PSS solution was filtered through a 0.45 µm PES filter into a vial, then placed along with prepared ITO glass on a hot plate and heated to 55 °C prior to spin coating. The ITO glass was spun at 2000 rpm in a spin coater for 40 s, and 90 µL of PEDOT:PSS solution was deposited onto the slide. The film was allowed to dry for 3 min at room temperature. A second layer of PEDOT:PSS was added by spin coating 90 µL onto the substrate at 2000 rpm for 40 s, slides were room temperature. The anode portion of the device was then wiped with a cotton swab dipped in water to remove PEDOT:PSS. The films were then annealed at 140 °C for 10 min on a hot plate inside an N_2 filled glove box.

The thermal evaporation was performed under ultra-high vacuum of 10^{-6} mbar using a MB-EVAP system inside a MBRAUN glovebox and controlled with a SQC-310C Deposition Controller. The rate of evaporation along with thickness of Si(pincer)$_2$ complexes are listed in **Table 3.2.** After deposition of the active layer, cathode layer is

applied. Gold was used as cathode, and was deposited onto the substrate by thermal evaporation at a rate of 0.20-0.25 Å/s until total thickness of 50 nm.

Table 3.2. Rate of deposition, and total thickness for active layers of electron transport devices.

Material	Rate (Å/s)	Thickness (nm)
$Si(bzimpy)_2$	0.20	91
$Si(bzimpyMe)_2$	0.30-0.40	115
$Si(bzimpyOMe)_2$	0.01-0.10	21
$Si(bzimpyMeOMe)_2$	0.01-0.10	35
$Si(IPI)_2$	0.02-0.05	29

The highest hole mobility was found to be for $Si(bzimpy)_2$ with average mobility of $1.07 \times 10^{-5} \pm 5.99 \times 10^{-6}$, and representative curves are shown in **Figure 3.8**. $Si(bzimpy)_2$ also had the highest electron mobility. Such ability to be good carrier for both electrons and holes may be due to films being amorphous. As discussed earlier, the molecules can align with the intermolecular stacking where: 1) LUMOs of two or more molecules overlap; 2) HOMOs of two or more molecules overlap; or 3) HOMO of one molecule would overlap with LUMO of neighboring molecule. Thus, ability to almost equally be good ETM and HTM can be due to mix of alignment of the molecules, which are tightly packed.

The hole mobility in the case of $Si(bzimpyMe)_2$, is slightly lower than electron mobility. The average hole mobility was found to be $2.56 \times 10^{-6} \pm 5.48 \times 10^{-8}$ cm^2/Vs, and representative curves are shown in **Figure 3.9**. The molecules are likely to be oriented in the film to favor electron mobility in this case. More evidence would be needed to confirm if there is a more organized structure to the film present or not.

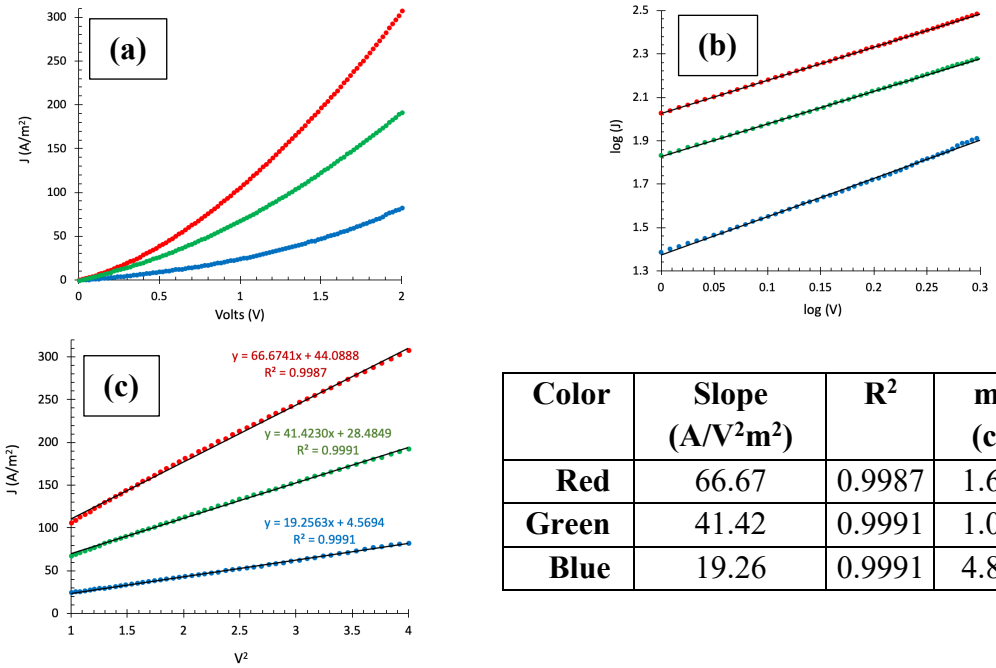

Color	Slope (A/V^2m^2)	R^2	mobility (cm^2/Vs)
Red	66.67	0.9987	1.68×10^{-5}
Green	41.42	0.9991	1.05×10^{-5}
Blue	19.26	0.9991	4.86×10^{-6}

Figure 3.8. (a) J-V curve of ITO/PEDOT:PSS/Si(bzimpy)$_2$/Au devices. (b) log(J)-log(V) curve of ITO/Si(bzimpy)$_2$/Al devices. (c) J-V^2 curve of ITO/Si(bzimpy)$_2$/Al devices. Hole mobilities were calculated from slopes of lines in graph 3.8 c.

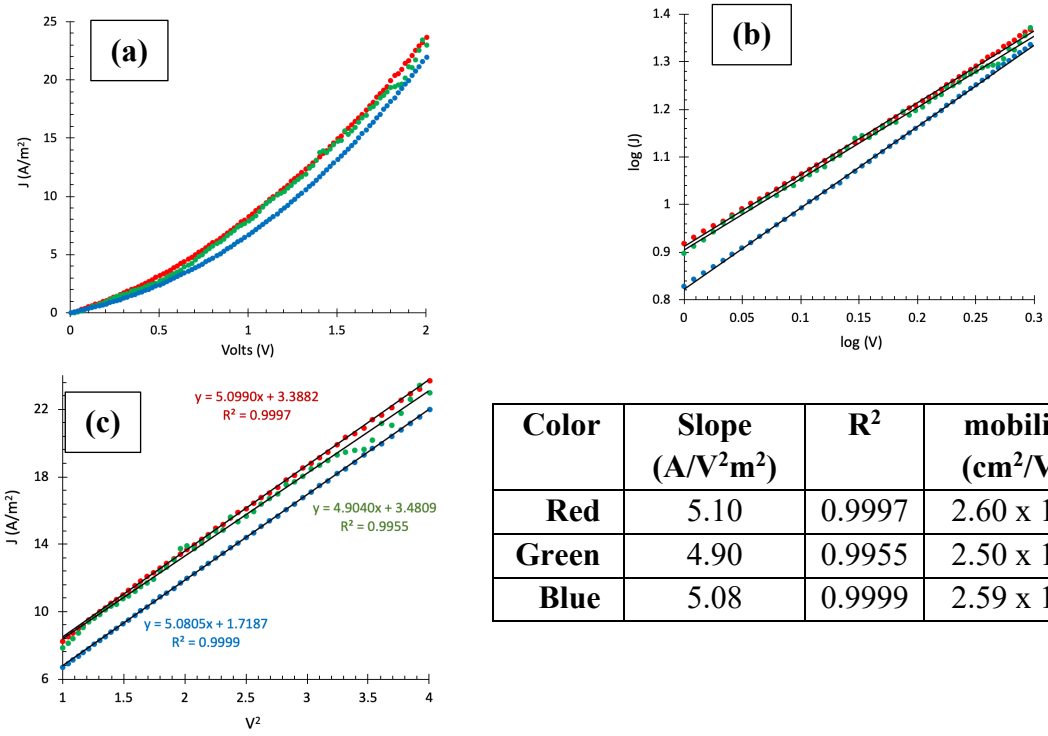

Color	Slope (A/V^2m^2)	R^2	mobility (cm^2/Vs)
Red	5.10	0.9997	2.60×10^{-6}
Green	4.90	0.9955	2.50×10^{-6}
Blue	5.08	0.9999	2.59×10^{-6}

Figure 3.9. (a) J-V curve of ITO/PEDOT:PSS/Si(bzimpyMe)$_2$/Au devices. (b) log(J)-log(V) curve of ITO/Si(bzimpy)$_2$/Al devices. (c) J-V^2 curve of ITO/Si(bzimpy)$_2$/Al devices. Hole mobilities were calculated from slopes of lines in graph 3.9 c.

Similarly to electron mobility, the lowest hole mobility was found to be in Si(bzimpyOMe)$_2$ with average mobility of 2.60 x 10^{-8} ± 5.60 x 10^{-9} cm^2/Vs, and representative curves are shown in **Figure 3.10**. Similarly, the film was significantly thinner, only 18 nm, while Si(bzimpy)$_2$ was 90 nm thick. The molecules are also potentially not packed as tightly and with more random orientation, resulting in lower carrier mobilities.

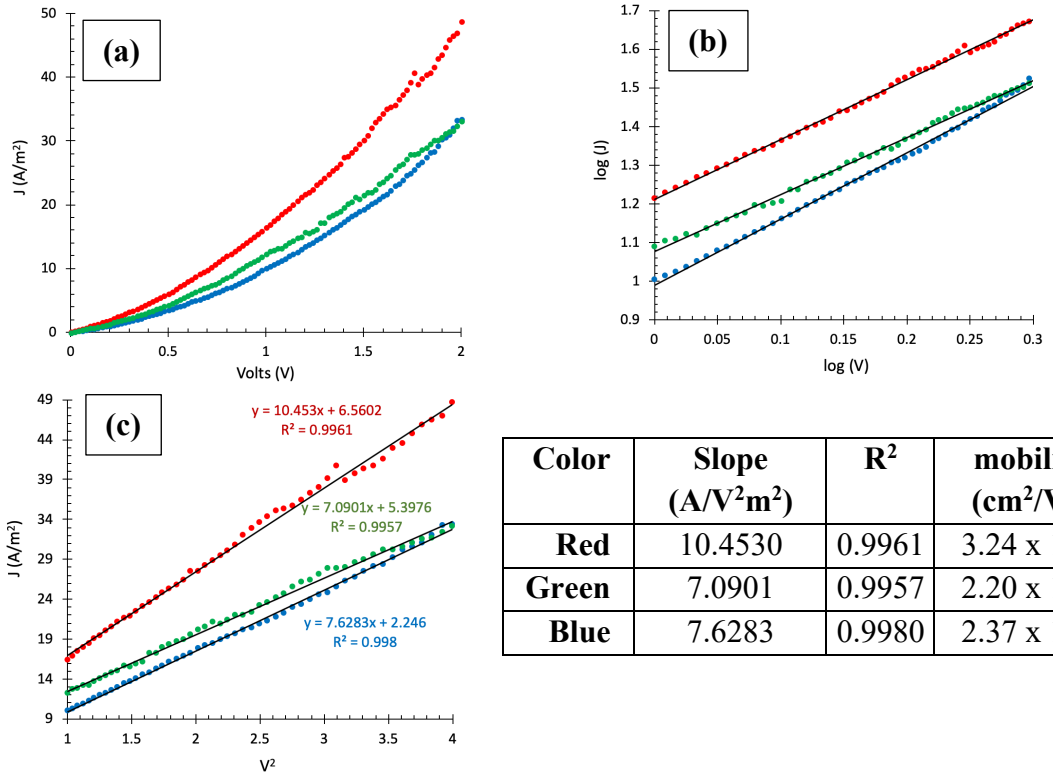

Color	Slope (A/V^{2}m^2)	R^2	mobility (cm^2/Vs)
Red	10.4530	0.9961	3.24 x 10^{-8}
Green	7.0901	0.9957	2.20 x 10^{-8}
Blue	7.6283	0.9980	2.37 x 10^{-8}

Figure 3.10. (a) J-V curve of ITO/PEDOT:PSS/Si(bzimpyOMe)$_2$/Au devices. (b) log(J)-log(V) curve of ITO/Si(bzimpy)$_2$/Al devices. (c) J-V^2 curve of ITO/Si(bzimpy)$_2$/Al devices. Hole mobilities were calculated from slopes of lines in graph 3.10 c.

T Hole mobilities of Si(bzimpyMeOMe)$_2$, shown in **Figure 3.11**, and Si(IPI)$_2$ shown in **Figure 3.12** were found to be the second highest performing materials, and were determined to be 3.84 x 10^{-6} ± 5.39 x 10^{-6} cm^2/Vs, and 9.60 x 10^{-6} ± 3.57 x 10^{-7} cm^2/Vs for Si(bzimpyMeOMe)$_2$ and Si(IPI)$_2$, respectively. As in previous cases, the

molecules in the films are most likely randomly oriented, which can influence the carrier mobility to be equal for both electrons and holes. Both of the materials can be promising ambipolar hosts, with rate being identical for both electrons and holes. To better compare both electron and hole mobilities of all materials that were studied, all values are listed side by side in **Table 3.3**. In comparison to commercially available materials listed in **Table 3.3**, Si(pincer)$_2$ complexes have competitive electron and hole transport rates, and provide improved thermal, chemical, and photostability.

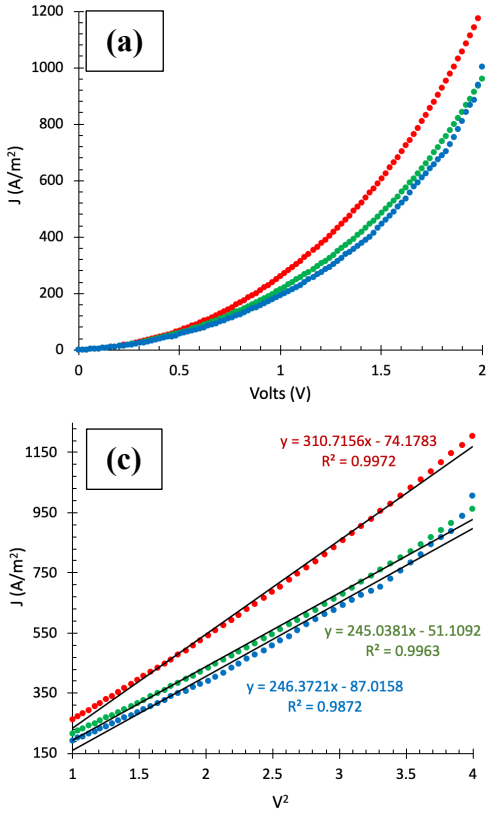

Color	Slope (A/V^2m^2)	R^2	mobility (cm^2/Vs)
Red	310.72	0.9972	4.46×10^{-5}
Green	245.04	0.9963	3.52×10^{-6}
Blue	246.37	0.9872	3.54×10^{-6}

Figure 3.11. (a) J-V curve of ITO/PEDOT:PSS/Si(bzimpyMeOMe)$_2$/Au devices. (b) log(J)-log(V) curve of ITO/Si(bzimpy)$_2$/Al devices. (c) J-V^2 curve of ITO/Si(bzimpy)$_2$/Al devices. Hole mobilities were calculated from slopes of lines in graph 3.11 c.

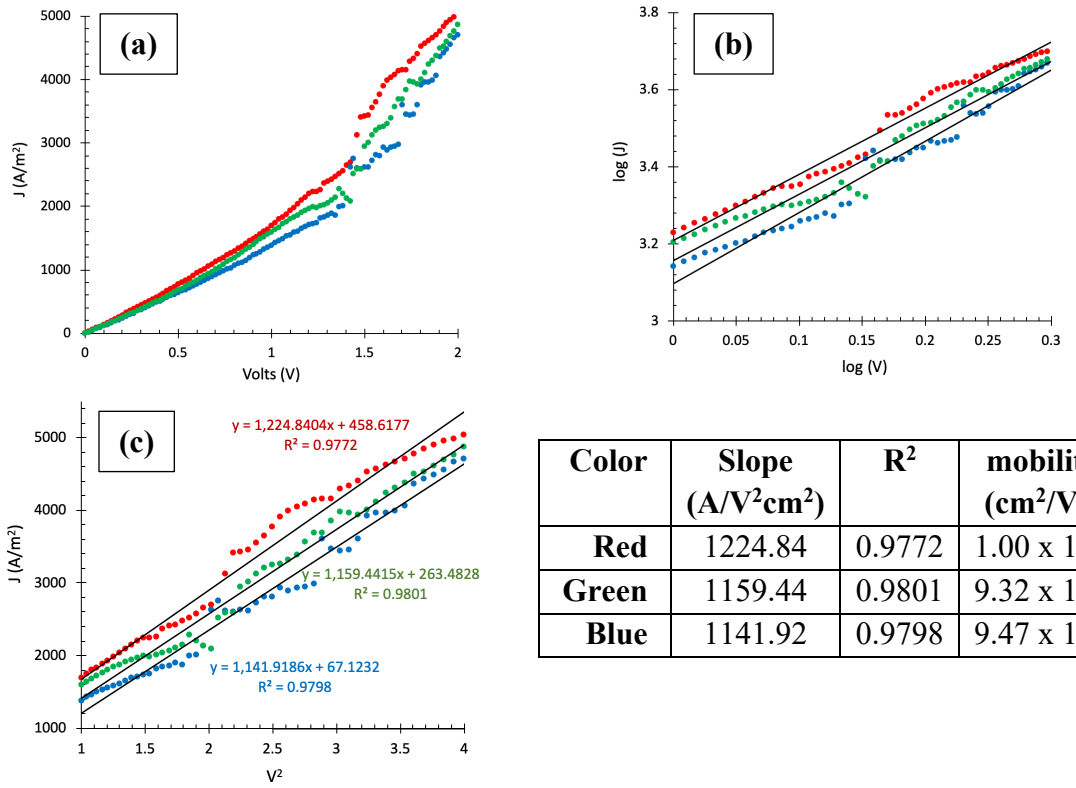

Color	Slope (A/V^2cm^2)	R^2	mobility (cm^2/Vs)
Red	1224.84	0.9772	1.00×10^{-5}
Green	1159.44	0.9801	9.32×10^{-6}
Blue	1141.92	0.9798	9.47×10^{-6}

Figure 3.12. (a) J-V curve of ITO/PEDOT:PSS/$Si(IPI)_2$/Au devices. (b) log(J)-log(V) curve of ITO/$Si(bzimpy)_2$/Al devices. (c) J-V^2 curve of ITO/$Si(bzimpy)_2$/Al devices. Hole mobilities were calculated from slopes of lines in graph 3.11 c.

Table 3.3. Electron and hole mobility averages of three top performing devices for each of the complex using SCLC method, including mobility ranges of some of the commercial materials.

Complex Name	*Electron Mobility (cm^2/Vs)*	*Hole Mobility (cm^2/Vs)*
$Si(bzimpy)_2$	$1.17 \times 10^{-4} \pm 2.51 \times 10^{-5}$	$1.07 \times 10^{-5} \pm 5.99 \times 10^{-6}$
$Si(bzimpyMe)_2$	$4.94 \times 10^{-5} \pm 2.04 \times 10^{-5}$	$2.56 \times 10^{-6} \pm 5.48 \times 10^{-8}$
$Si(bzimpyOMe)_2$	$3.05 \times 10^{-8} \pm 2.87 \times 10^{-8}$	$2.60 \times 10^{-8} \pm 5.60 \times 10^{-9}$
$Si(bzimpyMeOMe)_2$	$1.46 \times 10^{-6} \pm 6.30 \times 10^{-7}$	$3.84 \times 10^{-6} \pm 5.39 \times 10^{-6}$
Si $(IPI)_2$	$5.21 \times 10^{-6} \pm 8.53 \times 10^{-7}$	$9.60 \times 10^{-6} \pm 3.57 \times 10^{-7}$
Alq_3	10^{-6}- 10^{-7} *[56]	10^{-8} - 10^{-10} *[57]
Bphen	10^{-4}- 10^{-5} *[58]	
NPB	10^{-6}- 10^{-8} *[59, 60]	10^{-4}- 10^{-5} *[60, 61]

CHAPTER 4: PROTOTYPE ORGANIC ELECTRONIC DEVICES WITH HEXACOORDINATE SILICON COMPLEXES

4.1. Organic light emitting diodes

OLED substrates were prepared as described in the section 3.1.1, then materials were thermally evaporated in the order shown in **Figures 4.1** OLED device prototyping started with design similar to the first ever reported OLED device design reported by Tang and VanSlyke, but instead of Alq_3 use $Si(pincer)_2$ complexes.[13] The OLED device was assembled according to Generation 1 design shown in **Figure 4.1**. After substrates were cleaned, $Si(bzimpy)_2$ was deposited at the rate of 0.5-0.8 Å/s to obtain 78 nm film. Aluminum was used as the cathode and was deposited on top of $Si(bzimpy)_2$ via thermal evaporation at the rate of 0.20 Å/s for the first 20 nm and 2.0 Å/s for the rest of the deposition. The total thickness of the aluminum layer was 300 nm.

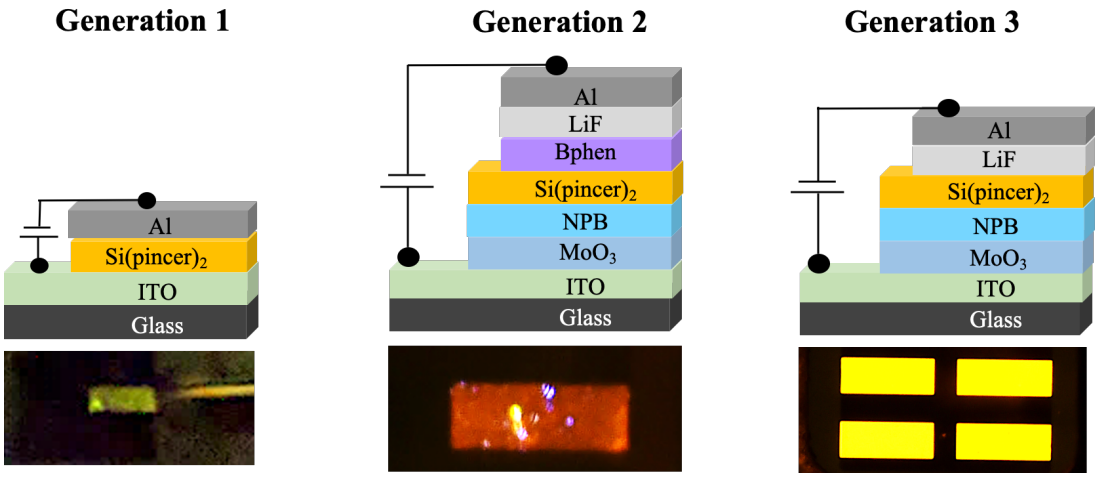

Figure 4.1. Three generations of OLED architecture.

Although, 1st generation architecture resulted in successful electroluminescence, after applying bias voltage of 12 V, with λ_{max} = 560 nm the emission lasted only for 1 min. Comparison of photoluminescence (PL) and electroluminescence (EL) of the

Si(bzimpy)$_2$ film is shown in **Figure 4.2**. This successful light emission inspired Generation 2 device design shown in **Figure 4.1**.

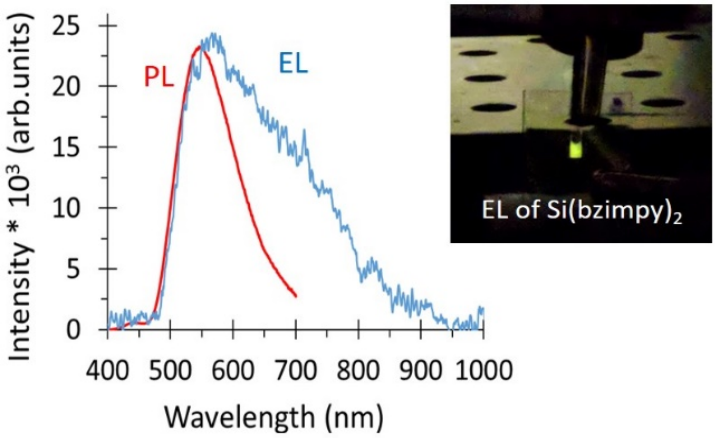

Figure 4.2. Photo- and electroluminescence of first-generation OLED using Si(bzimpy)$_2$.

Multiple versions of second-generation devices were tested to find the optimal architectural design to use for the rest of the devices using other Si(pincer)$_2$ complexes. Four iterations of OLED Generation 2 devices are shown in **Figure 4.4**. The materials were deposited at the rate and thickness reported in **Table 4.1** and assembled in the order shown in **Figure 4.4**. The devices were then tested by applying a ramping bias voltage until 13 V, and their electroluminescence was recorded for each illuminating device, shown in **Figure 4.4**. Due to issues with capturing Generation 2-3 device, there is no representative photo shown. All of the measured devices had a dominant peak emission centered at 750 nm, which corresponds to NIR region. Besides the dominant peak, there are additional, much smaller in intensity peaks present in the visible region.

The peak at 750 nm does not correspond to the excitonic emission of Si(bzimpy)$_2$, since this emission does not come from the excited state of Si(bzimpy)$_2$ monomer. Instead it is observed from excited dimer, commonly called excimer or electromer, which

Table 4.1. Rate of deposition, and total thickness for active layers of OLED devices.

Material	Rate (Å/s)	Thickness (nm)
MoO_3	0.18-0.21	10
$Si(bzimpy)_2$	0.25-0.30	60
NPB	0.10-0.90	90
Bphen	0.05-0.90	30
LiF	0.13-0.16	7
Al	0.35-0.40 up to 30 nm, then 1.2	150

is formed between a molecule that donates electrons and molecule that accepts electrons. This results in excited state that is lower in energy than excited state of a monomer. In the case of dissimilar molecules, the excited state of the complex is called exciplex. The exciplex formation can be generated optically or electrically. In the devices demonstrated in Generation 2, the emission is obtained only in the cases of application of bias voltage, in the case of optical excitation of $Si(bzimpy)_2$ and NPB (N,N′-Di(1-naphthyl)-N,N′-diphenyl-(1,1′-biphenyl)-4,4′-diamine) together, no low energy emission is observed. In electroluminescence, electrically generated electron-hole pairs then can have cross transitions between different molecules and radiatively emit, resulting in modification of emission spectrum. Such electron-hole pairs are called electromers or electroplexes.[62]

There are many ways to obtain exciplex or electroplex, which are shown in **Figure 4.3**. Donor and acceptor must be present, they can be either two different materials, or within the same molecule. Based on carrier mobility experiments, $Si(bzimpy)_2$ can be thought of as a n-type acceptor or bipolar acceptor, which would correspond to the case shown in **Figure 4.3 a** or **Figure 4.3 b**, due to NPB being p-type donor. In recent years, the trend had switched from achieving improvement in device

performance by addition of emissive components to reduction of emissive components by using excimers, exciplexes, electroplexes, or electromers.[41, 63]

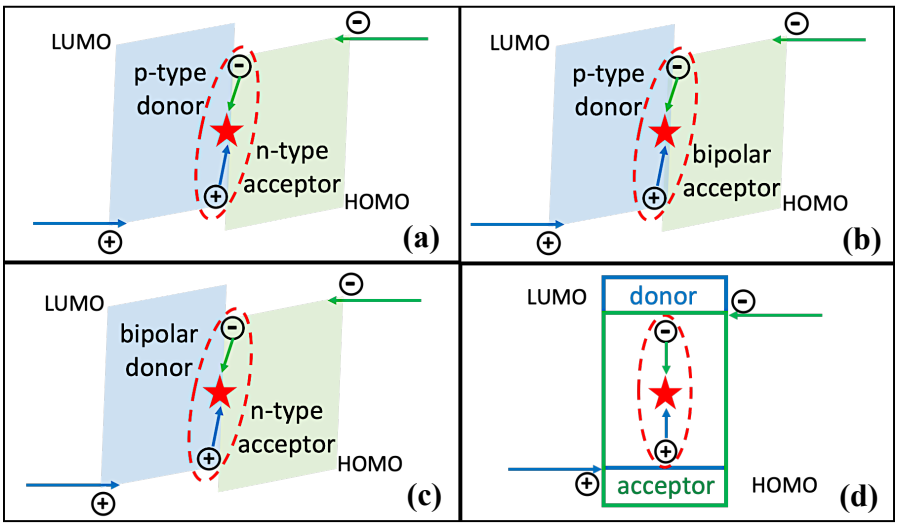

Figure 4.3. Scheme of exciplex or electroplex formation. This figure was inspired by the work reported by Xiao *et.al*. The red star represents exciplex or electroplex formation, green arrow electron transport, and blue arrow hole transport.[41]

Generation 2 devices show that it is possible to achieve both exciton and electroplex emission using $Si(bzimpy)_2$ as n-type acceptor, and NPB as a p-type donor. In the case of Generation 2-1 and Generation 2-2 devices, the difference is that Generation 2-2 includes MoO_3 as hole injection layer. Separate hole injection layer was added to observe improvement in performance lifetime and brightness of the devices. The overall emission intensity of the peak at 750 nm is greater in device that does not have additional layer of MoO_3, and the peak at 530 nm remains the same in intensity. The lifetime of the device without MoO_3 was significantly shorter, on the order of 4-5 min at operating voltage of 13 V. While Generation 2-2 had slight loss in luminescence, the lifespan of the devices increased to 12-14 min.

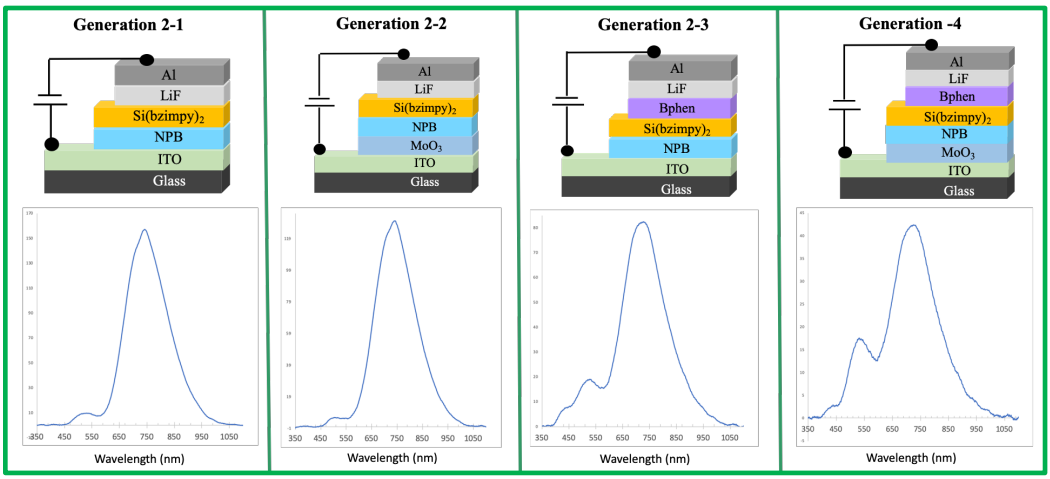

Figure 4.4. Variations of the second generation of OLED architecture.

Generation 2-3 and Generation 2-4 devices included Bphen (bathophenanthroline) as electron injection layer, and the difference between them is that Generation 2-3 does not include MoO_3 layer, while Generation 2-4 does. The addition of Bphen as an electron injection/electron transport layer to see how $Si(bzimpy)_2$ performance as emitter would change. Similar emission intensity changes are observed, without MoO_3 layer 750 nm peak is more intense, while 530 nm stays the same. In this set of devices there is additional peak observed at 440 nm, intensity of which also is not influenced with presence of MoO_3 layer. This peak was not present in Generation 2-1 and 2-2, there is observable patchiness of films, where blue emission and yellow emission is observed separately, this can be due to film uniformity issues due to challenges upon deposition of Bphen. These devices had lifetime on the order of 6-7 min for Generation 2-3 and 8-9 min Generation 2-4 for at operating voltage of 13 V.

From results obtained from Generation 2 devices the most optimal balance between device lifetime and brightness of the emission was the Generation 2-2. Based on these results Generation 3 devices were assembled and tested for complexes $Si(bzimpy)_2$,

$Si(bzimpyMe)_2$, $Si(bzimpyOMe)_2$, and $Si(bzimpyMeOMe)_2$. The devices were assembled as shown in **Figure 4.1**, and deposition rates and thicknesses are listed in **Table 4.2**.

Table 4.2. Rate of deposition, and total thickness for active layers of OLED devices.

Material	Rate (Å/s)	Thickness (nm)
MoO_3	0.18-0.21	10
$Si(bzimpy)_2$	0.25-0.30	90
$Si(bzimpyMe)_2$	0.10-0.40	77
$Si(bzimpyOMe)_2$	0.02-0.15	21
$Si(bzimpyMeOMe)_2$	0.02-0.10	35
NPB	0.10-0.90	31, for $Si(bzimpyMeOMe)_2$ device thickness was 55
LiF	0.13-0.16	7
Al	0.35-0.40 up to 30 nm, then 1.2	150

The electro- and photoluminescence of all assembled OLED devices are shown in **Figure 4.5**. The contribution of excitonic and electroplex emission varies in the obtained devices. The film thickness in devices was supposed to be as similar as possible between all four devices, but it was not achieved due to differences in material properties and ability to make thicker films. Therefore, it will not be possible to exclude the influence of thickness differences on device properties. All of the device electroluminescence emissions were recorded at applied bias voltage of 12 V. One of the most notable observations is intensity of excitonic emission. Black line in **Figures 4.5 a - 4.5 d** represents the photoluminescence of corresponding $Si(pincer)_2$ films, which had been normalized to the maximum peak emission in the electroluminescence, which is represented by green line.

For device with $Si(bzimpyMe)_2$, **Figure 4.5 a**, the excitonic peak contribution at 575 nm is greater than low energy emission peak at approximately 645 nm, which

overlaps with excitonic emission. To the eye this OLED looks bright yellow as shown in the photo in **Figure 4.5 a**. This device had the longest performance lifetime, and the longest performing device was illuminating for 14 min at 15 V.

Device with Si(bzimpyMeOMe)$_2$, shown in **Figure 4.5 b**, the excitonic peak contribution at 530 nm is equal to the low energy emission peak at 630 nm. Light observed to the eye looks close to white light, and in the photo can be seen a slight green tint resulting in greenish white illumination. These did not have as high performance longevity and had the shortest performance. At 15 V the longest performing device was illuminating for 5 min before the burn out.

For OLED device assembled with Si(bzimpy)$_2$, spectrum of which is shown in **Figure 4.5 c**, the excitonic peak contribution at 540 nm is much lower in intensity than the low energy emission peak at 750 nm. These pixels appear to have bright orange emission to the eye, as shown in the photo in **Figure 4.5 c**, this is probably due to color mixing of the yellow excitonic emission, and deeper red emission of the electroplex emission. These devices also had longer performance lifetime, at 16 V the longest performing device was illuminating for 12 min.

For device with Si(bzimpyOMe)$_2$, **Figure 4.5 d**, the excitonic contribution cannot be distinguished in the obtained spectrum, and only the low energy emission peak at 930 nm is observed. This is very different than for the rest of the devices, the low energy emission is significantly more intense than for the rest of the devices, and there is no visible to the eye emission. The longest performing device was illuminating for 10 min at 15 V.

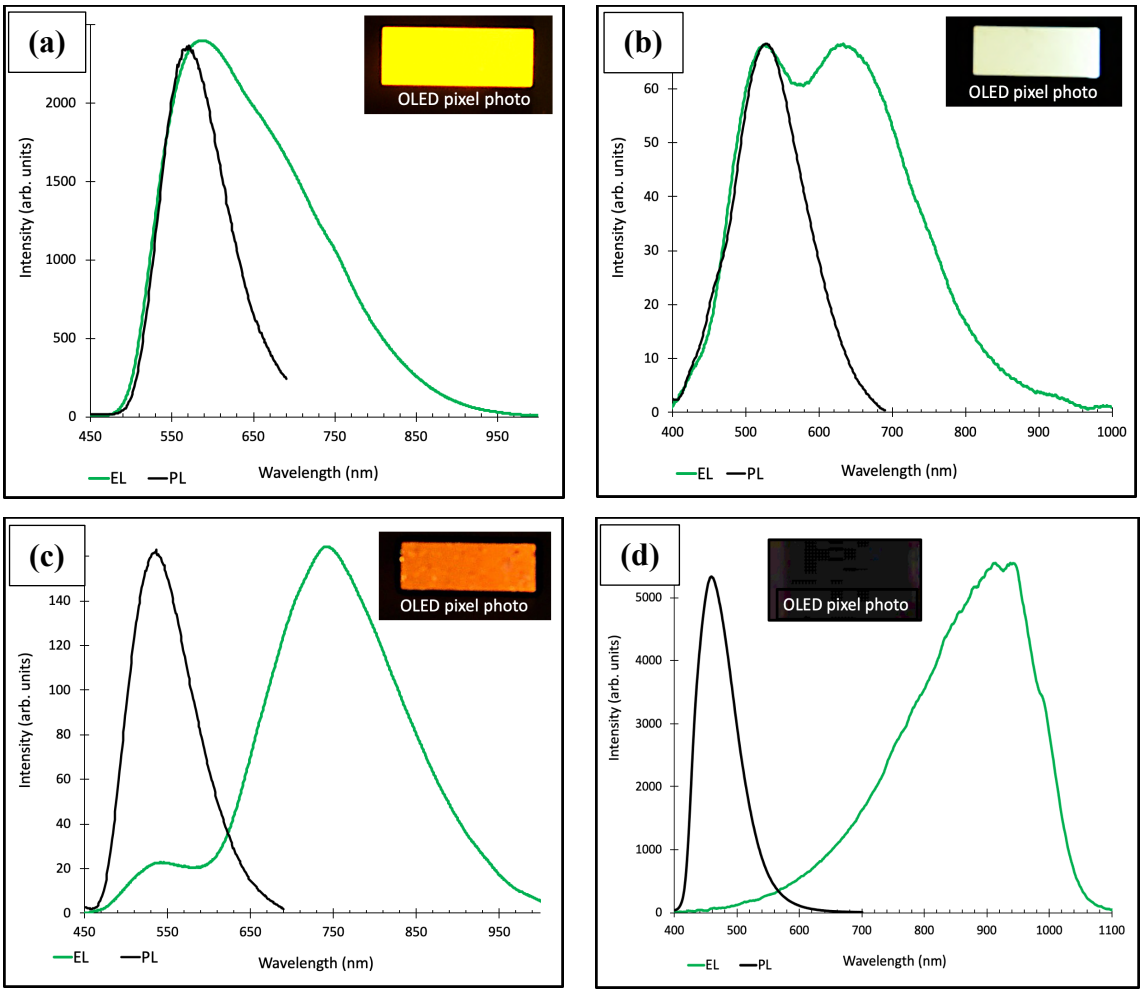

Figure 4.5. Electroluminescence and photoluminescence of Generation 3 OLED devices, along with photos of illuminating pixels. (a) Si(bzimpyMe)2. (b) Si(bzimpyMeOMe)2. (c) Si(bzimpy)2. (d) Si(bzimpyOMe)2

A stepwise measurement of emission at applied voltage of OLED device with $Si(bzimpyMe)_2$ is shown in **Figure 4.6**. The turn on voltage of the lowest energy peak at 675 nm is at 2 V. This peak is significantly lower in energy than photoluminescence of the film in the solid state. This emission is not observed upon mixing NPB and $Si(bzimpyMe)_2$ and photoexciting the mixture, the emission for both materials are observed in the regions that belong to those materials. In the case of applied voltage, the low energy luminescence is observed. This leads to believe that electroluminescence is

observed due to emission from the formed electromer or electroplex upon excitation of NPB and Si(bzimpyMe)$_2$. In fact, there can be multiple electromers or electroplexes, upon application of higher voltage the emission intensity increases and different shoulders of the broad peak gain greater intensity until excitonic emission is observed along with electroplex emission. The much lower turn on voltage for the electroplex based peak can be explained by the nature of this emission being the interfacial interaction between the two films, which has much smaller energy barrier that needs to be overcome than in order to achieve the excitonic based emission.

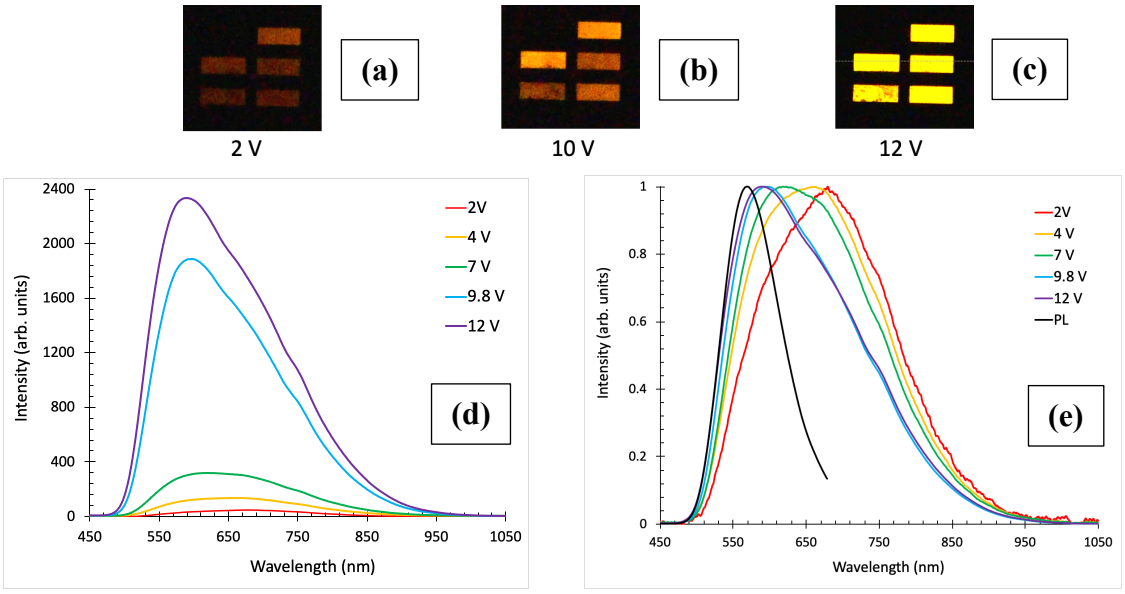

Figure 4.6. Applied voltage vs. emission change of ITO/MoO_3/NPB/Si(bzimpyMe)$_2$/LiF/Al. (a) Photo of electroluminescent at applied bias voltage of 2 V. (b) Photo of electroluminescent at applied bias voltage of 10 V. (c) Photo of electroluminescent at applied bias voltage of 12 V. (d) Intensity is shown as obtained. (e) Normalized intensity to the highest intensity shoulder.

From the band edge diagram shown in **Figure 4.7** some trends can be observed. In the case of the device with Si(bzimpyMe)$_2$ the film was thicker than NPB film, and the HOMO of the Si(bzimpyMe)$_2$ is very close to the HOMO of NPB, and for this device the

excitonic emission was significantly more intense in comparison to the electroplex emission. For device with $Si(bzimpyMeOMe)_2$ the NPB layer was significantly thicker. The difference between the HOMO of NPB and $Si(bzimpyMeOMe)_2$ is greater in this case, and the emission intensity of the excitonic based peak is comparable to the intensity of the electroplex based peak. The band gap of $Si(bzimpyMeOMe)_2$ is also greater than of the $Si(bzimpyMe)_2$, but possibly due to the thickness differences the electroplex emission peak did not shift significantly. The difference in the HOMO energy levels between $Si(bzimpy)_2$ and NPB is even greater than in the previous examples. The thickness for $Si(bzimpy)_2$ was almost three times greater than of NPB, and the intensity of the excitonic peak was significantly smaller in comparison to the electroplex emission. The electroplex emission peak in this device is red shifted by approximately 50 nm. For device with $Si(bzimpyOMe)_2$ the film thickness was significantly thinner than of NPB. The difference in the HOMO energy levels is very similar to $Si(bzimpy)_2$, but the band gap is much greater for $Si(bzimpyOMe)_2$. The excitonic peak emission is not observed, or it is very convoluted, while the electroplex emission peaks is very strong. For this device, the electroplex emission peak is shifted by almost 200 nm in comparison to $Si(bzimpyMe)_2$. Such significant shift towards lower energy could be attributed to the $Si(bzimpyOMe)_2$ layer being much thinner, and possibly the interface with NPB is also different in this case. Due to the nature of electroplex emission being interfacial, it is possible that difference in the film interaction can lead to such energy difference.

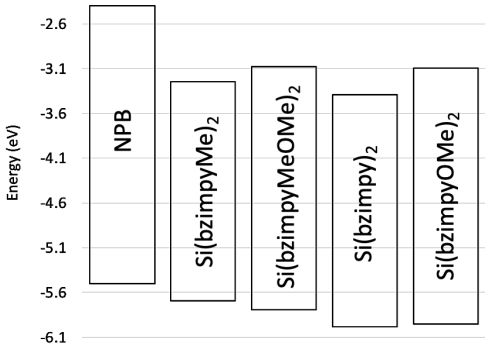

Figure 4.7. Band edge diagram of donor and acceptor materials in Generation 3 OLEDs. The HOMOL and LUMO energy levels of NPB were taken from previously reported values by Trinh Dac *et. al.*[64] Si(pincer)$_2$ band edges were calculate based on cyclic voltammetry experiments and UV-Vis.

4.2. Organic photovoltaic devices

For all of the OPV devices the substrates were prepared as described in the section 3.1.1, then were used to spin coat PEDOT:PSS in ambient conditions. PEDOT:PSS solution was filtered through a 0.45 μm PES filter into a vial, then placed along with prepared ITO glass on a hot plate and heated to 55 °C prior to spin coating. The ITO glass was spun at 2000 rpm in a spin coater for 40 s, and 90 μL of PEDOT:PSS solution was deposited onto the slide. The film was allowed to dry for 3 min at room temperature. A second layer of PEDOT:PSS was added by spin coating 90 μL onto the substrate at 2000 rpm for 40 s, slides were room temperature. The anode portion of the device was then wiped with a cotton swab dipped in water to remove PEDOT:PSS. The films were then annealed at 140 °C for 10 min on a hot plate inside an N_2 filled glove box. It is important to note that the lamp intensity was found to be 150 mW/cm^2, which was then corrected for in the calculation of efficiency. The J-V curves are reported as recorded.

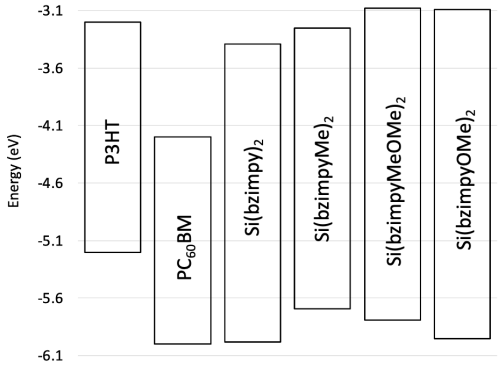

Figure 4.8 Band edge diagram. The energy levels of P3HT and PCBM were obtained from data reported by Khlyabich *et. al*.[65] Si(pincer)$_2$ band edges were calculate based on cyclic voltammetry experiments and UV-Vis.

The control P3HT:$PC_{60}BM$ OPV devices were assembled as shown in **Figure 4.9** along with performance parameters are shown in **Figure 4.10**. In the article reported by Irwin *et. al* in 2007, theoretical Voc was reported to be 1.0 V based on cyclic voltammetry.[66] This sets a goal for the future optimization of these solar cells. For P3HT:$PC_{60}BM$ devices obtained in this experiment three best performing devices had Voc between 0.52-0.54. These results closely compare to reported 0.45-0.55 V for similar devices, important note that the blend used in the article was 10:8 mg (lower performance value) and 20:16 mg (higher performance value) of P3HT:$PC_{60}BM$.[67] Fill factors obtained experimentally were between 34.3-38.4%, while the reported fill factors were 33-44% for blends of 10:8 mg (lower performance value) and 20:16 mg (higher performance value) of P3HT:$PC_{60}BM$.[67] The experimental performance efficiency was calculated to be between 3.3-3.7%, and reported efficiency 0.81-3.96% blends of 10:8 mg (lower performance value) and 20:16 mg (higher performance value) of P3HT:$PC_{60}BM$. These control devices suggest that this is a good method of preparing these solar cells, and we can use these devices as control to compare a set of devices with addition of Si(pincer)$_2$ complexes.

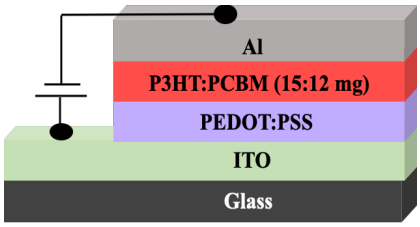

Figure 4.9. OPV device structure for testing P3HT:$PC_{60}BM$ OPVs.

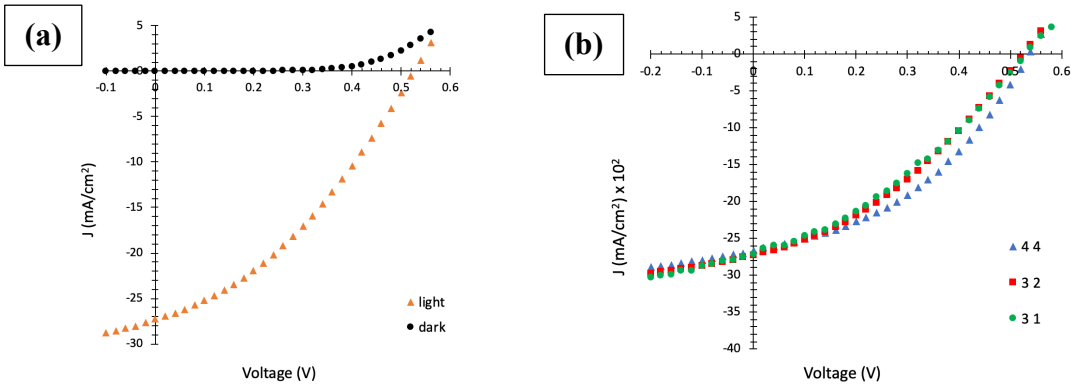

Device	3-1	3-2	4-4	*10:8 mg	*20:16 mg
Voc (V)	0.52	0.53	0.54		
Jsc (mA/cm^2)	-27.1	-26.6	-25.8		
FF%	35.5	34.3	38.4	*33.0	*43.0
η%	3.3	3.3	3.7	*0.81	*3.96

Figure 4.10. J-V curves of standard P3HT:$PC_{60}BM$ devices. (a) dark and light curves of device 3-2 (b) light curves of top three devices. Measured at AM1.5.

The first OPV devices with $Si(pincer)_2$ was assembled as shown in **Figure 4.11**. This device was designed to access the potential of $Si(pincer)_2$ complexes to be used as absorber/acceptor layers in the OPVs. P3HT solution was then prepared inside an N_2 filled glove box by dissolving 20 mg P3HT in 1.00 mL 1,2-dichlorobenzene. The obtained solution was heated to 50 °C on a hot plate for 2 hours before use. The ITO glass was spun at 2000 rpm for 20 s using a spin coater, while 45 µL of P3HT solution was dispensed onto the substrate. The film was then allowed to dry for 30 min at room temperature inside an N_2 filled glove box. Then $Si(bzimpy)_2$ was deposited using vacuum

deposition chamber at 0.25 - 0.30 Å/s until thickness of 45 nm. Last layer was aluminum, which was deposited at the rate of 0.40 Å/s until thickness of 30 nm was reached, then rate was raised to 1.2 Å/s until thickness of 150 nm was reached.

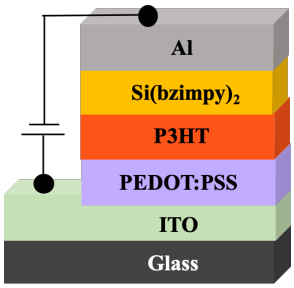

Figure 4.11. OPV device structure for testing $Si(bzimpy)_2$ complex as acceptor/absorber layer in OPVs.

Assembled OPV devices were then tested in the dark and under illumination. J-V curves of three best performing devices are shown in **Figure 4.12** along with performance criteria such as Voc, Jsc, FF and η. Obtained devices had very low Voc for most devices except Device 2-2, and current density was observed in the range of 0.10-0.27 mA/cm^2. The fill factor was found to be 24.2-28.5%. These performance results lead to conclusion that $Si(bzimpy)_2$ is a poor acceptor/absorber for OPVs, but this does not conclude whether or not $Si(bzimpy)_2$ can be used as an electron transport layer in these devices and possibly improve their performance.

The next set of devices were assembled as shown in **Figure 4.13** to probe the hypothesis that thin films of $Si(pincer)_2$ materials can be used to improve device performance based on their electron mobilities, their band edge alignment with P3HT and $PC_{60}BM$, as well as their great thermal stability can save the soft polymer blend from harsh aluminum that is used on top as a cathode. The assembling procedure was the same as for control OPV, except before aluminum layer $Si(pincer)_2$ films were added.

Si(pincer)$_2$ complexes were deposited via thermal evaporation, the rates and thicknesses of which are listed in **Table 4.3**. Then 150 nm layer of aluminum was added on top for all of the devices.

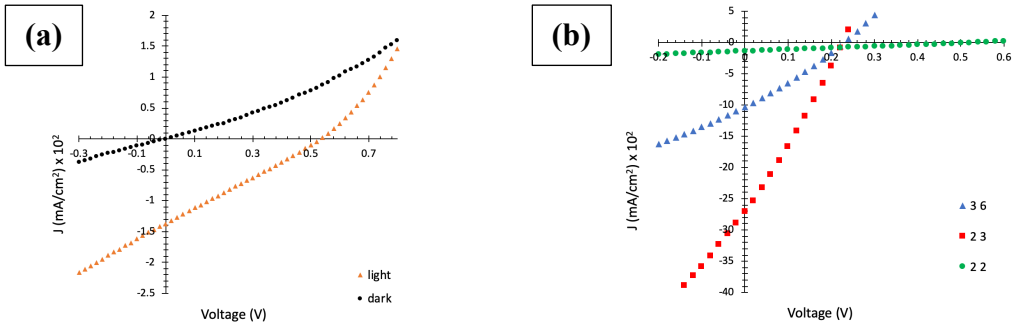

Device	2-2	2-3	3-6
Voc (V)	0.54	0.22	0.23
Jsc (mA/cm^2)	-0.014	-0.27	-0.10
FF%	24.2	27.8	28.5
η%	1.2 x 10^{-3}	1.1 x 10^{-2}	4.5 x 10^{-3}

Figure 4.12. J-V curves of Si(bzimpy)$_2$ devices. (a) dark and light curves of device 2-2 (b) light curves of top three devices. Measured at AM1.5.

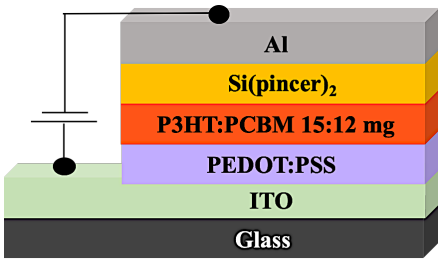

Figure 4.13. OPV device structure with Si(pincer)$_2$ complexes.

Table 4.3. Rate of deposition, and total thickness for Si(pincer)$_2$ complexes in OPV devices.

Material	Rate (Å/s)	Thickness (nm)
Si(bzimpy)$_2$	0.15-0.20	3.5
Si(bzimpyMe)$_2$	0.30-0.40	4.0
Si(bzimpyOMe)$_2$	0.02-0.10	3.0
Si(bzimpyMeOMe)$_2$	0.02-0.15	3.5
Si(IPI)$_2$	0.02-0.15	4.5

Upon addition of Si(bzimpy)$_2$ film, an improvement in Voc is observed from 0.53-0.54 V to 0.58-0.59 V as shown in **Figure 4.14**. There is also significant improvement in the fill factor from 34.3-38.4% to 49.4-54.3%, which is on average a 31% increase from the control. Overall device performance efficiency increased on average by 37% to average of 5.5%.

OPVs with Si(bzimpyMe)$_2$ film, show similar improvement in Voc from 0.53-0.54 V for control to 0.58-0.59 V as shown in **Figure 4.15**. There is also significant improvement in the fill factor from 34.3-38.4% to 50.8-52.3%, which is on average a 30% increase from the control. Overall device performance efficiency increased on average by 43% to average of 6.1% efficiency.

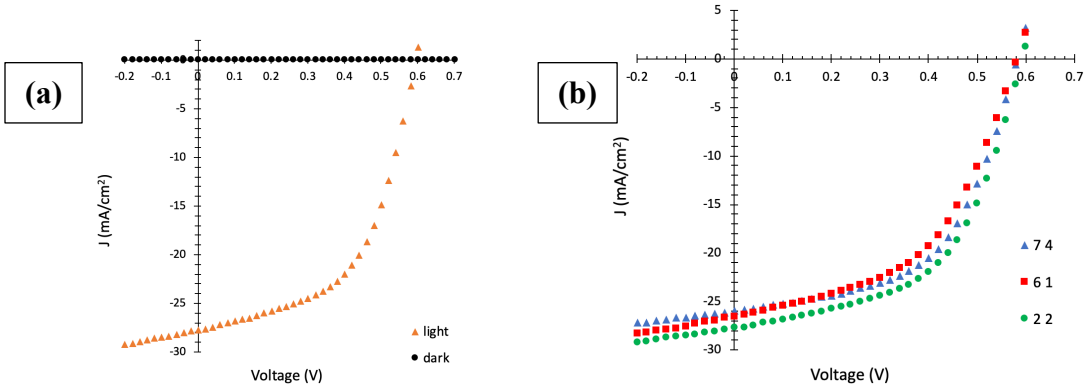

Device	2-2	6-1	7-4
Voc (V)	0.59	0.58	0.58
Jsc (mA/cm^2)	-27.7	-26.6	-25.8
FF%	54.3	49.4	54.0
η%	5.9	5.1	5.4

Figure 4.14. J-V curves of Si(bzimpy)$_2$ devices. (a) dark and light curves of device 2-2 (b) light curves of top three devices. Measured at AM1.5.

For devices with Si(bzimpyOMe)$_2$ film, the Voc improved from 0.53-0.54 V for control to 0.58-0.60 V as shown in **Figure 4.16**. The improvement in the fill factor was not as significant fill factors were 46.3-48.6%, which is on average a 24% increase from

the control. Overall device performance efficiency increased on average by 28% to average of 4.8% efficiency, which is not as significant of improvement as for previously discussed complexes.

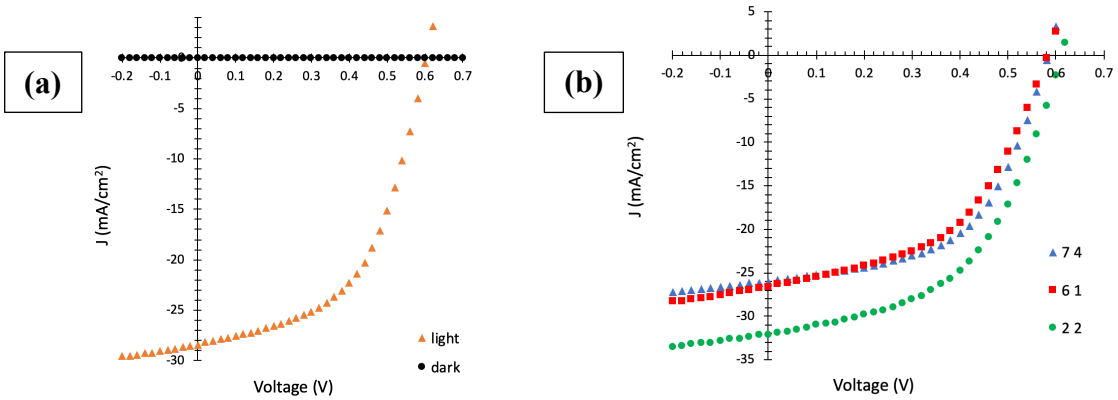

Device	1-1	1-2	2-1
Voc (V)	0.60	0.60	0.61
Jsc (mA/cm^2)	-28.4	-27.8	-32.1
FF%	52.3	51.3	50.8
η%	5.9	5.7	6.6

Figure 4.15. J-V curve of Si(bzimpyMe)$_2$ devices. (a) dark and light curves of device 1-1 (b) light curves of top three devices. Measured at AM1.5.

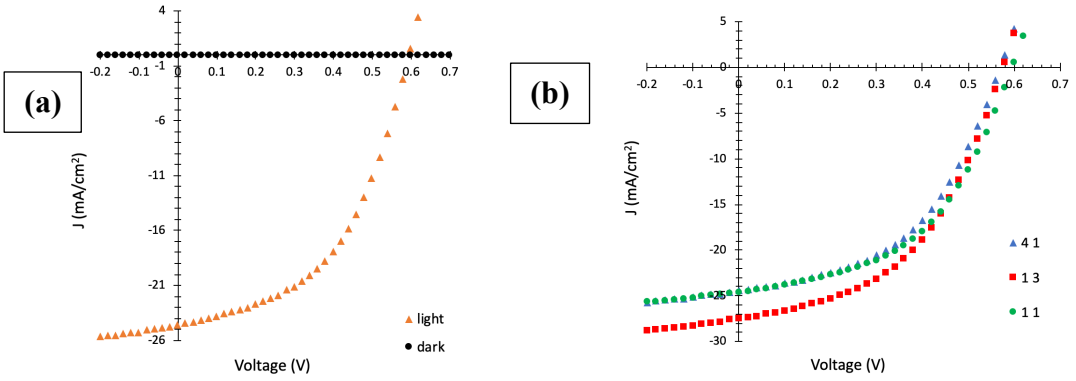

Device	1-1	1-3	4-1
Voc (V)	0.60	0.58	0.59
Jsc (mA/cm^2)	-24.6	-27.4	-24.5
FF%	48.6	47.5	46.3
η%	4.8	5.0	4.5

Figure 4.16. J-V curve of Si(bzimpyOMe)$_2$ devices. (a) dark and light curves of device 1-1 (b) light curves of top three devices. Measured at AM1.5.

Devices with Si(bzimpyMeOMe)$_2$ film have shown the greatest improvement in Voc from 0.53-0.54 V for control to 0.60-0.62 V as shown in **Figure 4.17**. The fill factor was calculated to be 46.3-48.6%, which is on average a 31% increase from the control. Overall device performance efficiency increased on average by 39% to average of 5.6% efficiency.

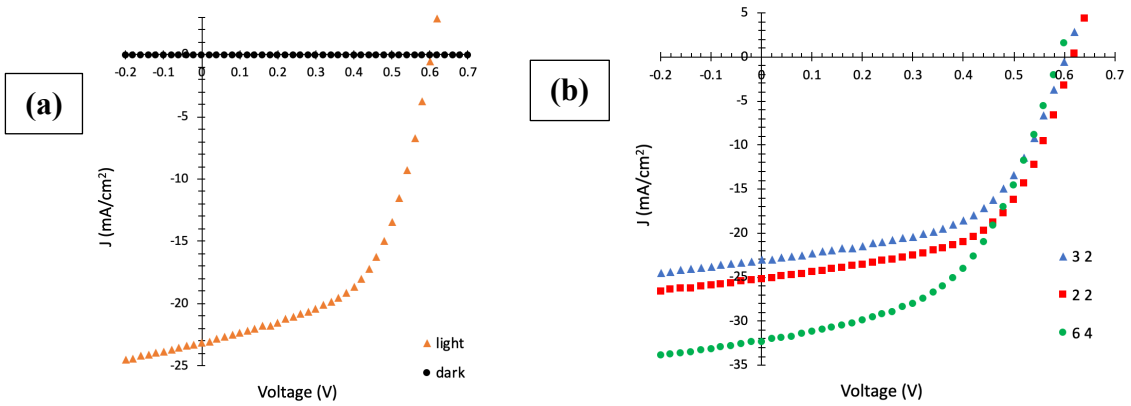

Device	2-2	3-2	6-4
Voc (V)	0.62	0.60	0.60
Jsc (mA/cm^2)	-25.3	-23.0	-32.1
FF%	54.3	54.0	48.2
η%	5.7	5.0	6.2

Figure 4.17. J-V curve of Si(bzimpyMeOMe)$_2$ devices. (a) dark and light curves of device 2-2 (b) light curves of top three devices. Measured at AM1.5.

The last set of prototype OPV devices was with Si(IPI)$_2$ complex, which was shown to have improvement in Voc from 0.53-0.54 V for control to 0.60 V as shown in **Figure 4.18**. The fill factor was calculated to be 41.1-41.7%, which is on average a 13% increase from the control and the lowest improvement in this set of devices. Overall device performance efficiency increased on average by 24% to average of 4.5% efficiency.

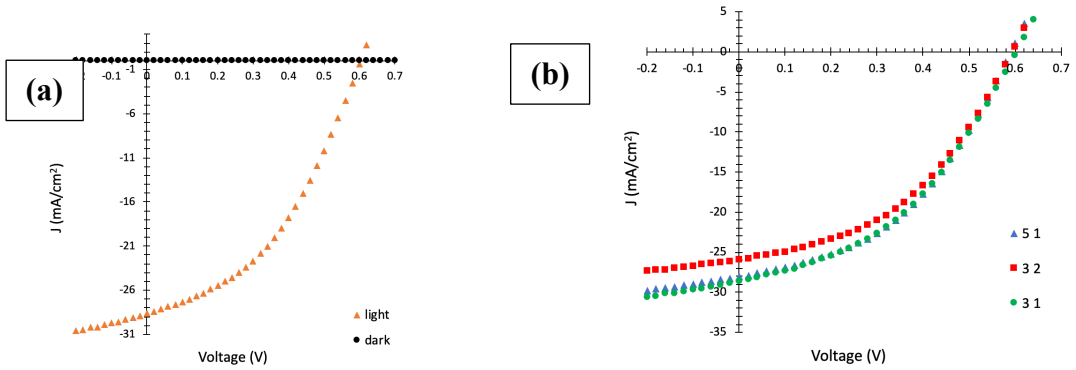

Device	3-1	3-2	5-1
Voc (V)	0.60	0.60	0.60
Jsc (mA/cm^2)	-28.6	-26.0	-28.1
FF%	41.5	41.7	41.1
η%	4.7	4.3	4.6

Figure 4.18. J-V curve of Si(IPI)$_2$ devices. (a) dark and light curves of device 3-1 (b) light curves of top three devices. Measured at AM1.5.

In summary, addition of thin Si(pincer)$_2$ film as a buffer and electron transport layer improved performance of P3HT:PCBM solar cells. This can be due to multiple factors, such as improved thermal stability of Si(pincer)$_2$ films served as protecting layer for aluminum contact deposition, protecting the polymer blend from damage. Addition of separate electron transport layer can serve as assistance for better charge extraction, and prevent some unwanted processes, which result in loss of efficiency. This can be seen in the summary figure with all of the representative curves overlaid in **Figure 4.19**. Summary of the performance criteria of P3HT:PCBM devices that employed Si(pincer)$_2$ complexes as an electron injection/buffer layer are reported in **Table 4.4**. The best overall improvement in device performance was observed using Si(bzimpyMe)$_2$ with an average fill factor of 51.47% and efficiency of 6.09%. This complex has an overall higher thermal stability in comparison to other pincer complexes, the hole mobility of P3HT:PCBM blend has been reported to be in 10^{-5} cm^2 V^{-1} s^{-1},[68, 69] while electron mobility was reported

to be 10^{-4} cm^2 V^{-1} s^{-1}.[68, 69] The electron mobility of $Si(bzimpyMe)_2$ film was determined to be 5 x 10^{-5} ± 2 x 10^{-5} cm^2 V^{-1} s^{-1}, which would fit well for optimal device performance. $Si(bzimpyMe)_2$ makes densely packed films, and would serve as a good hole blocker. The LUMO of $Si(bzimpyMe)_2$ is much higher than of PCBM, which would assist maximization of the Voc. These contributing factors can serve to minimise the loses within the device, and result in improved performance.

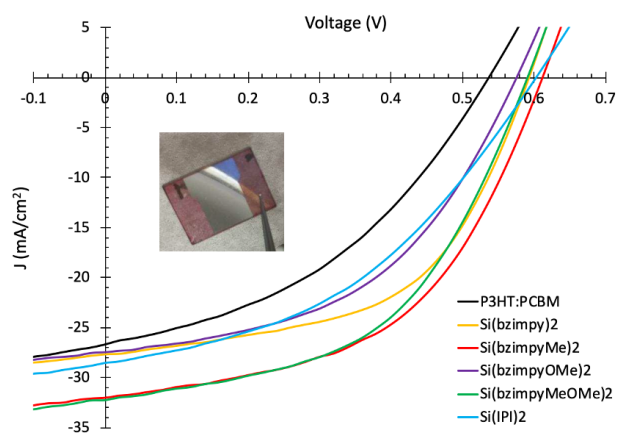

Figure 4.19. J-V curve of $Si(IPI)_2$ devices. (a) dark and light curves of device 3-1 (b) light curves of top three devices. Measured at AM1.5.

Table 4.4. Summary of all P3HT:PCBM devices along with $Si(pincer)_2$ complexes as an electron injection/buffer layer.

Device	**P3HT:PCBM**	**$Si(bzimpy)_2$**	**$Si(bzimpyMe)_2$**
Voc (V)	0.530 ± 0.010	0.583 ± 0.006	0.603 ± 0.006
Jsc (mA/cm^2)	-27.02 ± 0.31	-26.68 ± 0.92	-29.41 ± 2.32
FF%	36.07 ± 2.12	52.56 ± 2.73	51.47 ± 0.74
η%	3.44 ± 0.21	5.46 ± 0.42	6.09 ± 0.48

Device	**$Si(bzimpyOMe)_2$**	**$Si(bzimpyMeOMe)_2$**	**$Si(IPI)_2$**
Voc (V)	0.590 ± 0.010	0.607 ± 0.012	0.597 ± 0.006
Jsc (mA/cm^2)	-25.47 ± 1.66	-26.76 ± 4.72	-27.5 ± 1.39
FF%	47.50 ± 1.14	52.17 ± 3.44	41.4 ± 0.33
η%	4.76 ± 0.29	5.60 ± 0.61	4.56 ± 0.21

CHAPTER 5: CONCLUSIONS AND FUTURE WORK

In this work, total of six hexacoordinate silicon complexes with two dianionic ligands were synthesized, characterized and then studied to understand their place in organic electronic devices. These complexes have shown good stability in solution and solid state, which makes them applicable in variety of devices. Some of the most unique characteristics of these molecules are their thermal stability at temperatures over 200 °C. The $Si(bzimpy)_2$ has demonstrated good moisture stability when placed in moisture containing environment.

These complexes can be thermally evaporated into very dense, smooth films, in some cases the surface roughness was under 1 nm. This is important in order to minimized pinholes and device short-circuiting. These materials have also shown improved photostability, which remains to be one of the issues of use of organic materials in electronics. From the results obtained with XRD and Raman experiments it still remains unknown in which orientation molecules stack inside the film. But it can be concluded that films are largely amorphous as deposited. It is common for films at the nanoscale to undergo changes upon annealing, and these films are no exception. $Si(bzimpy)_2$ was thermally annealed at a range of different temperatures, as well as at the phase change temperature, and it was observed that upon annealing the photoluminescence significantly decreases. This result leads to believe that it was best to use these materials as deposited for better device performance.

From carrier mobility experiments using SCLS method can be concluded that all studied $Si(pincer)_2$ complexes with the exception of $Si(BIP)_2$, which was not investigated due to the challenges in film deposition, are promising electron transport materials.

Materials Si(bzimpyMeOMe)$_2$ and Si(IPI)$_2$ have similar carrier mobilities for both electrons and holes. For the rest of materials the hole mobility was found to be about an order of magnitude slower than the electron mobility. The highest electron mobility was calculated to be $1.17 \times 10^{-4} \pm 2.51 \times 10^{-5}$ cm^2/Vs for Si(bzimpy)$_2$. The highest hole mobility was calculated to be $1.07 \times 10^{-5} \pm 5.99 \times 10^{-6}$ cm^2/Vs for Si(bzimpy)$_2$. These charge transport layers can be used in variety of organic electronic devices such as OLEDs, OPVs, OFETs, and sensors. In this work OLED and OPV devices with Si(pnicer)$_2$ complexes were assembled and tested.

The OLED devices were successfully assembled using Si(bzimpy)$_2$, Si(bzimpyMe)$_2$, Si(bzimpyOMe)$_2$, and Si(bzimpyMeOMe)$_2$. Devices that were assembled with NPB have shown significant improvement in performance lifetime from 1 min to over 10 min, and intensity of emission in comparison to the single layer approach. It was also observed that all of the obtained devices have deep red – NIR emission. Although the assembled devices do not have strong emission in the visible range of the spectrum, there are verity of applications in sensing that can benefit from such OLED devices such as eye tracking, night vision, automotive LiDIR, facial and gesture recognition.

OPV devices that were assembled with Si(bzimpy)$_2$ as an acceptor/absorber layer for P3HT donor were not successful, the best performing device had fill factor of 27.8% and efficiency of 1.1×10^{-2}%. Instead, Si(pincer)$_2$ complexes were used as electron transport/buffer layers in P3HT:$PC_{60}BM$ blended OPVs. A control OPV device with pristine P3HT: $PC_{60}BM$ blended were assembled and tested. The best performing device had a fill factor of 38.4% and efficiency of 3.7%. All of the devices that employed

$Si(pincer)_2$ complexes have shown significant improvement in device performance. The most improvement was observed for device with $Si(bzimpyMe)_2$, which had a fill factor of 52.3% and efficiency of 5.9%.

In the future, further studies of film structure would be needed to obtain a better understanding of some of the properties that are caused possibly due to packing in the film. These experiments include further studies using Raman spectroscopy, XRD, possibly GIWAX. The studies would need to be performed for films as deposited, as well as after annealing at the temperatures of the phase change.

From results obtained after charge mobility experiments, it would be appropriate to test ambipolar host capabilities of the $Si(pincer)_2$ materials. This can be done via assembling an OLED device where $Si(pincer)_2$ will be doped with highly efficient emitter and used as the active emitting component in the device. As the general trend moving towards not only more efficient OLEDs, but also reducing the number of layers in the device, this can be a great solution, since there will be no need for additional ETL and HTL, and possibly may eliminate the need for electron and hole injection layers as well.

The future of OPVs is possible if they can be manufactured on large scale much cheaper than inorganic Si-wafer based solar cells, even if they are not as efficient. Thus, would be important to test solution processing capabilities of $Si(pincer)_2$ materials. Although, these complexes have low solubility, this should note pose issues, since only very thin layer is needed to achieve improvement in device performance. Thus, solution based processing would be the next step in the OPV device development and testing.

REFERENCES

1. Bernanose, A.; Vouaux, P., Électroluminescence organique : étude du mode d'émission. *J. Chim. Phys.* **1953,** *50*, 261-263.

2. Pope, M.; Kallmann, H. P.; Magnante, P., Electroluminescence in Organic Crystals. *The Journal of Chemical Physics* **1963,** *38* (8), 2042-2043.

3. Zou, S.-J.; Shen, Y.; Xie, F.-M.; Chen, J.-D.; Li, Y.-Q.; Tang, J.-X., Recent advances in organic light-emitting diodes: toward smart lighting and displays. *Materials Chemistry Frontiers* **2020,** *4* (3), 788-820.

4. Abdulrazzaq, O. A.; Saini, V.; Bourdo, S.; Dervishi, E.; Biris, A. S., Organic Solar Cells: A Review of Materials, Limitations, and Possibilities for Improvement. *Particulate Science and Technology* **2013,** *31* (5), 427-442.

5. Facchetti, A., Semiconductors for organic transistors. *Materials Today* **2007,** *10* (3), 28-37.

6. Bässler, H.; Köhler, A., Charge transport in organic semiconductors. *Top Curr Chem* **2012,** *312*, 1-65.

7. Hua, W.; Du, X.; Su, W.; Lin, W.; Zhang, D., Full phosphorescent white-light organic light-emitting diodes with improved color stability and efficiency by fine tuning primary emission contributions. *AIP Advances* **2014,** *4* (2), 027103.

8. Godumala, M.; Choi, S.; Cho, M. J.; Choi, D. H., Recent breakthroughs in thermally activated delayed fluorescence organic light emitting diodes containing non-doped emitting layers. *Journal of Materials Chemistry C* **2019,** *7* (8), 2172-2198.

9. Luo, Y.-J.; Lu, Z.-Y.; Huang, Y., Triplet fusion delayed fluorescence materials for OLEDs. *Chinese Chemical Letters* **2016,** *27* (8), 1223-1230.

10. Lim, K.; Li, X.; Tu, Y., Effect of moving pictures on visual task performance and fatigue using 4K OLED and LCD TVs. *Journal of the Society for Information Display* **2020,** *28* (2), 177-183.

11. Han, J.; Suk, H. J., Do users Perceive the same image differently? Comparison of OLED and LCD in mobile HMDs and smartphones. *Journal of Information Display* **2019,** *20* (1), 31-38.

12. Miller, N. J. L., F. A. *OLED Lighting Products:Capabilities, Challenges, Potential*; Prepared for the U.S. Department of Energy under Contract DE-AC05-76RL01830, 2016.

13. Tang, C. W.; VanSlyke, S. A., Organic electroluminescent diodes. *Applied Physics Letters* **1987,** *51* (12), 913-915.

14. Herre, W., Ralph S. Becker: Theory and Interpretation of Fluorescence and Phosphorescence. Interscience Publishers, John Wiley & Sons, London, New York, Sydney 1969. 283 Seiten. Preis: 140 s. *Berichte der Bunsengesellschaft für physikalische Chemie* **1970,** *74* (3), 310-310.

15. Beljonne, D.; Shuai, Z.; Ye, A.; Brédas, J.-L., Charge-recombination processes in oligomer- and polymer-based light-emitting diodes: A molecular picture. *Journal of the Society for Information Display* **2005,** *13* (5), 419-427.

16. Jiang, T.; Liu, Y.; Ren, Z.; Yan, S., The design, synthesis and performance of thermally activated delayed fluorescence macromolecules. *Polymer Chemistry* **2020,** *11* (9), 1555-1571.

17. Chen, X.-K.; Kim, D.; Brédas, J.-L., Thermally Activated Delayed Fluorescence (TADF) Path toward Efficient Electroluminescence in Purely Organic Materials: Molecular Level Insight. *Accounts of Chemical Research* **2018,** *51* (9), 2215-2224.

18. Thompson, M. E.; Burrows, P. E.; Forrest, S. R., Electrophosphorescence in organic light emitting diodes. *Curr. opin. solid state mater. sci* **1999,** *4* (4), 369-372.

19. Murawski, C.; Leo, K.; Gather, M. C., Efficiency Roll-Off in Organic Light-Emitting Diodes. *Advanced Materials* **2013,** *25* (47), 6801-6827.

20. Mao, H.-T.; Li, G.-F.; Shan, G.-G.; Wang, X.-L.; Su, Z.-M., Recent progress in phosphorescent Ir(III) complexes for nondoped organic light-emitting diodes. *Coordination Chemistry Reviews* **2020,** *413*, 213283.

21. Salehi, A.; Dong, C.; Shin, D.-H.; Zhu, L.; Papa, C.; Thy Bui, A.; Castellano, F. N.; So, F., Realization of high-efficiency fluorescent organic light-emitting diodes with low driving voltage. *Nature communications* **2019,** *10* (1), 2305-2305.

22. Xiao, P.; Huang, J.; Yu, Y.; Liu, B., Recent Developments in Tandem White Organic Light-Emitting Diodes. *Molecules (Basel, Switzerland)* **2019,** *24* (1), 151.

23. Mertens, R., The OLED Handbook. A Guide to OLED Technology, Industy & Market. OLED-Info: 2019; p. 145.

24. Jou, J.-H.; Kumar, S.; Agrawal, A.; Li, T.-H.; Sahoo, S., Approaches for fabricating high efficiency organic light emitting diodes. *Journal of Materials Chemistry C* **2015,** *3* (13), 2974-3002.

25. Cui, Y.; Yao, H.; Zhang, J.; Zhang, T.; Wang, Y.; Hong, L.; Xian, K.; Xu, B.; Zhang, S.; Peng, J.; Wei, Z.; Gao, F.; Hou, J., Over 16% efficiency organic

photovoltaic cells enabled by a chlorinated acceptor with increased open-circuit voltages. *Nature Communications* **2019,** *10* (1), 2515.

26. Meng, L.; Zhang, Y.; Wan, X.; Li, C.; Zhang, X.; Wang, Y.; Ke, X.; Xiao, Z.; Ding, L.; Xia, R.; Yip, H.-L.; Cao, Y.; Chen, Y., Organic and solution-processed tandem solar cells with 17.3% efficiency. *Science* **2018,** *361* (6407), 1094-1098.

27. Tang, C. W., Two-layer organic photovoltaic cell. *Appl. Phys. Lett.* **1986,** *48*, 183-185.

28. Yu, G.; Gao, J.; Hummelen, J. C.; Wudl, F.; Heeger, A. J., Polymer Photovoltaic Cells: Enhanced Efficiencies via a Network of Internal Donor-Acceptor Heterojunctions. *Science* **1995,** *270* (5243), 1789-1791.

29. Laboratory, N. R. E. Best Research-Cell Efficiency Chart. https://www.nrel.gov/pv/cell-efficiency.html (accessed July 20).

30. Peumans, P. Y., A.; Forrest, S. R., Small molecular weight organic thin-film photodetectors and solar cells. *J. Appl. Phys.* **2003,** *93*, 3693-3723.

31. Mikhnenko, O. V.; Blom, P. W. M.; Nguyen, T.-Q., Exciton diffusion in organic semiconductors. *Energy & Environmental Science* **2015,** *8* (7), 1867-1888.

32. Nikolka, M.; Hurhangee, M.; Sadhanala, A.; Chen, H.; McCulloch, I.; Sirringhaus, H., Correlation of Disorder and Charge Transport in a Range of Indacenodithiophene-Based Semiconducting Polymers. *Advanced Electronic Materials* **2018,** *4* (10), 1700410.

33. Pittelli, S. L.; De Keersmaecker, M.; Ponder Jr, J. F.; Österholm, A. M.; Ochieng, M. A.; Reynolds, J. R., Structural effects on the charge transport properties of

chemically and electrochemically doped dioxythiophene polymers. *Journal of Materials Chemistry C* **2020,** *8* (2), 683-693.

34. Suzuki, F.; Kubo, S.; Fukushima, T.; Kaji, H., Effects of Structural and Energetic Disorders on Charge Transports in Crystal and Amorphous Organic Layers. *Scientific Reports* **2018,** *8* (1), 5203.

35. Lin, Y.; Li, Y.; Zhan, X., Small molecule semiconductors for high-efficiency organic photovoltaics. *Chemical Society Reviews* **2012,** *41* (11), 4245-4272.

36. Yao, Y. J.; Gao, J.; Bao, F.; Jiang, S. F.; Zhang, X.; Ma, R., Covalent functionalization of graphene with polythiophene through a Suzuki coupling reaction. *Rsc Advances* **2015,** *5* (53), 42754-42761.

37. Sasabe, H.; Kido, J., Low Molecular Weight Materials: Electron-Transport Materials. In *Handbook of Organic Light-Emitting Diodes*, Adachi, C.; Hattori, R.; Kaji, H.; Tsujimura, T., Eds. Springer Japan: Tokyo, 2019; pp 1-10.

38. Shahnawaz; Sudheendran Swayamprabha, S.; Nagar, M. R.; Yadav, R. A. K.; Gull, S.; Dubey, D. K.; Jou, J.-H., Hole-transporting materials for organic light-emitting diodes: an overview. *Journal of Materials Chemistry C* **2019,** *7* (24), 7144-7158.

39. Dey, A.; Layek, A.; Roychowdhury, A.; Das, M.; Datta, J.; Middya, S.; Das, D.; Ray, P. P., Investigation of charge transport properties in less defective nanostructured ZnO based Schottky diode. *RSC Advances* **2015,** *5* (46), 36560-36567.

40. Röhr, J. A.; Moia, D.; Haque, S. A.; Kirchartz, T.; Nelson, J., Exploring the validity and limitations of the Mott–Gurney law for charge-carrier mobility determination of semiconducting thin-films. *Journal of Physics: Condensed Matter* **2018,** *30* (10), 105901.

41. Xiao, P. H., J.; Yu, Y.; Yuan, J.; Luo, D.; Liu, B.; Liang, D., Recent Advances of Exciplex-Based White Organic Light-Emitting Diodes. . *Appl. Sci.* **2018,** *8*, 1449.

42. Beattie, I. R., The acceptor properties of quadripositive silicon, germanium, tin, and lead. *Quarterly Reviews, Chemical Society* **1963,** *17* (4), 382-405.

43. Miller, J. D.; Baron, E. D.; Scull, H.; Hsia, A.; Berlin, J. C.; McCormick, T.; Colussi, V.; Kenney, M. E.; Cooper, K. D.; Oleinick, N. L., Photodynamic therapy with the phthalocyanine photosensitizer Pc 4: The case experience with preclinical mechanistic and early clinical–translational studies. *Toxicology and Applied Pharmacology* **2007,** *224* (3), 290-299.

44. Lim, B.; Margulis, G. Y.; Yum, J.-H.; Unger, E. L.; Hardin, B. E.; Grätzel, M.; McGehee, M. D.; Sellinger, A., Silicon-Naphthalo/Phthalocyanine-Hybrid Sensitizer for Efficient Red Response in Dye-Sensitized Solar Cells. *Organic Letters* **2013,** *15* (4), 784-787.

45. Peloquin, D. M.; Schmedake, T. A., Recent advances in hexacoordinate silicon with pyridine-containing ligands: Chemistry and emerging applications. *Coordination Chemistry Reviews* **2016,** *323*, 107-119.

46. Kawamoto, K.; Akashi, H.; Yamasaki, M.; Shibahara, T., Fluorescent Fluoro–Silicon(IV) Complexes with Schiff Base Ligands. *Chemistry Letters* **2013,** *42* (4), 389-391.

47. Xiang, Y.; Fu, C.; Breiding, T.; Sasmal, P. K.; Liu, H.; Shen, Q.; Harms, K.; Zhang, L.; Meggers, E., Hydrolytically stable octahedral silicon complexes as bioactive scaffolds: application to the design of DNA intercalators. *Chemical Communications* **2012,** *48* (57), 7131-7133.

48. Breiding, T.; Henker, J.; Fu, C.; Xiang, Y.; Glöckner, S.; Hofmann, P.; Harms, K.; Meggers, E., Synthesis and Functionalization of Hexacoordinate (Arenediolato)bis(polypyridyl)silicon(IV) Complexes. *European Journal of Inorganic Chemistry* **2014,** *2014* (18), 2924-2933.

49. Fu, C.; Harms, K.; Zhang, L.; Meggers, E., DNA Mismatch Recognition by a Hexacoordinate Silicon Sandwich–Ruthenium Hybrid Complex. *Organometallics* **2014,** *33* (12), 3219-3222.

50. Portius, P.; Filippou, A. C.; Schnakenburg, G.; Davis, M.; Wehrstedt, K.-D., Neutral Lewis Base Adducts of Silicon Tetraazide. *Angewandte Chemie International Edition* **2010,** *49* (43), 8013-8016.

51. Peloquin, D. M.; Dewitt, D. R.; Patel, S. S.; Merkert, J. W.; Donovan-Merkert, B. T.; Schmedake, T. A., Spectroelectrochemistry of tris(bipyridyl)silicon(iv): ligand localized reductions with potential electrochromic applications. *Dalton Transactions* **2015,** *44* (43), 18723-18726.

52. Suthar, B.; Aldongarov, A.; Irgibaeva, I. S.; Moazzen, M.; Donovan-Merkert, B. T.; Merkert, J. W.; Schmedake, T. A., Electrochemical and spectral properties of hexacoordinate polypyridyl silicon complexes. *Polyhedron* **2012,** *31* (1), 754-758.

53. Lee, D. A.; Moon, S. K.; Sizeland, A. N.; Gould, N. W.; Gbarbea, E. M.; Owusu, D.; Jones, D. S.; Schmedake, T. A., Synthesis and characterization of a dipyridocatecholate silicon complex. *Inorganic Chemistry Communications* **2013,** *33*, 125-128.

54. England, J.; Wieghardt, K., 2,2′-Bipyridine Compounds of Group 14 Elements: A Density Functional Theory Study. *Inorg Chem* **2013,** *52* (17), 10067-10079.

55. Wang, Y.; Liu, D.; Ikeda, S.; Kumashiro, R.; Nouch, R.; Xu, Y.; Shang, H.; Ma, Y.; Tanigaki, K., Ambipolar behavior of 2,5-diphenyl-1,4-distyrylbenzene based field effect transistors: An experimental and theoretical study. *Applied Physics Letters* **2010,** *97* (3), 033305.

56. Park, H.; Shin, D.-S.; Yu, H.-S.; Chae, H.-B., Electron mobility in tris(8-hydroxyquinoline)aluminum (Alq3) films by transient electroluminescence from single layer organic light emitting diodes. *Applied Physics Letters* **2007,** *90* (20), 202103.

57. Fong, H. H.; So, S. K., Hole transporting properties of tris(8-hydroxyquinoline) aluminum (Alq3). *Journal of Applied Physics* **2006,** *100* (9), 094502.

58. Khan, M. A.; Xu, W.; Khizar-ul-Haq; Bai, Y.; Jiang, X. Y.; Zhang, Z. L.; Zhu, W. Q.; Zhang, Z. L.; Zhu, W. Q., Electron mobility of 4,7-diphyenyl-1,10-phenanthroline estimated by using space-charge-limited currents. *Journal of Applied Physics* **2008,** *103* (1), 014509.

59. Liu, S.-W.; Wang, J.-K., *Charge mobility of mixed organic semiconductors: a NPB-AlQ₃ study*. SPIE: 2006; Vol. 6333.

60. Rohloff, R.; Kotadiya, N. B.; Crăciun, N. I.; Blom, P. W. M.; Wetzelaer, G. A. H., Electron and hole transport in the organic small molecule α-NPD. *Applied Physics Letters* **2017,** *110* (7), 073301.

61. Chu, T.-Y.; Song, O.-K., Hole mobility of N,N′-bis(naphthalen-1-yl)-N,N′-bis(phenyl) benzidine investigated by using space-charge-limited currents. *Applied Physics Letters* **2007,** *90* (20), 203512.

62. Kalinowski, J. In *Excimers and exciplexes in organic electroluminescence*, 2009.

63. Zhao, Z. X., B.; Yang, Z.; Wang, H.; Wang,X.; Lu,P.; Tian, W., White Light from Excimer and Electromer in Single-Emitting-Component Electroluminescent Diodes. *J. Phys. Chem. C* **2008,** *112* (23), 8511-8515.

64. Hoanh, T. D.; Im, Y. H.; Kim, D.-E.; Kwon, Y.-S.; Lee, B.-J., Synthesis and Electroluminescent Properties of Bis(3H-1,2,3-triazolo-[4,5-b]pyridine-3-ol)zinc Zn(TAP)₂. *Journal of Nanomaterials* **2012,** *2012*, 451306.

65. Khlyabich, P. P.; Burkhart, B.; Rudenko, A. E.; Thompson, B. C., Optimization and simplification of polymer–fullerene solar cells through polymer and active layer design. *Polymer* **2013,** *54* (20), 5267-5298.

66. Irwin, M. D.; Buchholz, D. B.; Hains, A. W.; Chang, R. P. H.; Marks, T. J., p-Type semiconducting nickel oxide as an efficiency-enhancing anode interfacial layer in polymer bulk-heterojunction solar cells. *Proceedings of the National Academy of Sciences* **2008,** *105* (8), 2783-2787.

67. Radbeh, R.; Parbaile, E.; Bouclé, J.; Di Bin, C.; Moliton, A.; Coudert, V.; Rossignol, F.; Ratier, B., Nanoscale control of the network morphology of high efficiency polymer fullerene solar cells by the use of high material concentration in the liquid phase. *Nanotechnology* **2010,** *21* (3), 035201.

68. Koster, L. J. A.; Mihailetchi, V. D.; Xie, H.; Blom, P. W. M., Origin of the light intensity dependence of the short-circuit current of polymer/fullerene solar cells. *Applied Physics Letters* **2005,** *87* (20), 203502.

69. Lee, C.-T.; Lee, C.-H., Conversion efficiency improvement mechanisms of polymer solar cells by balance electron–hole mobility using blended P3HT:PCBM:pentacene active layer. *Organic Electronics* **2013,** *14* (8), 2046-2050.

APPENDIX – A: Synthesis of $Si(bzimpy)_2$

Under a nitrogen atmosphere, bis(benzimidazole)pyridine (2.036 g, 65.07 mmol) in chloroform (60 mL) was stirred at 0 °C, and triethylamine was added to a stirring suspension (1.81 mL, 12.98 mmol). Upon addition of silicon tetrachloride (0.37 mL, 32.23 mmol) the mixture instantly turned yellow and was allowed to stir for 3 min at 0 °C. The resulting brownish-yellow suspension was warmed to room temperature, and the reaction allowed to proceed for 16 h with no stirring. The yellow solid obtained was separated by filtration, washed with chloroform (2 x 15 mL), and dried *in vacuo* for 1 h at 120 °C. The product was then suspended in acetone (60 mL), stirred for 1 h, and filtered to yield a bright yellow powder (1.170 g, 56%). The powder was purified using Soxhlet extraction (0.100 g of product and chloroform (350 mL) were used to extract the product). The yellow luminescent solution was concentrated to dryness to obtain 0.068 g of product. (38% yield overall from $SiCl_4$). ^{1}H NMR(CD_2Cl_2, 500 MHz): δ 5.75 [d, J_{H-H} = 8.4, 4 H], 6.98 [dd, 4 H], 7.05 [dd, , 4 H], 7.58 [d, J_{H-H} = 8.1, 4 H], 8.81 [m, 4 H], 8.97 [t, J_{H-H} = 7.4, 2 H]. ^{13}C NMR($CDCl_2/CD_3OD$, 40/60 mixture, 125 MHz): δ 110.6 (4 C), 119.9 (4 C), 120.6 (4 C), 123.5 (4 C), 125.7 (4 C), 134.9 (4 C), 145.7 (4 C), 147.3 (4 C), 147.4 (4 C), 150.4 (s, 2 C). ^{29}Si NMR($CDCl_3/CD_3OD$, Cr(acac)3 added, 40/60 mixture, 99 MHz): δ -185.7. IR data: 3400 (w), 3058 (w), 1629 (m), 1574 (m), 1558 (m), 1537 (w), 1473 (vs), 1438 (w), 1412 (w), 1376 (w), 1352 (m), 1322 (s), 1294 (w), 1263 (w), 1238 (w), 1194 (w), 1175 (w), 1146 (m), 1122 (w), 1089 (w), 1043 (m), 1007 (w), 963 (w), 926 (m), 835 (w), 816 (w), 807 (w), 738 (vs), 718 (m), 697 (w). Anal. Calc. for $C_{38}H_{22}N_{10}Si{\cdot}H_2O$: C, 68.7; H, 3.6; N, 21.1. Found: C, 68.8; H, 3.9; N, 20.9%. MS (MALDI-TOF): m/z = 647.8

APPENDIX – B: Synthesis of $Si(bzimpyMe)_2$

Under a nitrogen atmosphere, bzimpyMe ligand (1.000g, 2.74 mmol) in chloroform (60 mL) was stirred at 0 °C, and triethylamine was added to a stirring suspension (0.76 mL, 5.45 mmol). Upon addition of silicon tetrachloride (0.16 mL, 1.39 mmol) the mixture instantly turned orange and was allowed to stir for 5 min at 0 °C. The resulting brownish-orange suspension was warmed to room temperature, and the reaction allowed to proceed for 18 h with stirring. The orange solid obtained was separated by removing the solvent via vacuum. The product was then dissolved in dichloromethane (100 mL), and washed with DI water (3 x 50 mL), then obtained solution was brought to dryness. Orange powder was then dissolved in 50:50% acetonitrile:dichloromethane mixture of total volume 50 mL, and was purified via silica gel column (mobile phase 50:50% acetonitrile:dichloromethane mixture). Obtained solution was dried to yield a bright orange powder, and dried *in vacuo* for 12 h at 110 °C (0.454 g, 42.9%). ^{1}H NMR(CD_2Cl_2, 500 MHz): δ 2.03 [s, 12 H], 2.13 [s, 12 H], 5.55 [s, 4 H], 7.28 [s, 4 H], 8.60 [d, J_{H-H} = 7.9, 4 H], 8.84 [t, J_{H-H} = 7.9, 2 H]. ^{13}C NMR(CD_2Cl_2, 125 MHz): δ 20.2 (4 C), 21.3 (4 C), 111.7 (8 C), 119.1 (4 C), 120.9 (4 C), 133.0 (4 C), 134.7 (4 C), 135.4 (4 C), 147.1 (4 C), 147.7 (4 C), 148.3 (2 C) ^{29}Si NMR(CD_2Cl_2, Cr(acac)3 added, 99 MHz): δ -185.9. MS (MALDI-TOF): m/z = 758.5

APPENDIX – C: Synthesis of $Si(bzimpyOMe)_2$

Under a nitrogen atmosphere, bzimpyOMe ligand (1.380 g, 4.07 mmol) in chloroform (50 mL) was stirred at 0 °C, and triethylamine was added to a stirring suspension (1.13 mL, 8.10 mmol). Upon addition of silicon tetrachloride (0.23 mL, 2.00 mmol) the mixture instantly turned pale yellow color and was allowed to stir for 10 min at 0 °C. The resulting greenish-yellow suspension was warmed to room temperature, and the reaction allowed to proceed for 20 h with stirring. The light yellow solid obtained was separated by removing the solvent via vacuum. The product was then dissolved in dichloromethane (150 mL), and washed with DI water (3 x 50 mL), then obtained solution was brought to dryness. Light yellow powder was then dissolved in 50:50% methanol:dichloromethane mixture of total volume 90 mL, and was purified via silica gel column (mobile phase 50:50% methanol:dichloromethane mixture). Obtained solution was dried to yield a bright light yellowish green solid, and dried *in vacuo* for 12 h at 110 °C (0.424 g, 30.0%). ^{1}H NMR($CDCl_3$, 500 MHz): δ 4.44 [s, 6 H], 5.89 [d, J_{H-H} = 9.5, 4 H], 6.93 [m, 4 H], 7.01 [m, 4 H], 7.56 [d, J_{H-H} = 8.0, 4 H], 8.07 s, 2 H]. ^{13}C NMR($CDCl_2/CD_3OD$, 40/60 mixture, 125 MHz): δ 59.3 (2 C), 106.3 (4 C), 121.1 (4 C), 121.2 (4 C), 124.0 (4 C), 126.1 (4 C), 136.0 (4 C), 148.0 (4 C), 148.2 (4 C), 148.7 (4 C), 176.5 (s, 2 C). ^{29}Si NMR($CDCl_3/CD_3OD$, Cr(acac)3 added, 40/60 mixture, 99 MHz): δ -187.4. MS (MALDI-TOF): m/z = 706.9

APPENDIX – D: Synthesis of $Si(bzimpyMeOMe)_2$

Under a nitrogen atmosphere, bzimpyMeOMe ligand (1.000g, 2.52 mmol) in chloroform (60 mL) was stirred at RT, and triethylamine was added to a stirring suspension (0.70 mL, 5.02 mmol). Upon addition of silicon tetrachloride (0.14 mL, 1.22 mmol) the mixture instantly turned yellow and the reaction allowed to proceed for 20 h with stirring. The yellow solid obtained was separated by removing the solvent via vacuum, The product was then dissolved in dichloromethane (120 mL), and washed with DI water (3 x 50 mL), then obtained solution was brought to dryness. Orange powder was then dissolved in 50:50% acetonitrile:dichloromethane mixture of total volume 100 mL, and was purified via silica gel column (mobile phase 50:50% acetonitrile:dichloromethane mixture). Obtained solution was dried to yield a bright yellow powder, and dried *in vacuo* for 14 h at 110 °C (0.497 g, 49.8%). ^{1}H NMR($(CD_3)_2SO$, 300 MHz): δ 2.04 [s, 4 H], 2.10 [s, 4 H], 4.56 [s , 4 H], 5.63 [s, 4 H], 7.29 [s, 4 H], 8.34 [s, 2 H]. ^{13}C NMR($(CD_3)_2SO$, 125 MHz): δ 54.9 (4 C) 59.3 (4 C), 105.1 (2 C), 111.0 (4 C), 120.2 (4 C), 131.7 (4 C), 133.6 (4 C), 133.9 (4 C), 146.4 (4 C), 147.0 (4 C), 147.4 (s, 2 C). ^{29}Si NMR($(CD_3)_2SO$, Cr(acac)3 added, 99 MHz): δ -188.5. MS (MALDI-TOF): m/z = 817.7

APPENDIX – E: Synthesis of $Si(BIP)_2$

Under a nitrogen atmosphere, BIP ligand (0.8660 g, 2.80 mmol) in THF (100 mL) was stirred at -78°C, and 2.5 M n-butyllithium was added to a stirring suspension (2.24 mL, 5.60 mmol) and allowed to stir for 30 min. Upon addition of silicon tetrachloride (0.20 mL, 1.74 mmol) the mixture instantly turned yellow after which the reaction flask was brought to room temperature and the reaction was allowed to proceed for 18 h. The solvent was then evaporated under vacuum and the resulting crude solid was purified via soxhlet extraction in chloroform for 24 hours, then acetone for 48 hours. The pure brown solid was then allowed to dry under vacuum for 24 hours (0.050g, 4.81%). ^{1}H NMR(DMSO-d_6, 500 MHz): δ 5.70 (m, 4H), 6.74 (m, 4H), 7.29 (d, J = 6.55, 4H), 7.34 (m, 4H), 7.71 (s, 4H), 8.44 (d, J = 7.95, 4H), 8.84 (t, J = 7.90, 2H). ^{13}C NMR($(CD_3)_2SO$, 125 MHz): δ 102.79 (4 C), 111.13 (4 C), 116.84 (4 C), 119.19 (4 C), 122.26 (4 C), 123.97 (4 C), 131.85 (4 C), 133.42 (4 C), 138.45 (4 C), 147.44 (4 C), 147.84 (2 C). ^{29}Si NMR ($(CD_3)_2SO$, Cr(acac)3 added, 99 MHz): δ -179.4. MS (MALDI-TOF): m/z = 643.0

APPENDIX – F: Synthesis of $Si(IPI)_2$

Under a nitrogen atmosphere, IPI ligand (1.000g, 4.74 mmol) in chloroform (50 mL) was stirred at RT, and triethylamine was added to a stirring suspension (1.32 mL, 9.48 mmol). Upon addition of silicon tetrachloride (0.27 mL, 2.37 mmol) the mixture instantly turned yellow-green and the reaction allowed to proceed for 22 h with stirring. The yellow solid obtained was separated by removing the solvent via vacuum. The product was then dissolved in dichloromethane (150 mL), and washed with DI water (3 x 50 mL), then obtained solution was dried to yield a bright yellow powder, and dried *in vacuo* for 24 h at 100 °C (0.805 g, 55.2%). ^{1}H NMR($(CD_3)_2SO$, 500 MHz): δ 6.48 [s, 4 H], 6.97 [s, 4 H], 8.11 [(d, J = 8.00, 4 H], 8.67 [t, J = 7.75, 2 H]. ^{13}C NMR($(CD_3)_2SO$, 125 MHz): δ 116.5 (4 C) 121.8 (4 C), 135.4 (4 C), 143.9 (4 C), 144.8 (4 C), 148.9 (2 C). MS (MALDI-TOF): m/z = 646.1

APPENDIX – G: ^{1}H NMR spectrum of Si(bzimpyMe)$_2$. (500 Mhz, CD_2Cl_2)

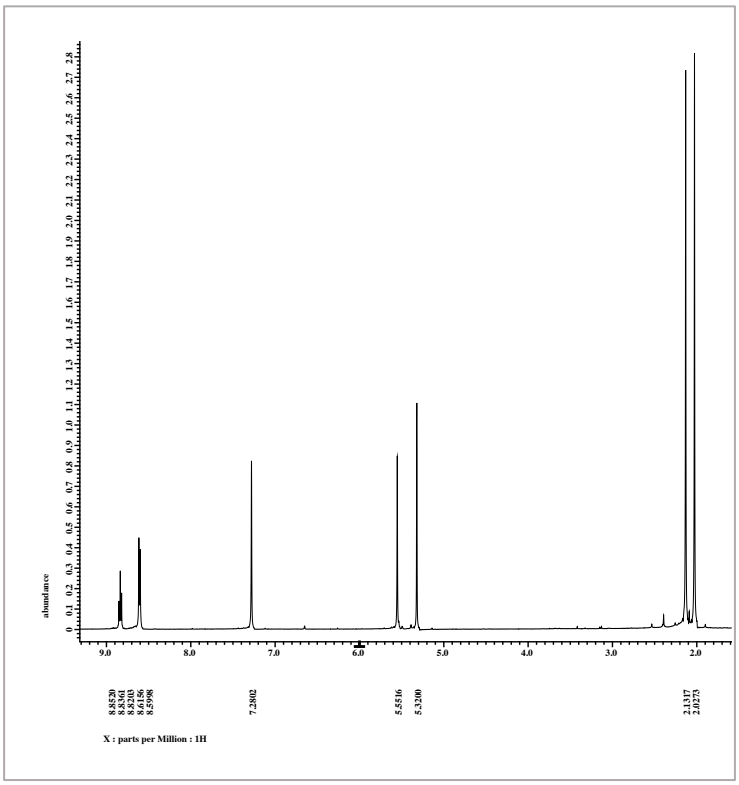

APPENDIX – H: ^{1}H NMR spectrum of Si(bzimpyOMe)$_2$. (500 Mhz, $CDCl_3$)

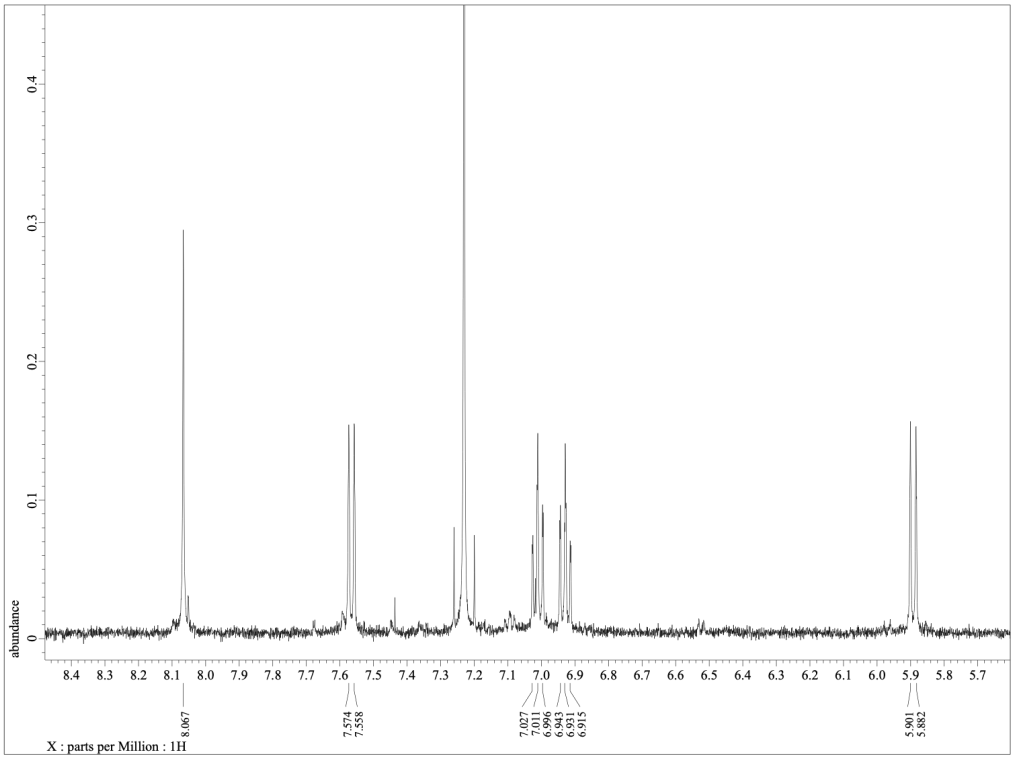

APPENDIX – I: ^{1}H NMR spectrum of Si(bzimpyMeOMe)$_2$. (300 Mhz, (CD$_3$)$_2$SO)

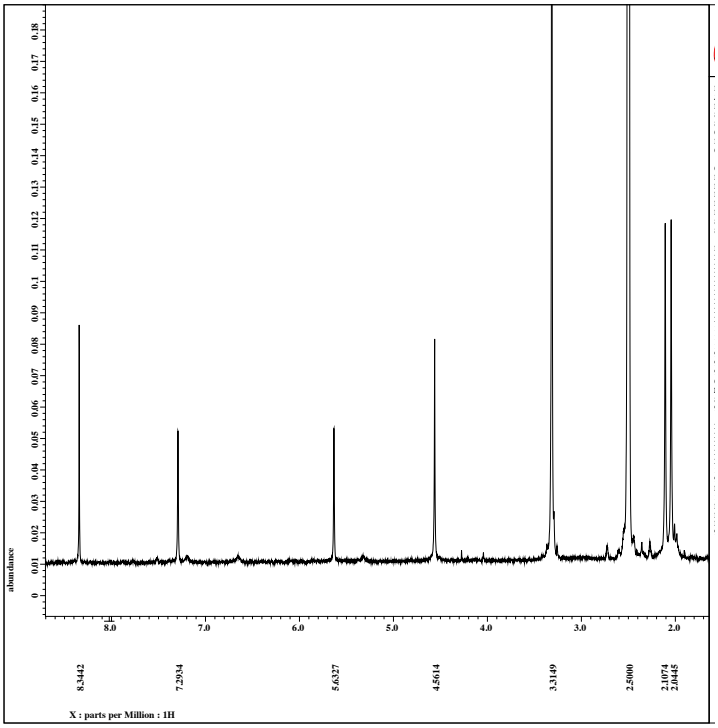

APPENDIX – J: ^{1}H NMR spectrum of Si(BIP)$_2$. (500 Mhz, (CD$_3$)$_2$SO)

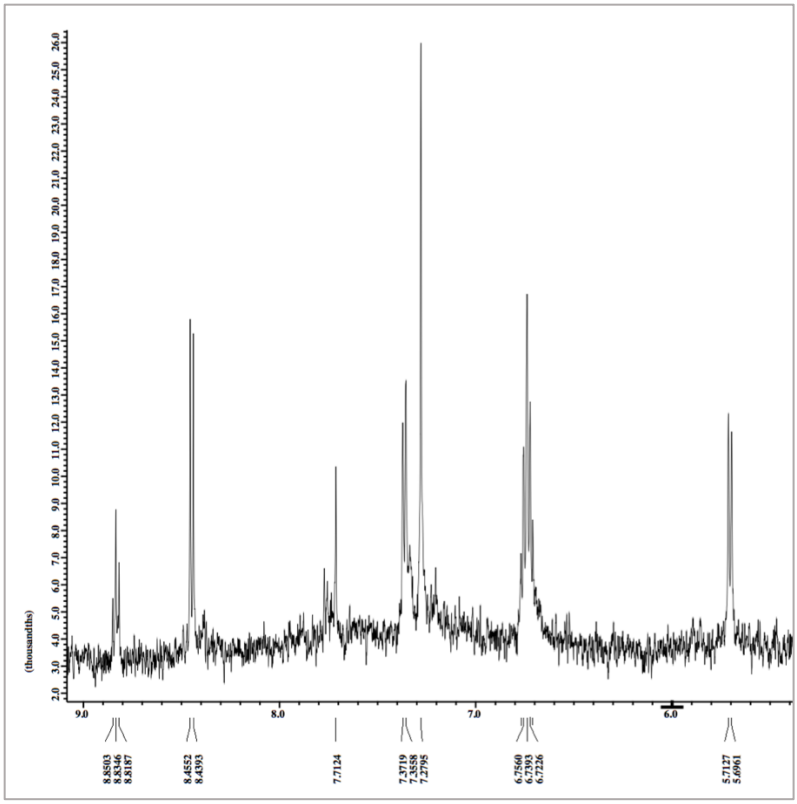

APPENDIX – K: ^{1}H NMR spectrum of $Si(IPI)_2$ (500 Mhz, $(CD_3)_2SO$)

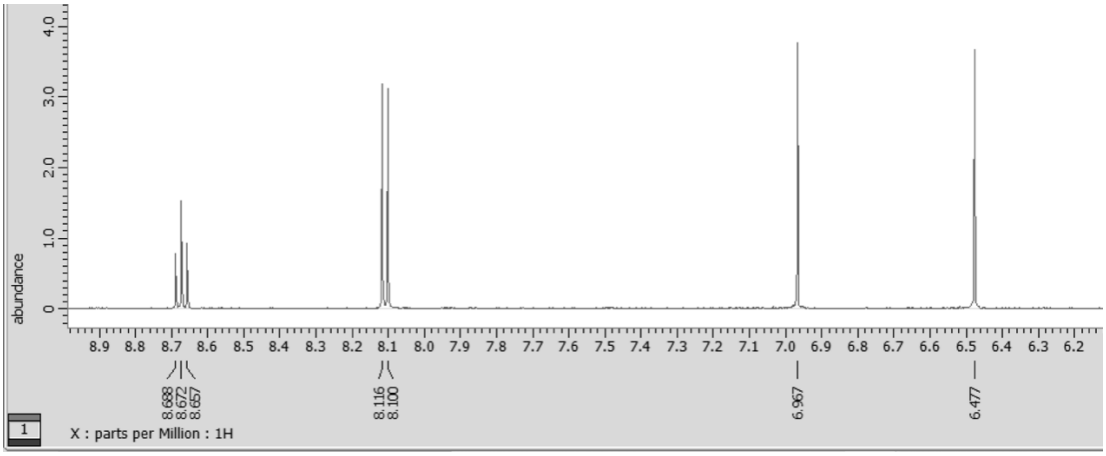

APPENDIX – L: ^{13}C NMR spectrum of $Si(bzimpyMe)_2$. (125 Mhz, CD_2Cl_2)

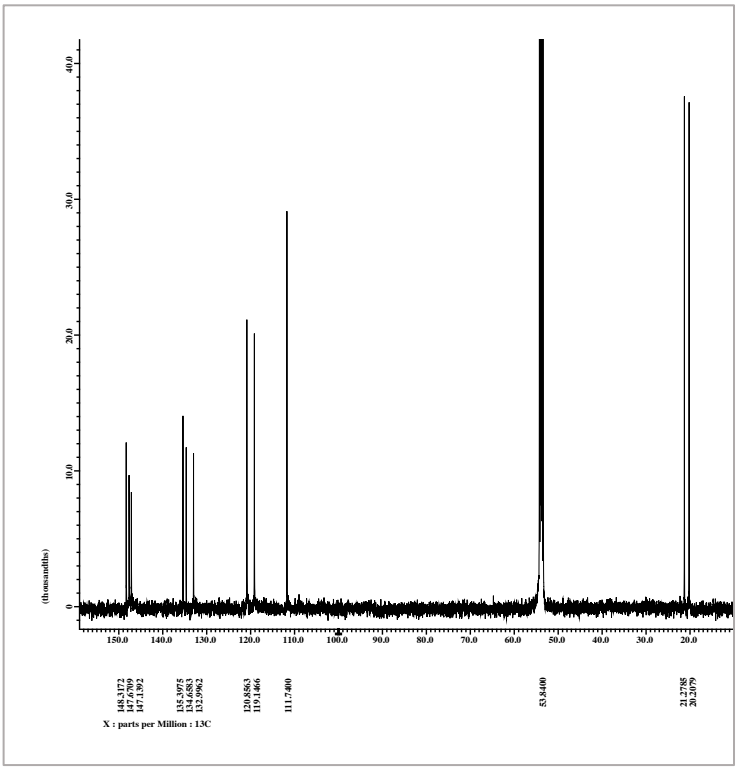

APPENDIX – M: ^{13}C NMR spectrum of $Si(bzimpyOMe)_2$. (125 Mhz, CD_2Cl_2)

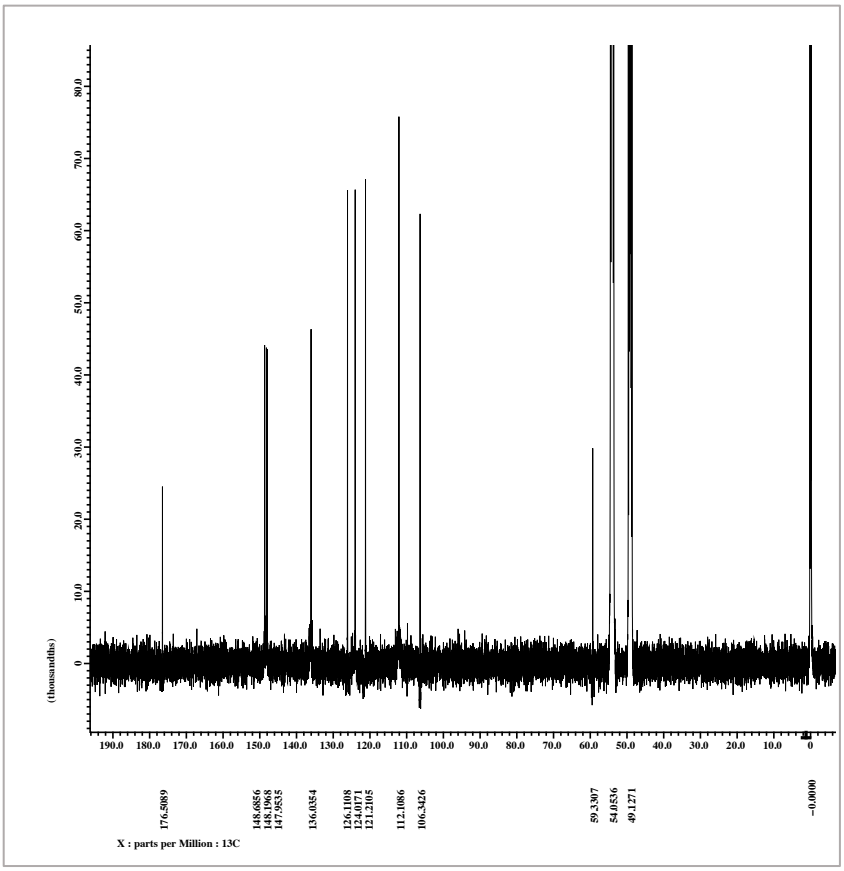

APPENDIX – N: ^{13}C NMR spectrum of $Si(bzimpyMeOMe)_2$. (125 Mhz, $(CD_3)_2SO$)

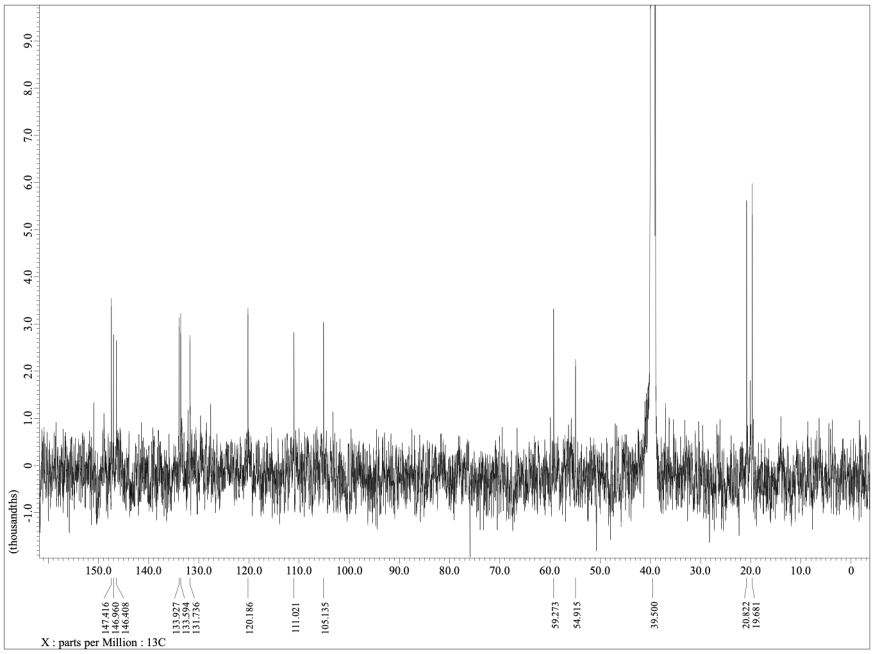

APPENDIX – O: ^{13}C NMR spectrum of $Si(BIP)_2$. (125 Mhz, $(CD_3)_2SO$)

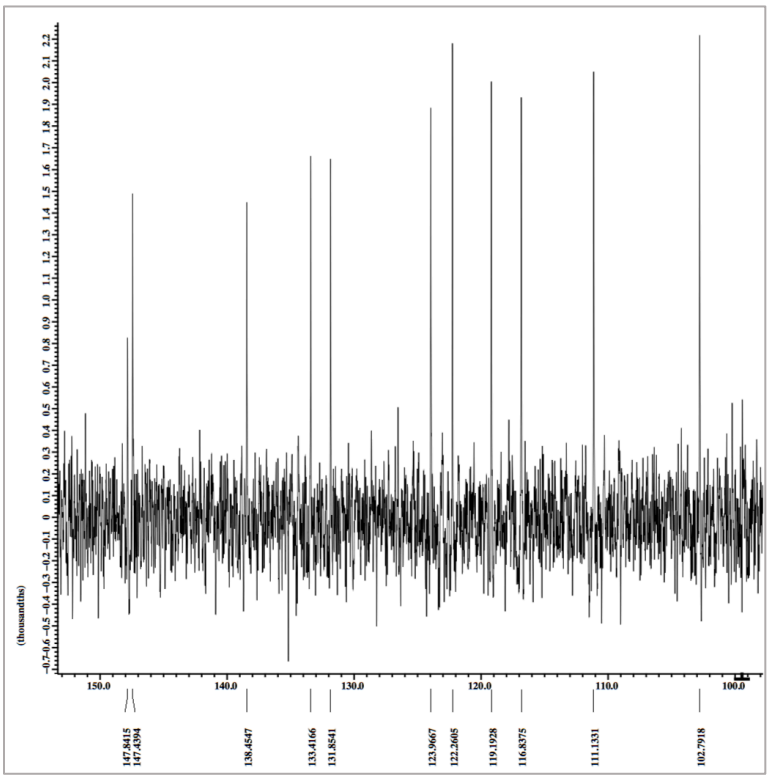

APPENDIX –P: ^{13}C NMR spectrum of $Si(IPI)_2$. (125 Mhz, $(CD_3)_2SO$)

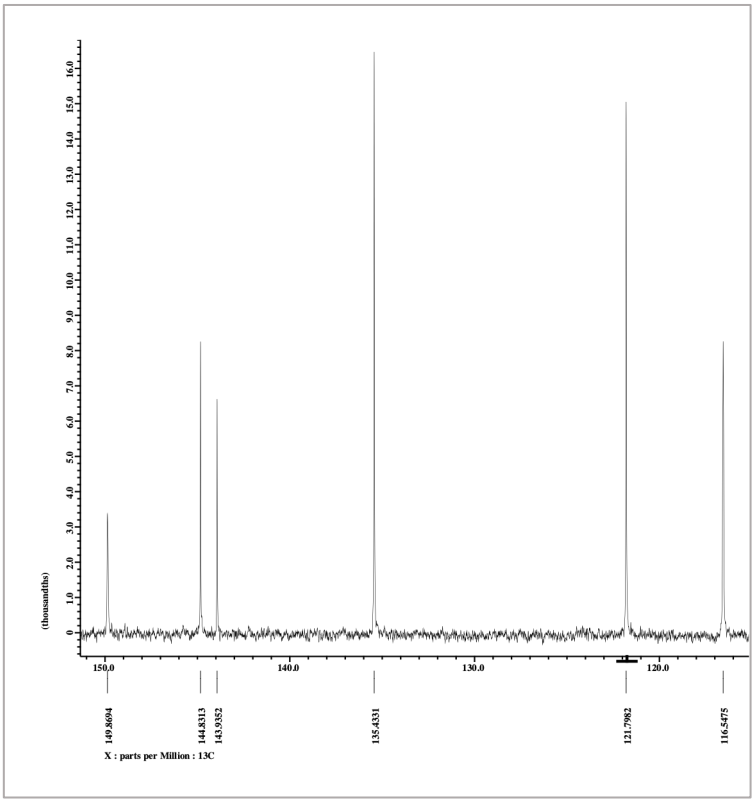

APPENDIX –Q: ^{29}Si NMR spectrum of Si(bzimpyMe)$_2$. (99 Mhz, CD_2Cl_2)

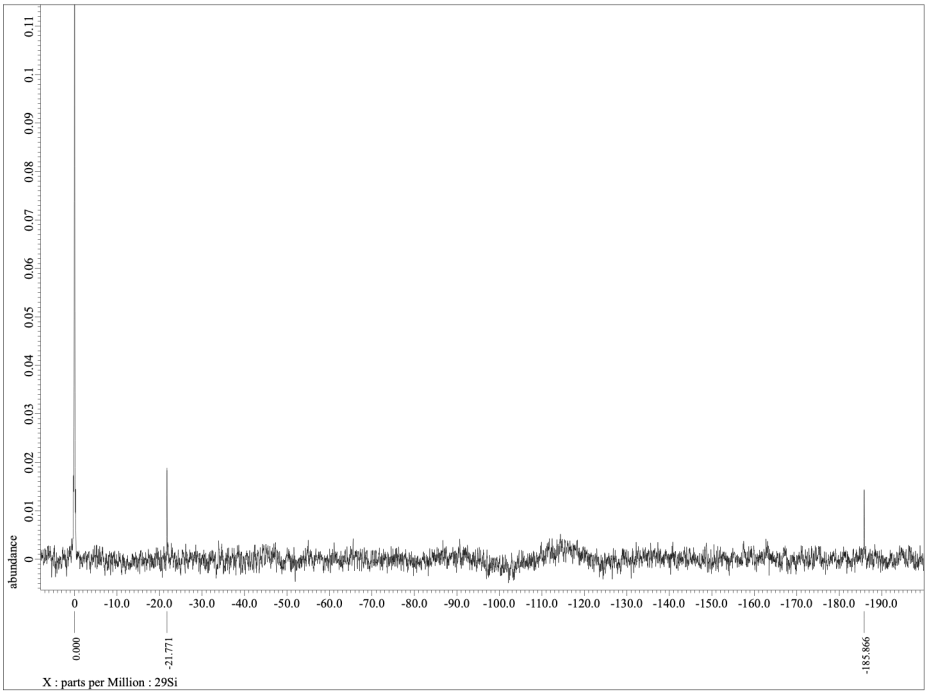

APPENDIX –R: ^{29}Si NMR spectrum of Si(bzimpyOMe)$_2$. (99 Mhz, CD_2Cl_2)

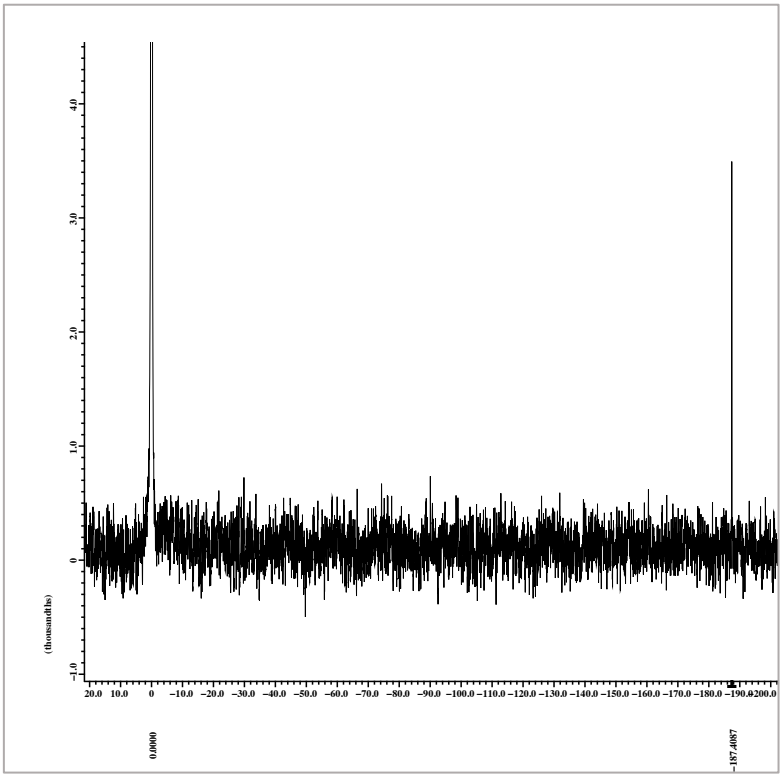

APPENDIX –S: ^{29}Si NMR spectrum of Si(bzimpyMeOMe)$_2$. (99 Mhz, $(CD_3)_2SO$)

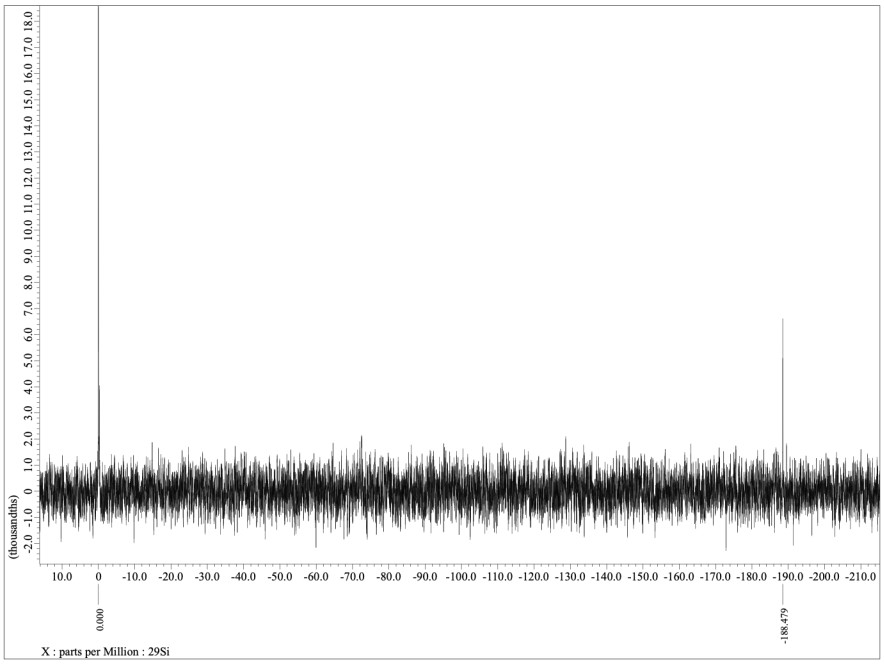

APPENDIX –T: ^{29}Si NMR spectrum of Si(BIP)$_2$. (99 Mhz, $(CD_3)_2SO$ and DMF)

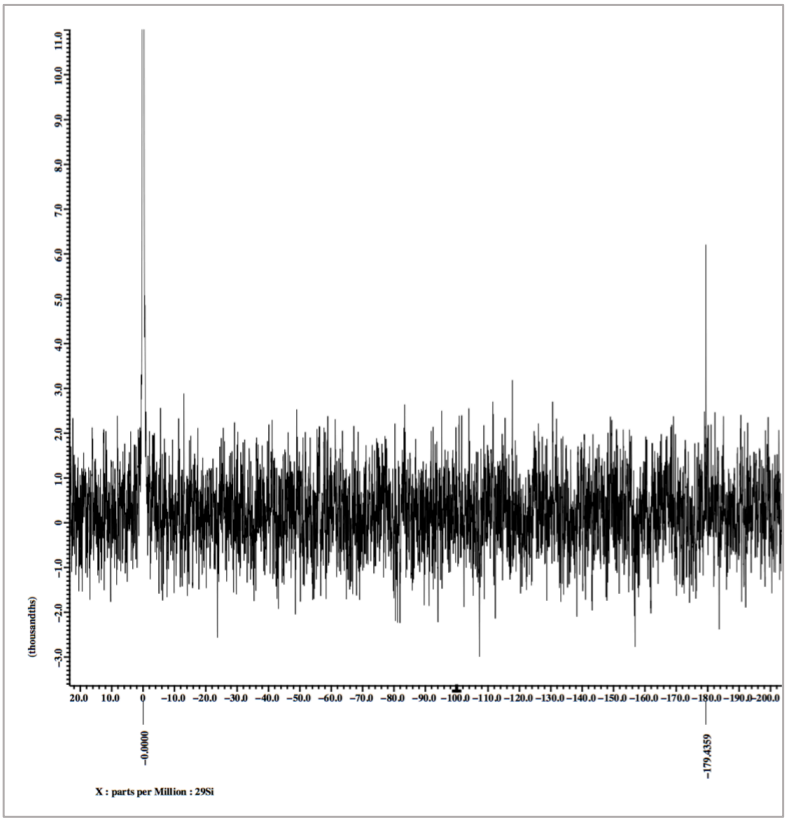

APPENDIX –U: ^{29}Si NMR spectrum of $Si(IPI)_2$. (99 Mhz, $(CD_3)_2SO$)

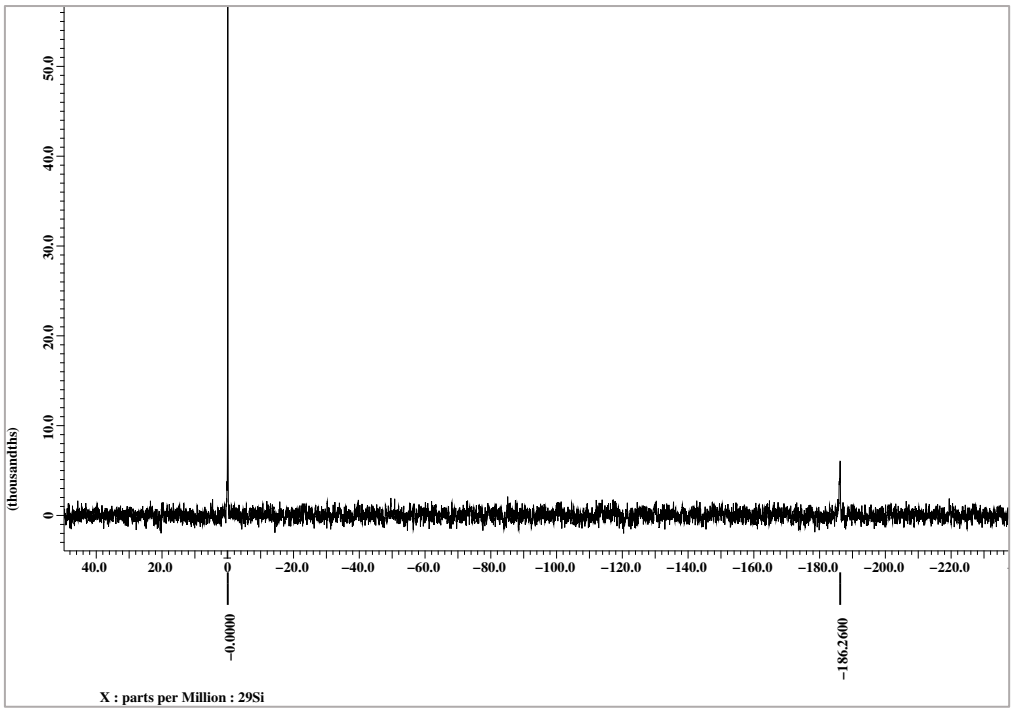

APPENDIX –V: MALDI-TOF-MS spectrum of $Si(bzimpyMe)_2$ (Matrix = 1,8,9-trihydroxyanthracene)

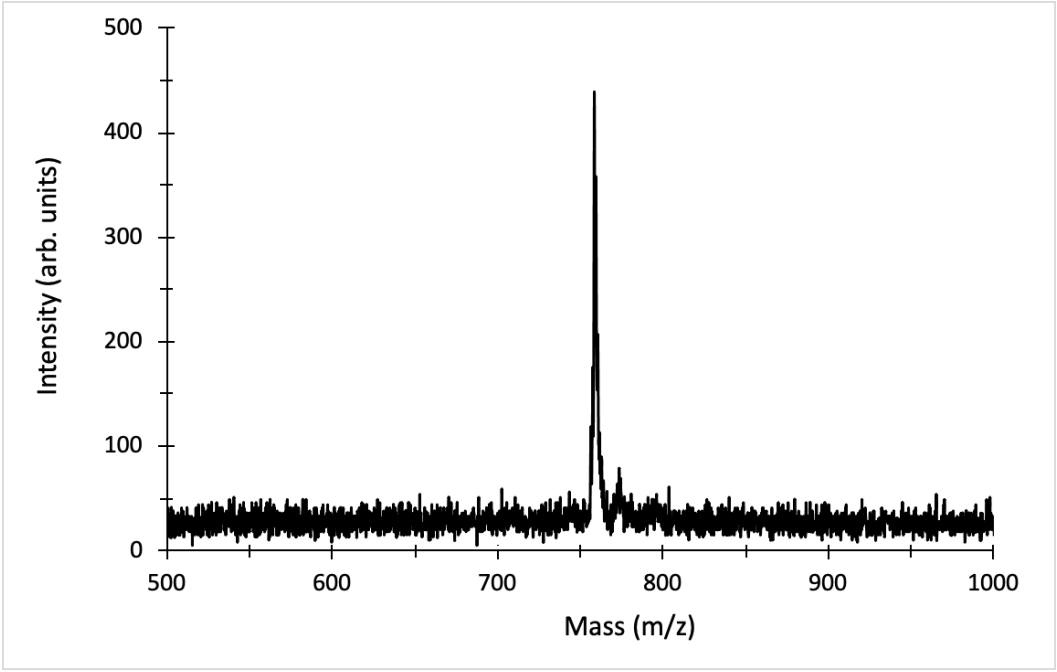

APPENDIX –W: MALDI-TOF-MS spectrum of $Si(bzimpyOMe)_2$ (Matrix = 1,8,9-trihydroxyanthracene)

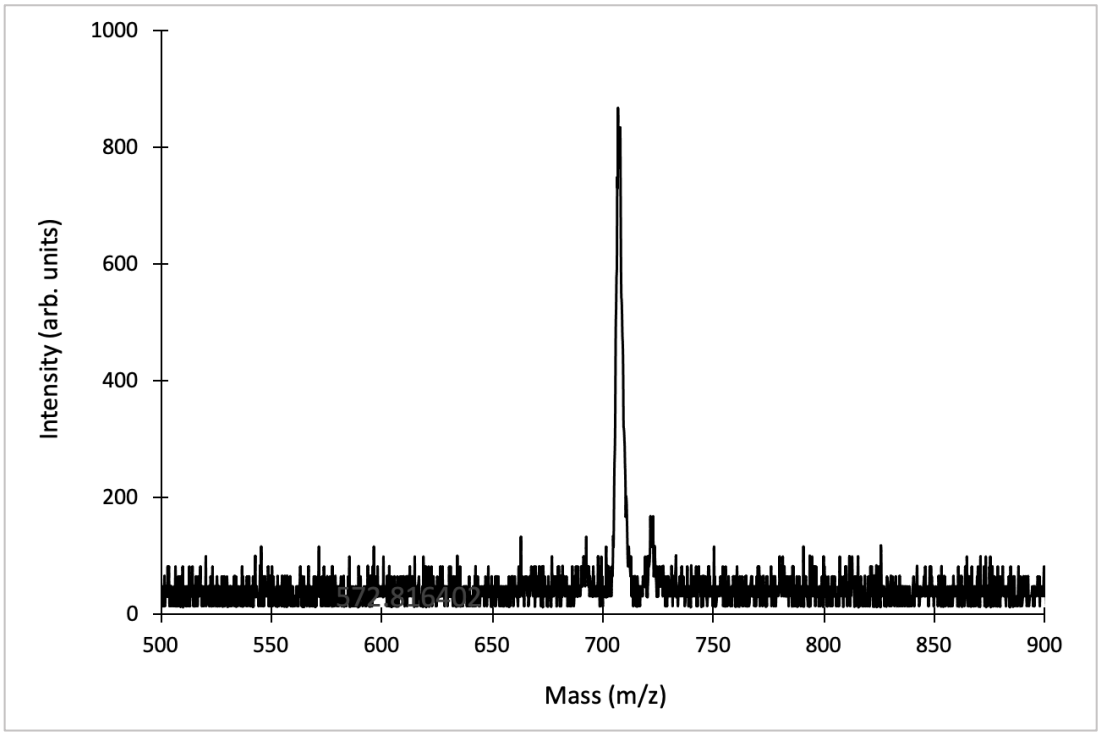

APPENDIX –X: MALDI-TOF-MS spectrum of $Si(bzimpyMeOMe)_2$ (Matrix = 1,8,9-trihydroxyanthracene)

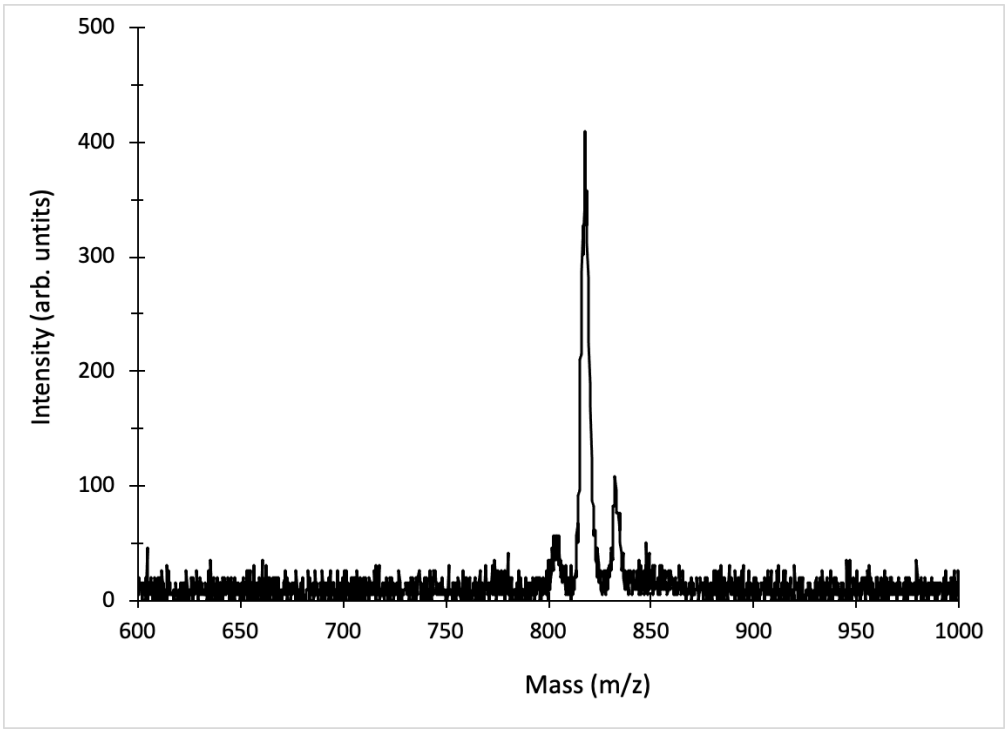

APPENDIX – Y: MALDI-TOF-MS spectrum of $Si(BIP)_2$ (Matrix = 1,8,9-trihydroxyanthracene)

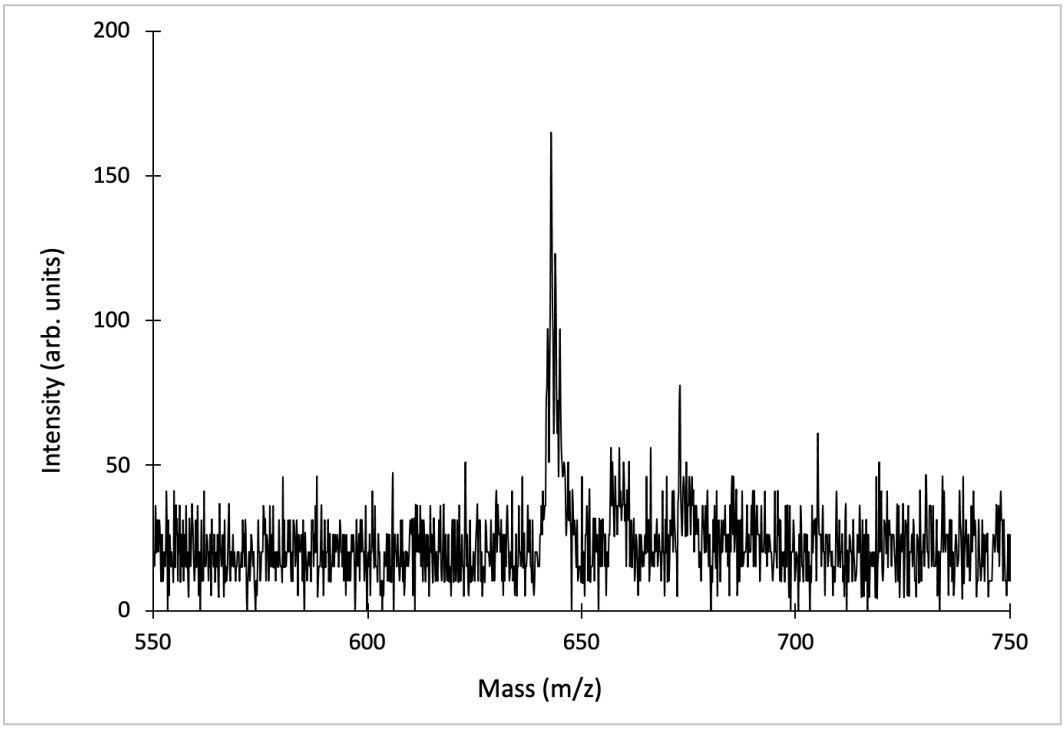

APPENDIX – Z: MALDI-TOF-MS spectrum of $Si(IPI)_2$ (Matrix = 1,8,9-trihydroxyanthracene)

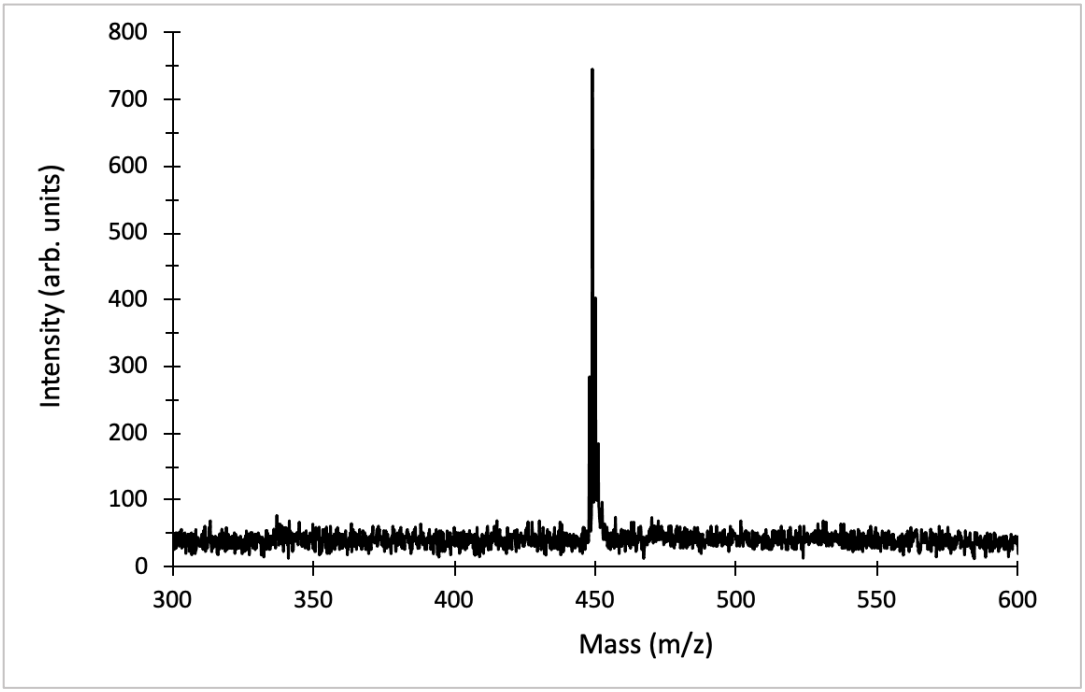

APPENDIX – AA: Cyclic voltammetry of $Si(BIP)_2$ in DMF TBAPF6

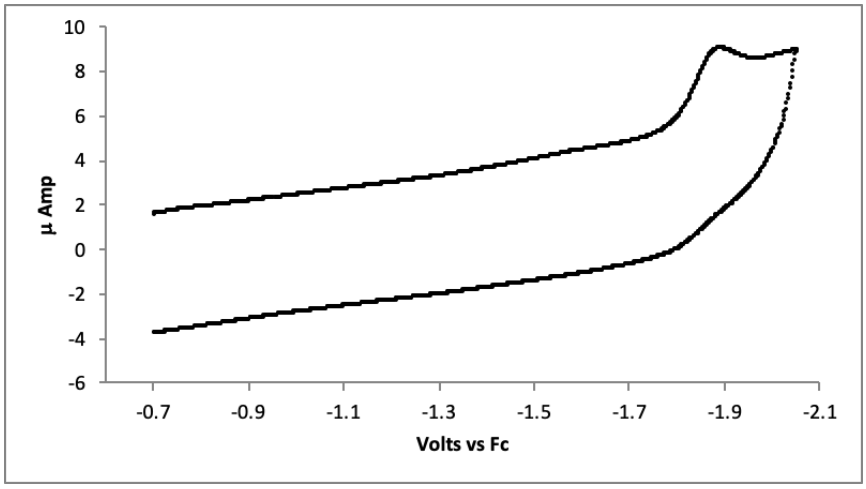

APPENDIX – AB: Cyclic voltammetry of $Si(bzimpy)_2$ in dichloromethane TBAPF6

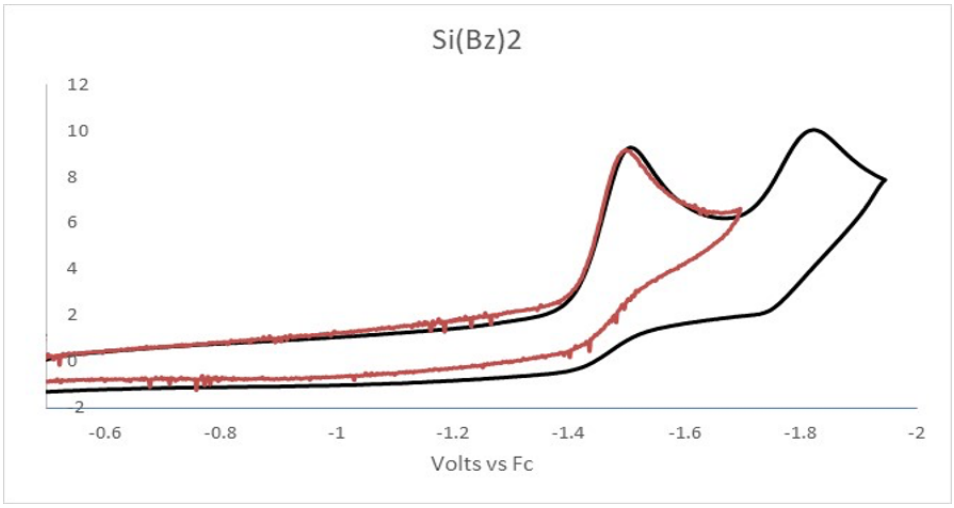

APPENDIX – AC: Cyclic voltammetry of $Si(bzimpyMe)_2$ in dichloromethane TBAPF6

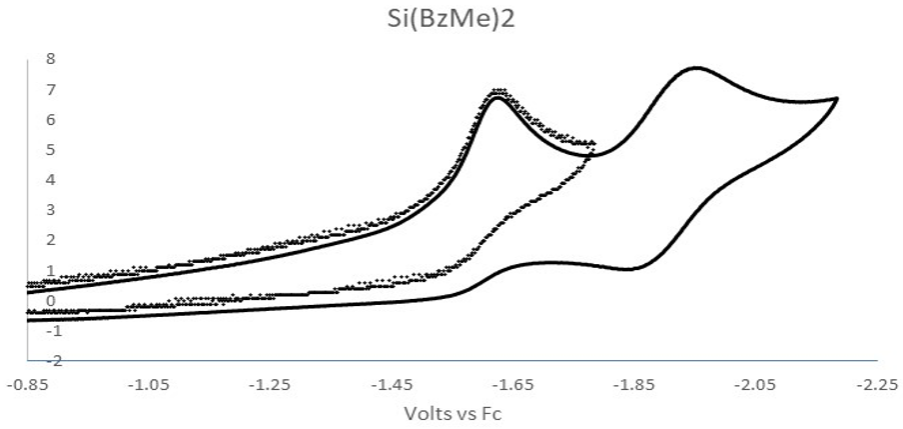

APPENDIX – AD: Cyclic voltammetry of $Si(bzimpyMe)_2$ in dichloromethane TBAPF6

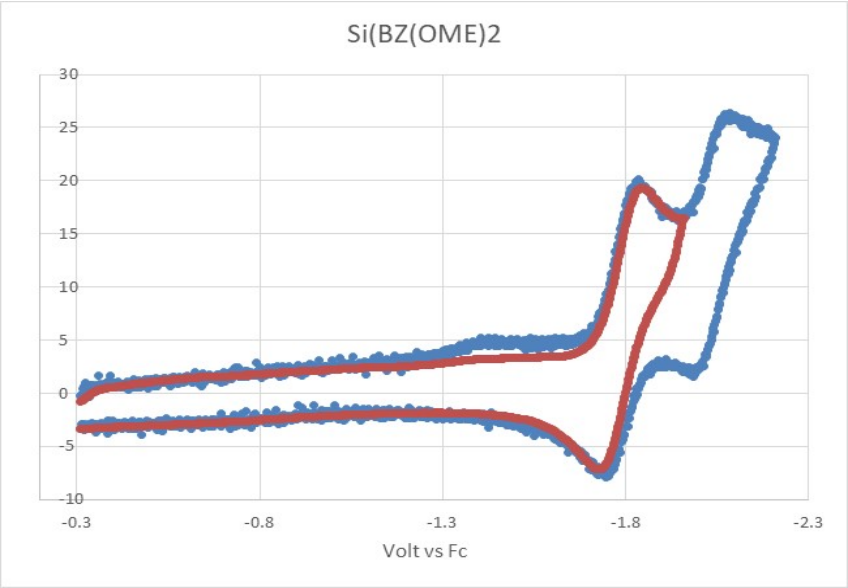

APPENDIX – AE: Cyclic voltammetry of $Si(bzimpyMeOMe)_2$ in dichloromethane TBAPF6

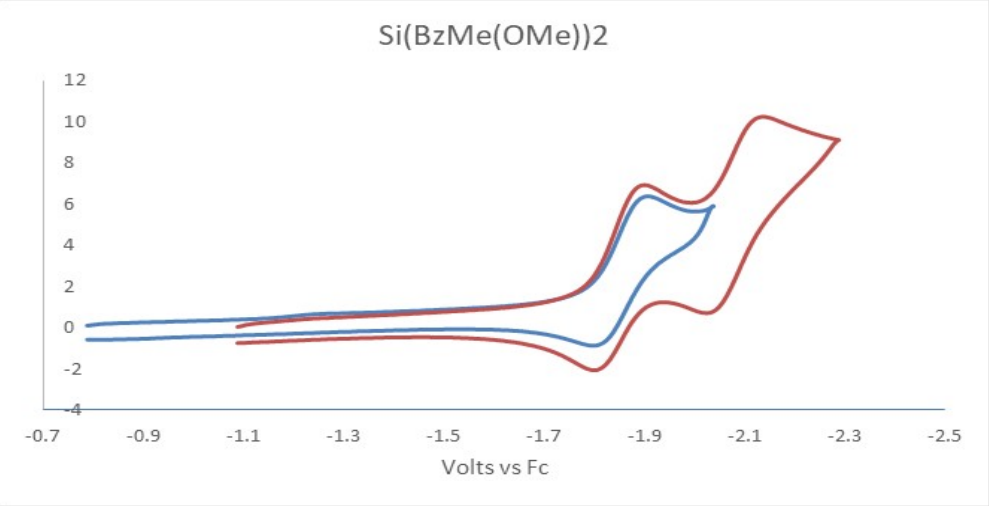

APPENDIX – AF: $Si(bzimpy)_2$ single crystal data tables

Table Crystal data and structure refinement for $Si(bzimpy)_2$.

Empirical formula	$C_{38}H_{22}N_{10}Si$
Formula weight	646.75
Temperature/K	298(3)
Crystal system	tetragonal
Space group	P-4n2
a/Å	9.8218(9)
b/Å	9.8218(9)
c/Å	15.820(4)
α/°	90
β/°	90
γ/°	90
Volume/$Å^3$	1526.1(4)
Z	2
$\rho_{calc}g/cm^3$	1.4299
μ/mm^{-1}	0.128
F(000)	678.7
Radiation	Mo Kα (λ = 0.71073)
2Θ range for data collection/°	7.8 to 57.18
Index ranges	$-13 \leq h \leq 8$, $-12 \leq k \leq 9$, $-19 \leq l \leq 20$
Reflections collected	3804
Independent reflections	1609 [R_{int} = 0.1028, R_{sigma} = 0.1850]
Data/restraints/parameters	1609/0/118
Goodness-of-fit on F^2	1.004
Final R indexes [I>=2σ (I)]	R_1 = 0.0729, wR_2 = 0.1223
Final R indexes [all data]	R_1 = 0.1838, wR_2 = 0.1737
Largest diff. peak/hole / e $Å^{-3}$	0.97/-0.52
Flack parameter	0.2(7)

APPENDIX – AG: $Si(bzimpyMe)_2$ single crystal data tables

Table Crystal data and structure refinement for $Si(bzimpyMe)_2$.

Empirical formula	$C_{46}H_{38}N_{10}Si$
Formula weight	758.97
Temperature/K	90(4)
Crystal system	orthorhombic
Space group	$Pca2_1$
a/Å	22.1141(15)
b/Å	10.9744(4)
c/Å	19.8058(8)
α/°	90
β/°	90
γ/°	90
Volume/$Å^3$	4806.6(4)
Z	4
$\rho_{calc}g/cm^3$	1.2479
μ/mm^{-1}	0.111
F(000)	1913.2
Radiation	Mo Kα (λ = 0.71073)
2Θ range for data collection/°	6.66 to 57.42
Index ranges	$-19 \leq h \leq 27$, $-14 \leq k \leq 14$, $-26 \leq l \leq 18$
Reflections collected	15306
Independent reflections	7865 [R_{int} = 0.0342, R_{sigma} = 0.0483]
Data/restraints/parameters	7865/1/621
Goodness-of-fit on F^2	1.057
Final R indexes [I>=2σ (I)]	R_1 = 0.0485, wR_2 = 0.1202
Final R indexes [all data]	R_1 = 0.0625, wR_2 = 0.1311
Largest diff. peak/hole / e $Å^{-3}$	0.37/-0.26
Flack parameter	-0.12(12)

APPENDIX – AH: $Si(bzimpyOMe)_2$ single crystal data tables

Table Crystal data and structure refinement for $Si(bzimpyOMe)_2$.

Empirical formula	$C_{41}H_{28}N_{10}O_2Si$
Formula weight	720.83
Temperature/K	99.98(10)
Crystal system	monoclinic
Space group	$P2_1/c$
a/Å	9.5059(3)
b/Å	30.4222(7)
c/Å	11.8486(4)
α/°	90
β/°	103.699(3)
γ/°	90
Volume/Å^3	3329.03(17)
Z	4
ρ_{calc}g/cm^3	1.4101
μ/mm^{-1}	1.072
F(000)	1469.5
Radiation	Cu Kα (λ = 1.54184)
2Θ range for data collection/°	8.22 to 133.46
Index ranges	$-8 \leq h \leq 11$, $-36 \leq k \leq 35$, $-14 \leq l \leq 13$
Reflections collected	22280
Independent reflections	5884 [R_{int} = 0.0480, R_{sigma} = 0.0365]
Data/restraints/parameters	5884/0/582
Goodness-of-fit on F^2	1.079
Final R indexes [I>=2σ (I)]	R_1 = 0.0433, wR_2 = 0.0999
Final R indexes [all data]	R_1 = 0.0536, wR_2 = 0.1075
Largest diff. peak/hole / e Å^{-3}	0.32/-0.46

APPENDIX – AI: $Si(bzimpyMeOMe)_2$ single crystal data tables

Table Crystal data and structure refinement for $Si(bzimpyMeOMe)_2$.

Empirical formula	$C_{48}H_{42}N_{10}O_2Si$
Formula weight	819.02
Temperature/K	100.0(1)
Crystal system	monoclinic
Space group	$P2_1/c$
a/Å	10.78042(19)
b/Å	23.4583(4)
c/Å	20.0208(4)
α/°	90
β/°	95.6050(17)
γ/°	90
Volume/Å^3	5038.87(16)
Z	4
ρ_{calc}g/cm^3	1.2318
μ/mm^{-1}	0.901
F(000)	2011.2
Radiation	Cu Kα (λ = 1.54184)
2Θ range for data collection/°	7.54 to 133.5
Index ranges	$-12 \leq h \leq 12$, $-27 \leq k \leq 27$, $-21 \leq l \leq 23$
Reflections collected	37658
Independent reflections	8909 [R_{int} = 0.0438, R_{sigma} = 0.0350]
Data/restraints/parameters	8909/0/785
Goodness-of-fit on F^2	1.052
Final R indexes [I>=2σ (I)]	R_1 = 0.0458, wR_2 = 0.1150
Final R indexes [all data]	R_1 = 0.0614, wR_2 = 0.1279
Largest diff. peak/hole / e Å^{-3}	0.50/-0.33

APPENDIX – AJ: $Si(IPI)_2$ single crystal data tables

Table Crystal data and structure refinement for $Si(IPI)_2$.

Empirical formula	$C_{22}H_{14}N_{10}Si$
Formula weight	446.51
Temperature/K	100.0(1)
Crystal system	orthorhombic
Space group	$Pna2_1$
a/Å	16.6643(3)
b/Å	13.2204(2)
c/Å	19.9165(4)
α/°	90
β/°	90
γ/°	90
Volume/Å^3	4387.78(13)
Z	4
ρ_{calc}g/cm^3	1.4487
μ/mm^{-1}	1.291
F(000)	1992.0
Radiation	Cu Kα (λ = 1.54184)
2Θ range for data collection/°	8.02 to 133.58
Index ranges	$-19 \leq h \leq 17$, $-15 \leq k \leq 14$, $-22 \leq l \leq 23$
Reflections collected	18383
Independent reflections	6619 [R_{int} = 0.0334, R_{sigma} = 0.0316]
Data/restraints/parameters	6619/1/635
Goodness-of-fit on F^2	1.068
Final R indexes [I>=2σ (I)]	R_1 = 0.0359, wR_2 = 0.0873
Final R indexes [all data]	R_1 = 0.0406, wR_2 = 0.0914
Largest diff. peak/hole / e Å^{-3}	0.20/-0.32
Flack parameter	0.06(3)